P-12-06

Temperature buffer test

Hydro-mechanical and chemical/ mineralogical characterizations

Mattias Åkesson, Siv Olsson, Ann Dueck,
Ulf Nilsson, Ola Karnland
Clay Technology AB

Leena Kiviranta, Sirpa Kumpulainen
B+Tech Oy

Johan Lindén, Åbo Akademi

January 2012

Svensk Kärnbränslehantering AB
Swedish Nuclear Fuel
and Waste Management Co

Box 250, SE-101 24 Stockholm
Phone +46 8 459 84 00

ISSN 1651-4416
SKB P-12-06
ID 1327614

Temperature buffer test

Hydro-mechanical and chemical/ mineralogical characterizations

Mattias Åkesson, Siv Olsson, Ann Dueck,
Ulf Nilsson, Ola Karnland
Clay Technology AB

Leena Kiviranta, Sirpa Kumpulainen
B+Tech Oy

Johan Lindén, Åbo Akademi

January 2012

Keywords: Field test, Buffer, Bentonite, Temperature, Hydraulic conductivity, Swelling pressure, Water retention curve, Shear strength, Chemical composition, Smectite composition, Mineralogical composition.

This report concerns a study which was conducted for SKB. The conclusions and viewpoints presented in the report are those of the authors. SKB may draw modified conclusions, based on additional literature sources and/or expert opinions.

Data in SKB's database can be changed for different reasons. Minor changes in SKB's database will not necessarily result in a revised report. Data revisions may also be presented as supplements, available at www.skb.se.

A pdf version of this document can be downloaded from www.skb.se.

Abstract

The Temperature Buffer Test (TBT) is a joint project between SKB/ANDRA and supported by ENRESA (modeling) and DBE (instrumentation), which aims at improving the understanding and to model the thermo-hydro-mechanical behavior of buffers made of swelling clay submitted to high temperatures (over 100°C) during the water saturation process. The test has been carried out in a KBS-3 deposition hole at Äspö HRL. It was installed during the spring of 2003. Two steel heaters (3 m long, 0.6 m diameter) and two buffer arrangements have been investigated: the lower heater was surrounded by rings of compacted Wyoming bentonite only, whereas the upper heater was surrounded by a composite barrier, with a sand shield between the heater and the bentonite. The test was dismantled and sampled during the winter of 2009/2010.

This report presents the hydro-mechanical and chemical/mineralogical characterization program which was launched subsequent to the dismantling operation. The main goal has been to investigate if any significant differences could be observed between material from the field experiment and the reference material. The field samples were mainly taken from Ring 4 (located at the mid-section around the lower heater), in which the temperature in the innermost part reached 155°C.

The following hydro-mechanical properties have been determined for the material (test technique within brackets): hydraulic conductivity (swelling pressure device), swelling pressure (swelling pressure device), unconfined compression strength (mechanical press), shear strength (triaxial cell) and retention properties (jar method). The following chemical/mineralogical properties (methods within brackets) were determined: anion analysis of water leachates (IC), chemical composition (ICP/AES+MS, EGA), cation exchange capacity (CEC, Cu-trien method) and exchangeable cations (exchange with NH_4, ICP-AES), mineralogical composition (XRD and FTIR), element distribution and microstructure (SEM and TEM), iron oxidation state (Mössbauer spectroscopy). The retention tests, the CEC-determinations, the chemical analyses by ICP, and the mineralogical analyses by XRD and FTIR were performed on bulk samples as well as on a Na-converted fine fraction (<0.5 μm). The latter fraction was subjected also to TEM analyses.

The hydro-mechanical characterizations of the bentonite resulted in the following observations: i) compared to the reference material no large deviation was seen in the retention curves for the Na converted fine fraction of the material from the innermost positions, and for the bulk material from the same positions a marked deviation was observed for equilibrium with RH = 97%; ii) a reduction in swelling pressure was observed on re-saturated samples from the field experiment, especially on those from the innermost part. Measured hydraulic conductivity values were generally scattered, but displayed a tendency with increased values on re-saturated specimens drilled from the innermost part, and a similar tendency was also observed on ground and re-compacted specimens and specimens prepared from dried material; iii) the triaxial test performed on the one specimen from the inner part demonstrated a brittle behaviour involving high stiffness, high shear strength, and low strain at failure; and iv) the unconfined compression tests demonstrated a reduced strain at failure on all specimens from the field material, and also a reduced maximum deviator stress on the re-saturated specimens from the innermost position.

The chemical/mineralogical characterization indicated that: i) sulfate was redistributed under the thermal and hydration gradients that were prevalent during the test. Anhydrite accumulated at some distance from the heater, whereas gypsum was dissolved in the peripheral parts of the buffer where water was supplied; ii) cristobalite was dissolved at the bentonite/heater contact; iii) calcite was dissolved in the warmest parts of the block; iv) exchangeable sodium was replaced by calcium in the warmest parts, probably as an effect of calcite dissolution, which must have affected the porewater composition; v) at the heater, the iron content of the bentonite had increased due to corrosion of the steel. The excess iron was readily extractable into a citrate-bicarbonate-dithionite solution, which suggests that iron was not incorporated into the smectite structure but existed mainly as free oxides/oxyhydroxides (after oxidation); vi) the distribution of non-exchangeable magnesium displayed a clear gradient with a distinct maximum at the heater, suggesting a transfer of magnesium along the thermal gradient; vii) the Mössbauer spectroscopy with a three component fit and the measurements with lower Doppler-velocity indicated that the amount of Fe^{2+} had increased slightly, but the five component fit didn't support this observation. Hence, the increase in the amount of iron observed with chemical analyses was probably too small to be detected reliably with Mössbauer spectroscopy.

Contents

1 Introduction

1.1 TBT experiment

The Temperature Buffer Test (TBT) is a joint project between SKB/ANDRA and supported by ENRESA (modelling) and DBE (instrumentation). The test aims at improving the understanding of the thermo-hydro-mechanical (THM) behaviour of clay buffers at temperatures around and above 100°C during the water saturation transient, in order to be able to model this behaviour.

The experiment was installed during the spring of 2003 (see Johannesson et al. 2010) and was dismantled during the winter of 2009/2010, i.e. after an operational time of approximately 2,500 days. The test has been carried out at the –420 m level in Äspö HRL in a 8 meters deep and 1.76 m diameter deposition hole, with two carbon steel heaters (3 m long, 0.6 m diameter), surrounded by four cylinders and 12 rings of compacted MX-80, a sodium dominated Wyoming bentonite produced by American Colloid Company. On the top, there was a confining concrete plug and a steel lid anchored with 9 rods (Figure 1-1). Two buffer arrangements have been investigated. The lower heater was surrounded by bentonite only, whereas the upper heater was surrounded by a composite barrier, with a sand shield between the heater and the bentonite. The latter has acted as a thermal protection for the bentonite, and as an important component for the retrievability.

The bentonite around the lower heater has been exposed to high temperatures. During the first ~1,700 days, the power output from each heater was 1,500 W (1,600 W during a limited period, see Figure 1-2). These conditions implied that the highest temperature at the heater surface was approximately 135–145°C (see Figure 1-3, left). During the last ~600 days, the power output from the lower heater was 2,000 W, whereas the corresponding value for the upper heater was 1,000 W. These conditions implied that the highest temperature at the heater surface was approximately 154–159°C (see Figure 1-3, right).

The experiment has been artificially supplied with water through a sand-filled filter between the bentonite and the rock. Injection pressures, filter pressures and injected volumes are shown in Figure 1-2. From the start of the test, a groundwater from a nearby borehole (HD0025A, see Table 1-1) was used for the hydration of the bentonite. The groundwater was replaced with de-ionized water from day 1,483, due to the high flow resistance of the injections points in the filter, which implied that a high filter pressure couldn't be sustained. The high flow resistance was caused by precipitates of calcite on the filter tips, see Goudarzi et al. (2010).

The dismantling operation was performed during a period from the end of October 2009 to the end of April 2010 (see Åkesson 2010). One important goal with the dismantling operation was to obtain different types of samples. Bentonite cores were devoted for the determination of water content and density. Large pieces of bentonite, so-called big sectors, were devoted for the hydro-mechanical and chemical/mineralogical program. The main method to sample and partition the bentonite blocks was with the use of handheld coring machines (Ø50 mm). For each block a coring scheme was specified according to which cores were to be taken in four directions (32, 122, 212 and 302°) at 50 mm intervals. The two big sectors were "cut" through stitch drilling from each block representing the entire radial distribution in two directions, 32 and 212°. In the lower part of the experiment, it was found to be beneficial to make a circular stitch drill around the heater, which enabled the sampling of suitable pieces close to the heater. All samples were packaged in evacuated aluminium laminate foil bags.

The determinations of density and water content have provided information about the final state of the bentonite (see Johannesson et al. 2010). Distributions of water content and dry density are shown in Figure 1-4 and Figure 1-5. The high temperature conditions around the lower heater apparently coincided with conditions with relatively low water contents and high dry density values.

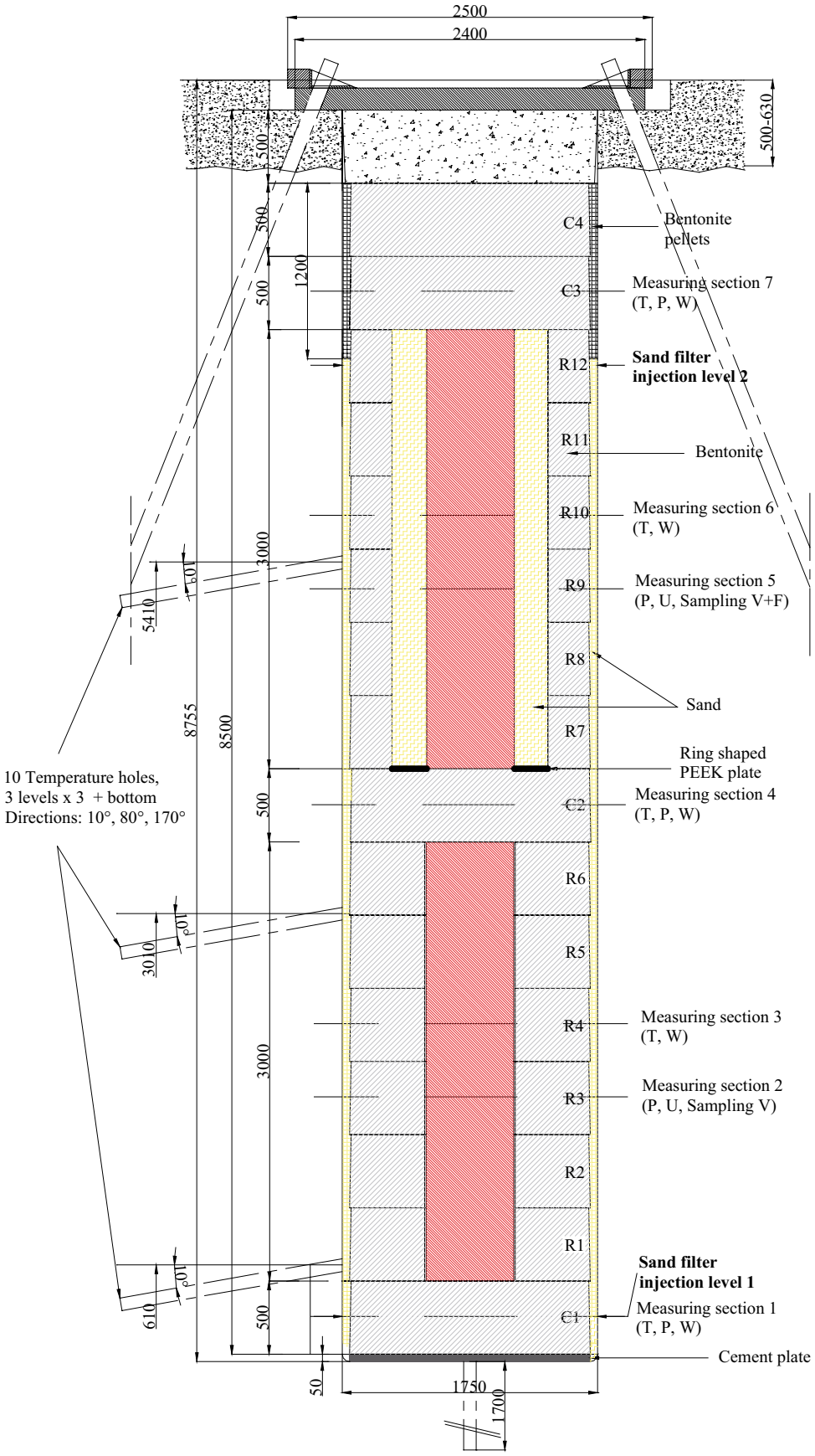

Figure 1-1. *Design of the TBT experiment.*

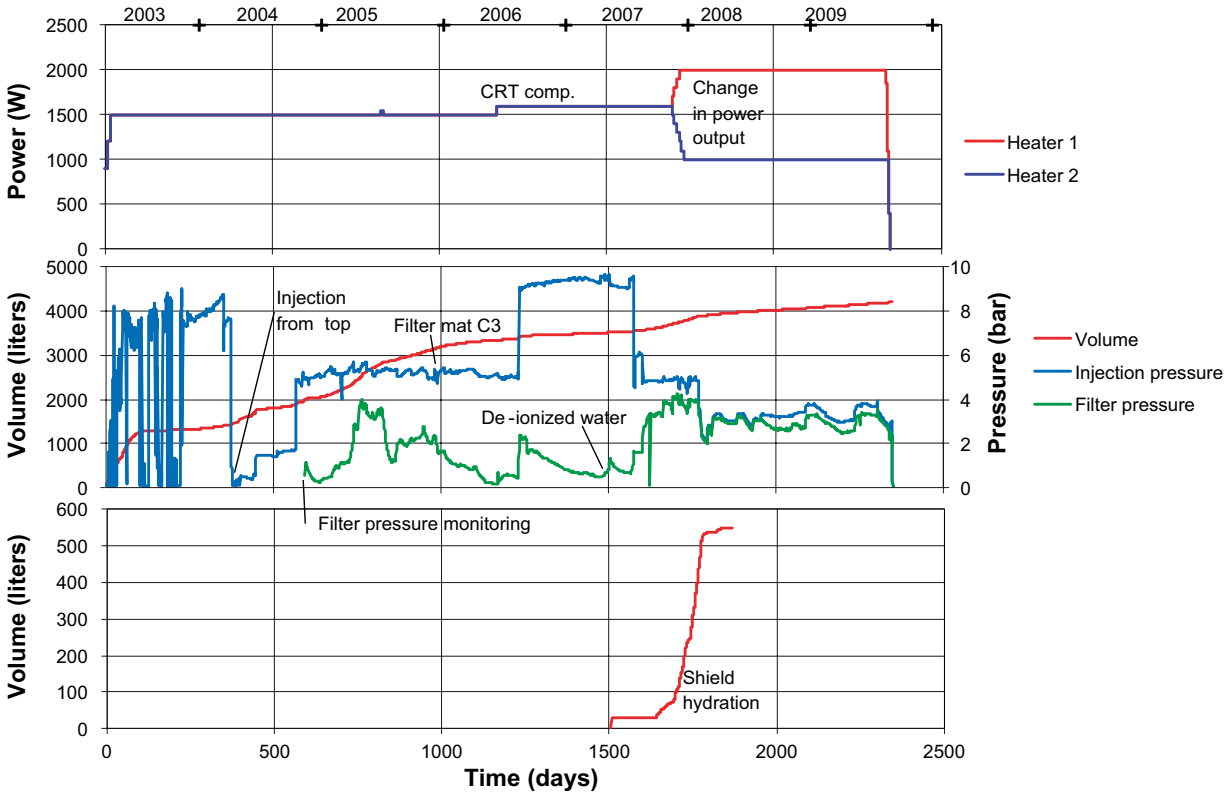

Figure 1-2. Timeline of major events regarding power output (upper), filter injection system with total injected volume and pressures (middle); and shield hydration (lower) with total injected volume.

Table 1-1. Main composition of the groundwater in water supply bore hole HD0025A in 2002, 2004 and 2006.

HD0025A Units	Na mM	K mM	Ca mM	Mg mM	HCO3 mM	Cl mM	SO4 mM	Br mM	F mM	Si mM	pH	E.C. mS/m
2002-09-24	69.2	0.711	15.7	4.94	2.69	108	3.29	0.274	0.0863	0.192	7.45	1,180
2004-09-21	64.4	0.749	15.2	4.36	2.79	94.8	3.38	0.373	0.0763	0.200	7.45	1,020
2006-10-04	76.1	0.731	22.2	4.69	2.64	120	3.71	0.260	0.0768	0.223	7.45	1,140

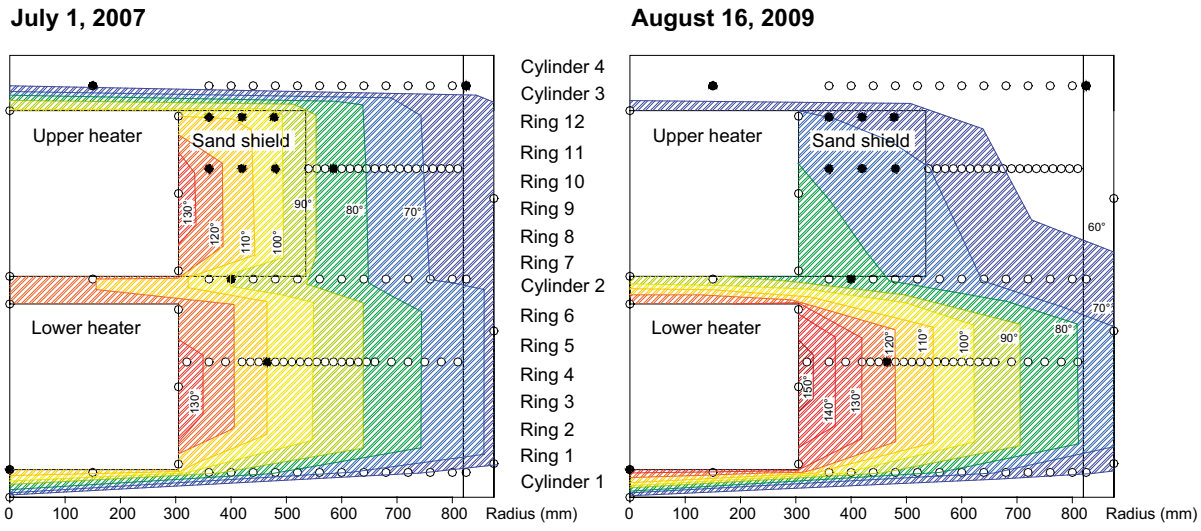

Figure 1-3. Temperature distribution on July 1, 2007 (left) and August 16, 2009 (right). Rings indicate sensor positions. Filled rings indicate sensors out of order (from Goudarzi et al. 2010).

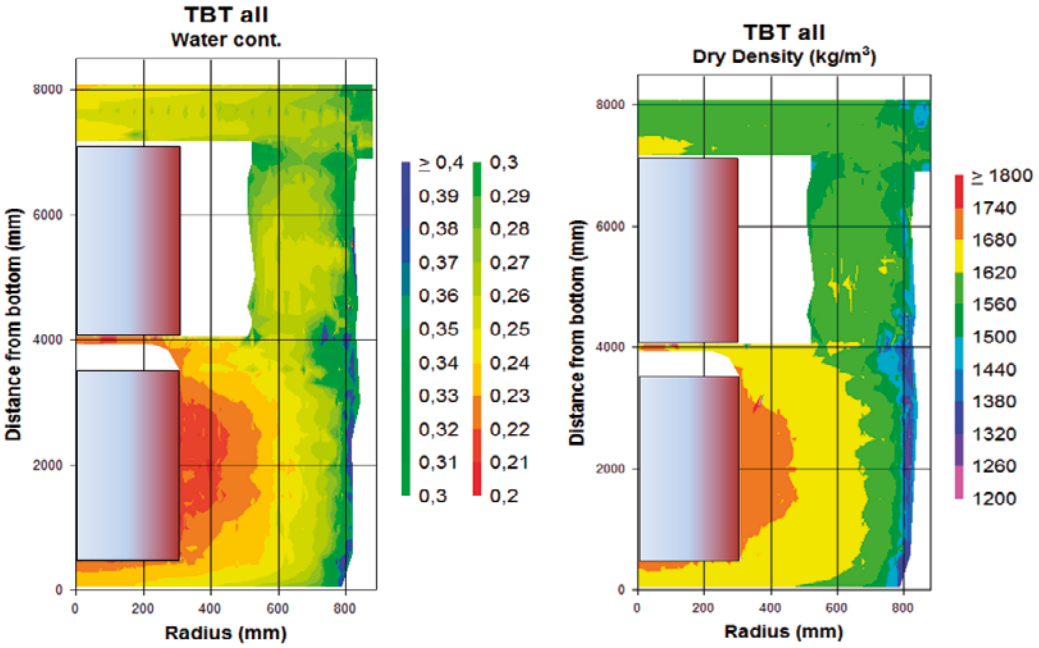

Figure 1-4. *Results from measurements of density and water content. Distributions of water content (left) and dry density (right) at the end of the test (from Johannesson 2010).*

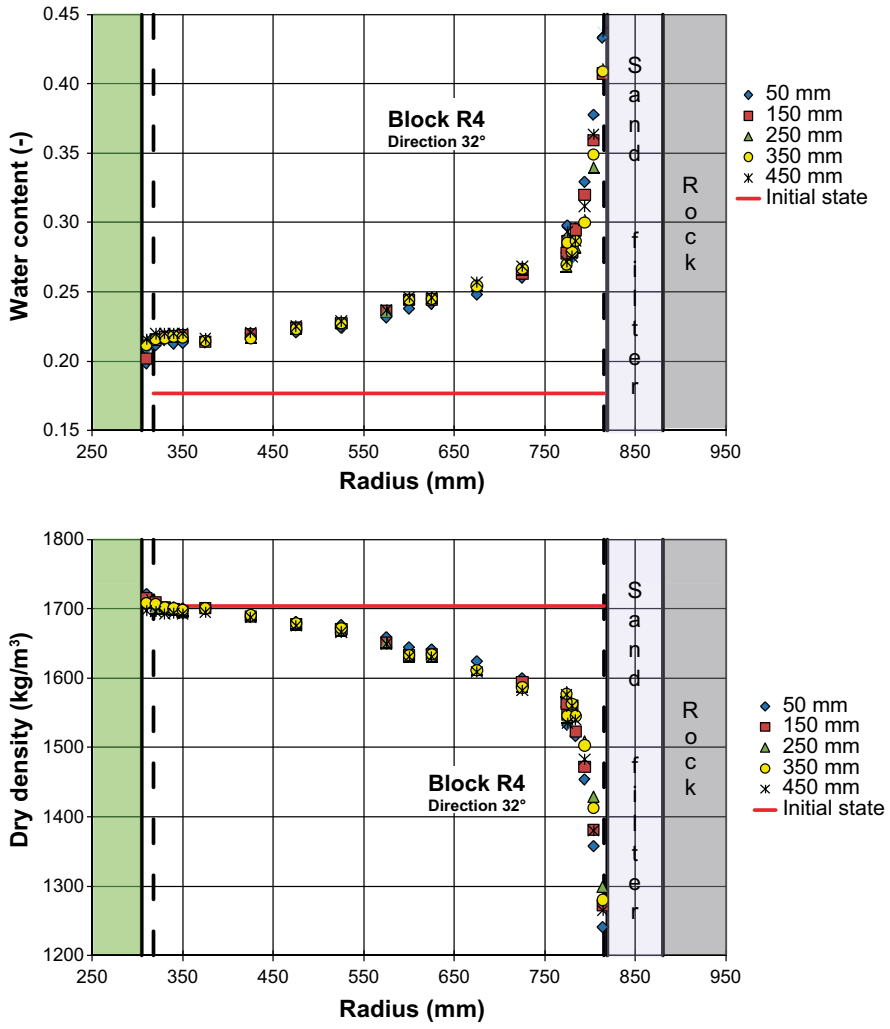

Figure 1-5. *Distributions of water content (upper) and dry density (lower) at the end of the test in Ring 4 in the 32° direction (from Johannesson 2010).*

1.2 Test philosophy

The main goal of the hydro-mechanical and chemical/mineralogical characterization program has been to investigate if any significant differences could be observed between exposed samples taken from the TBT field conditions with high temperature and high thermal gradient on one hand, and reference material on the other.

The following hydro-mechanical properties have been determined for the material (test technique within brackets):

- hydraulic conductivity (swelling pressure device),
- swelling pressure (swelling pressure device),
- unconfined compression strength (mechanical press),
- shear strength (triaxial cell),
- retention properties (jar method),

and the following chemical/mineralogical properties (methods within brackets):

- anion analysis in water solution (IC),
- element content (ICP/AES+MS,EGA),
- cation exchange capacity (CEC,Cu-trien method),
- exchangeable cations (exchange with NH_4, ICP-AES),
- mineralogical composition (XRD and FTIR),
- element distribution and microstructure (SEM and STEM),
- iron oxidation state (Mössbauer spectroscopy).

The plan for the analyses was to first perform a *Primary scan* on exposed samples taken at 10 cm intervals from the mid-section of the lower heater (Figure 1-6). The characterization program focused on this section since it exhibited the most adverse thermal conditions in the experiment. Several analyses (*base analyses*, Table 1-2) have been performed on all these exposed samples, whereas other resource-demanding analyses *(additional analyses*, Table 1-2) have been limited to samples taken from the inner parts of this section. All analyses have also been performed on reference material, and in the case of the base analyses at least three analyses have been performed.

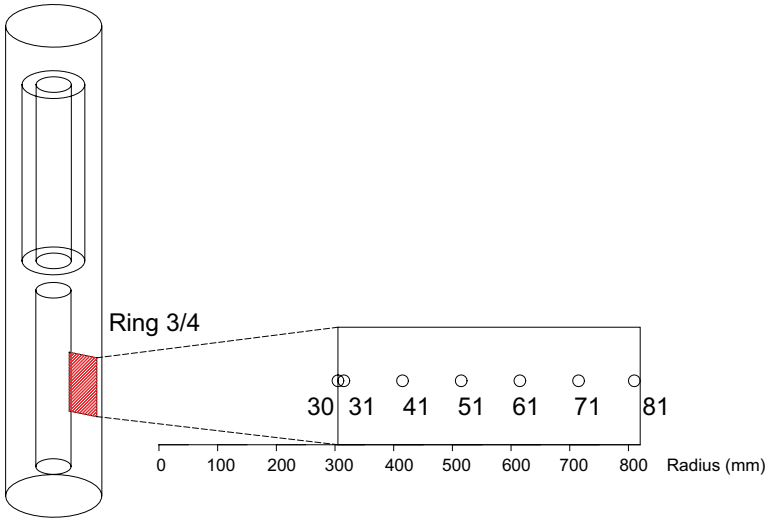

Figure 1-6. *Specified radial sample positions for the main part of the analyzed samples.*

Table 1-2. Compilation of base and additional analyses (preparation/fraction; Na-fines = sodium converted clay fraction <0.5 µm size).

Base analyses	Additional analyses
Swelling pressure and hydraulic cond. (trimmed, re-compacted)	Retention properties (bulk, Na-fines)
Unconfined compression tests (trimmed)	Triax (trimmed)
IC (water extract)	XRD (Na-fines)
ICP/AES+MS+EGA (bulk, Na-fines)	FTIR (Na-fines)
EC (bulk)	SEM/STEM (bulk, Na-fines)
CEC (bulk, Na-fines)	Mössbauer spectroscopy (bulk)
XRD (bulk)	
FTIR (bulk)	

A *Secondary scan* was subsequently defined based on the outcome of the primary scan. The motive for these additional analyses mainly concerned the *possibility to make indications of changes statistically significant* and included additional measurements of swelling pressure and hydraulic conductivity and unconfined compression tests; re-runs of XRD (bulk) and Mössbauer analyses; and the refined pre-treatment methods of CBD extractions (for subsequent Fe-analyses) and Greene-Kelly (for subsequent CEC-analyses).

A compilation of the number of analyses in the two scans, performed on exposed sample as well as reference material, is given in Table 1-3.

Table 1-3. Numbers of analyses in the primary and the secondary scans. Asterisks denote on which analyses each remark apply.

Analysis	Preparation/ fraction	Primary scan		Secondary scan		Remarks
		Exp.	Ref.	Exp.	Ref.	
Retention prop.	Bulk	1	1	–	–	
	Na-fines	1	1	–	–	
Swelling pressure	Trimmed	6	–	2	3	
Hydraulic cond.	Re-comp	6	–	–	3	
	Compacted	–	6	–	10*	* 4 dried
Triaxial tests	Trimmed	1	–	–	–	
	Compacted	–	1	–	–	
Unconfined	Sat. 4 cm	6	3	–	–	
Compression	Sat. 2 cm	6	3	6	6*	* Heated
Tests	Unsat. 2 cm	6	–	–	–	
Anion analysis (IC)	Water ext.	7	3	–	2	
Exchangable cations	Bulk	7	3	–	–	
Cation exchange	Bulk	26	4	–	–	* Greene-Kelly
Capacity (CEC)	Na-fines	14	2	13*	2*	
Element content	Bulk	7	3	7*	1*	* CBD-extraction
(ICP/AES+MS+EGA)	Na-fines	7	3	–	–	
XRD	Bulk	7	3	7	2	
	Mg-fines	4	2	–	–	
	Na-fines	–	–	7	1	(060) peak
SEM/TEM	Bulk	10	–	–	–	
	Na-fines	7	–	–	–	
Mössbauer	Bulk	4	2	1	1	
FTIR	Bulk	7	3	–	–	
	Na-fines	1	2	–	–	

1.3 Test material

The main part of the analyses was performed on samples obtained from the big sector from the 32° direction in Ring 4. The reason for selecting this particular big sector was that it was comparably intact after dismantling and that it did not contain any instruments.

The main part of the chemical/mineralogical analyses was performed on samples obtained by sawing pieces from the top level (A) of the big sector (Figure 1-7 and Figure 1-8). Each sample represented a radial width of 2 cm and was made large enough to supply material from the specific position for several of the planned tests (Figure 1-9). These samples were also devoted for the retention analyses. A sample representing the bentonite surface towards the heater was obtained by scraping 1–2 mm from the big sector specimen. Material was taken from the A as well as the B level in order to get sufficient amounts. A close-up of this surface is shown in Figure 1-10.

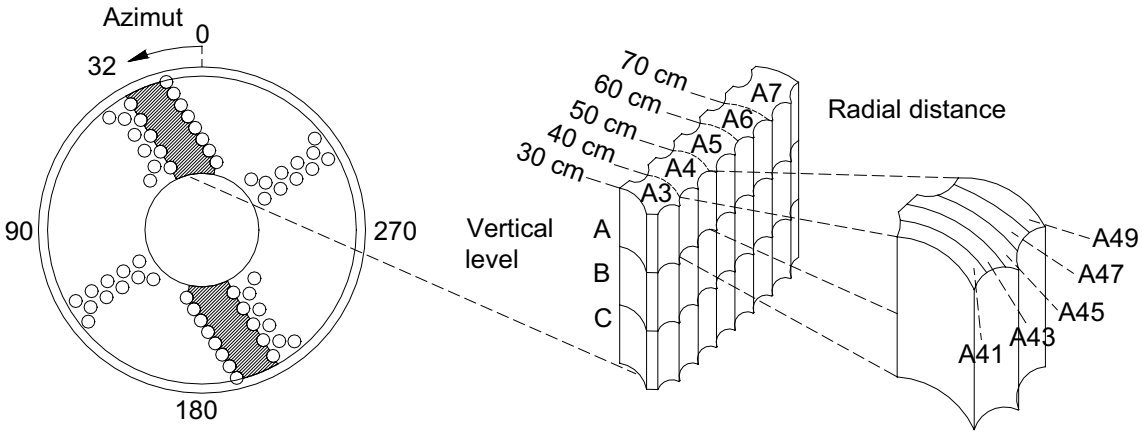

Figure 1-7. *Principle for denomination of specific sample positions. For handling of partitioned decimeter-thick specimens, the simple radial denomination in decimeters (e.g. A3 to A7) was used.*

Figure 1-8. *Big sector from Ring 4 in 32° direction and its partitioning.*

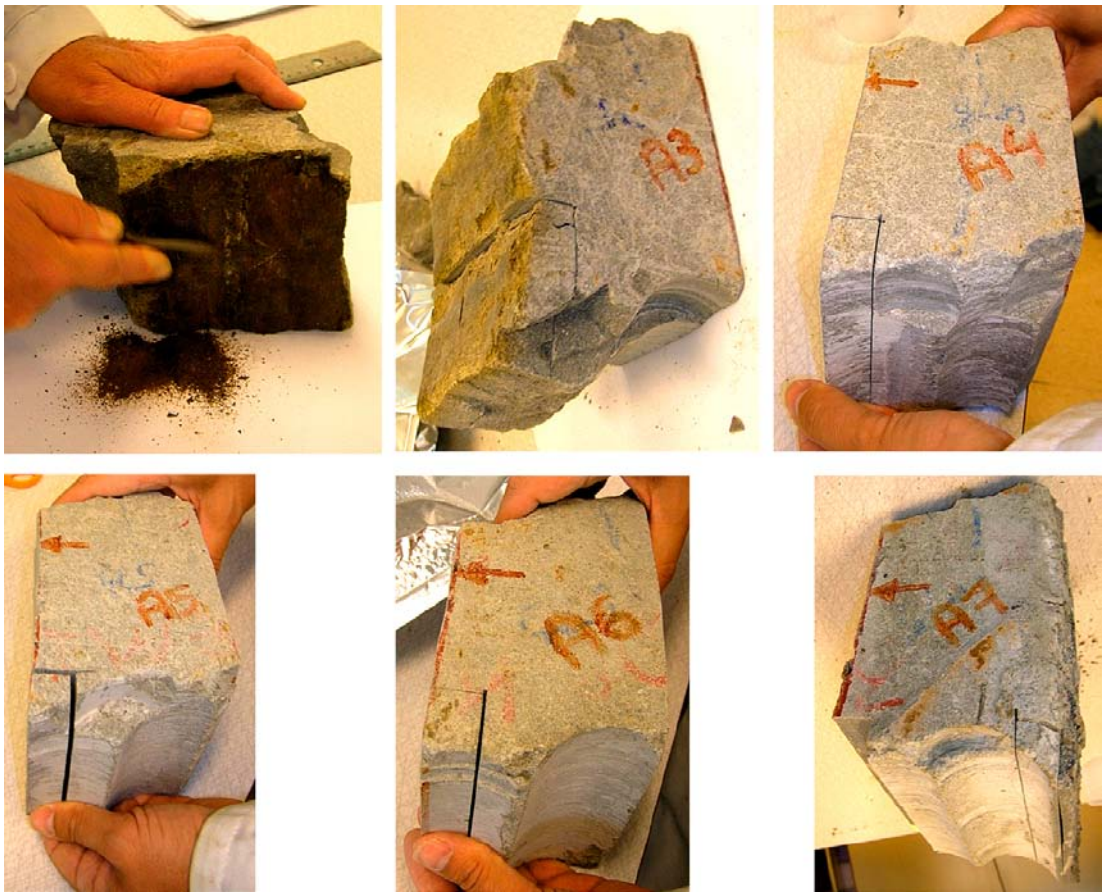

Figure 1-9. *Sampling for chemical/mineralogical analyses: TR04_032_A30 (upper left); TR04_032_A31 (upper middle); TR04_032_A41 (upper right); TR04_032_A51 (lower left); TR04_032_A61 (lower middle); TR04_032_A71 and TR04_032_A81 (lower right).*

Figure 1-10. *Close-up of surface towards heater on an inner piece from Ring 4, taken in 32° direction and A level.*

Samples devoted for the oedometer tests and the unconfined compression tests were obtained by core drilling (Figure 1-11). The radial positions of these cores largely corresponded with the positions of the sawed samples. In some cases, the radial positions had to be slightly modified in order to get intact material with no visible fractures, and for the innermost position almost all samples were taken from the B level.

Beam shaped samples, approximately 15 cm long, devoted for SEM analyses and XANES analyses (not presented in this report) were taken from an inner piece in Ring 4 and an outer piece of a big sector from Cylinder 2 (Figure 1-12 and Figure 1-13).

Dice-shaped samples with side lengths of a few centimeters and devoted for porosimetry analyses (not presented in this report) were taken from the big sector from Ring 4 in the 32° direction. Samples were taken from the following six positions: B31, A41, A51, A61, A72 and A80.

Special treatment was required for the Mössbauer analyses since these called for a more strict oxygen free handling. Inner pieces taken from Ring 3, were taken close to the heater, put in aluminum laminate bags, and evacuated as fast as possible. These bags were in turn put in plastic barrels, which were flushed with nitrogen. The actual sampling was made in glove box according to a scheme with four exposed samples representing the material at 10, 30, 50 and 90 mm distance from the heater (Figure 1-12 and Figure 1-14). The surface that was in contact with the heater was not considered for the Mössbauer analyses due to the likely contamination of material from the heater and the short exposure to air during dismantling. The samples were dried in the N_2-atmosphere inside the glove box before they were ground to a fine powder.

Figure 1-11. *Sampling for hydro-mechanical analyses. Specimens from Ring 4 in 32° direction. From B level close to heater (upper left), and from A level (all other photos);*

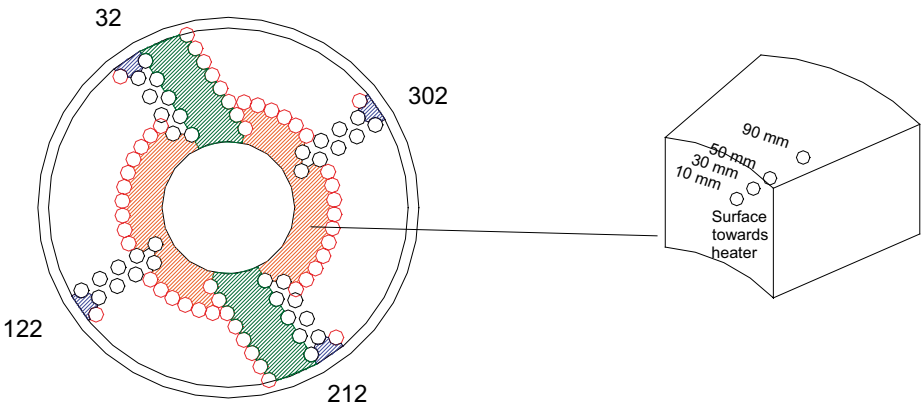

Figure 1-12. *Inner pieces and sampling for Mössbauer analysis.*

Figure 1-13. *Sampling for XANES and electron microscopy: inner piece from Ring 4 in 330° direction and B level (left) and outer piece from Cylinder 2 in 212° direction and B level (right).*

Figure 1-14. *Sampling for Mössbauer analysis in glove box. (TR03_250_C31, TR03_250_C33, TR03_250_C35 and TR03_250_C39)*

The denomination of a specific point (center of a volume) was made according to the following example:

TR04_032_A41b where:

T	TBT material
R04	block
032	azimuth direction (032° alt. 212°)
A	vertical level in block (A at the top, C at the bottom)
41	radial distance in centimeter from central line (30 denotes surface material)
b	bulk material (alt. c=clay fraction)

Reference material from a specific block was termed according to the following example:

TR04_R where :

T	TBT material
R04	block
R	reference material (non-compacted material saved at the compaction),

Ground water has been used in some of the hydro-mechanical analyses. For this purpose a small volume (approximately 5 liters) was taken from the borehole HD0025A, i.e. the same borehole as was used for the artificial saturation of the experiment during the first four years. This volume was analyzed for the composition of main components, through ICP-AES, ion chromatography and TOC Analyzer (see Table 1-4). The salt content (NaCl) was approximately 0.4%. This concentration was generally lower than what previously was analyzed for the same borehole (cnf. Table 1-1).

Table 1-4. Main components in groundwater used for some hydro-mechanical analyses.

Na mM	K mM	Ca mM	Mg mM	TOC mM	IC mM	Cl mM	SO_4-S mM	Br mM	F mM	Si mM
55.7	1.74	4.13	5.02	1.26	1.82	64.9	2.82	0.147	0.0418	0.161

2 Hydro-mechanical analyses

2.1 General

The following hydro-mechanical tests were run and described in this chapter:

- retention curve determinations
- hydraulic conductivity and swelling pressure tests
- unconfined compression tests
- triaxial tests

2.1.1 Basic geotechnical properties

The base variables water content w (%), void ratio e, and degree of saturation S_r (%) were determined according to Equations (2-1) to (2-3).

$$w = 100 \cdot \frac{m_{tot} - m_s}{m_s} \tag{2-1}$$

$$e = \frac{\rho_s}{\rho}(1 + w/100) - 1 \tag{2-2}$$

$$S_r = \frac{\rho_s \cdot w}{\rho_w \cdot e} \tag{2-3}$$

where

m_{tot} = total mass of the specimen (kg)

m_s = dry mass of the specimen (kg)

ρ_s = particle density (kg/m^3)

ρ_w = density of water (kg/m^3)

ρ = bulk density of the specimen (kg/m^3)

The dry mass of the specimen was obtained from drying the wet specimen at 105°C for 24 h. The bulk density was calculated from the total mass of the specimen and the volume determined by weighing the specimen above and submerged into paraffin oil.

For determination of void ratio and degree of saturation the particle density ρ_s = 2,780 kg/m^3 and water density ρ_w = 1,000 kg/m^3 were used.

2.2 Retention curves

2.2.1 General

The water retention curve is the relation between the water content and the energy state or potential of the soil water at equilibrium, expressed as relative humidity or suction. The retention curve is here presented as water content versus relative humidity. When starting with an initial water content of 0% the resulting curve is the basic retention curve while the so called specific retention curve is determined on material with an initial water content deviating from 0%. Both curves are determined under free swelling conditions.

The water content, w, is defined as mass of water per mass dry substance, see section 2.1.1. The relative humidity is the ratio between the partial vapour pressure p and the vapour pressure at saturation p_s in%, $RH = 100 \cdot \frac{p}{p_s}$.

The method used for the determination of retention curves was an experimentally simple method described below (see also Wadsö et al. 2004).

2.2.2 Test equipment

The equipments used for the analyses were glass jars, an analytical balance and a drying oven. Each specimen was placed in a metal cage and suspended inside a glass jar with a tight lid. A rod passing through the lid made it possible to weigh the specimens below the balance without having to remove them from the jars. A plastic sealing washer was placed around the rod such that the generated *RH* was maintained during the course of the experiment. The design is presented in Figure 2-1.

2.2.3 Preparation of specimen and test procedure

Four test series were run: two with material from the field experiment and two with reference material. From each of the materials both the bulk material and the Na-converted fine fraction were analyzed. The initial water contents of the bulk specimens were 20.5% and 18% and the initial water contents of the Na-converted specimens were 1.6% and 1.5%.

Each jar contained a salt solution, which generated a constant relative humidity. The measurements were carried out at eight different *RH* values (0%, 11%, 33%, 58%, 75%, 84%, 93%, 97%). These *RH* values were achieved using various saturated salt solutions (LiCl, $MgCl_2$, NaBr, NaCl, KCl, K_2SO_4) except in the cases of *RH* = 0% and 93% were molecular sieve and an unsaturated NaCl solution, respectively, were used. The *RH* values for the saturated salt solutions were taken from Greenspan (1977) and the vapour pressure above the 2 molal NaCl solution was taken from Clarke and Glew (1985). The jars were placed in an oven at a constant temperature of 25°C. The unsaturated solution was replaced with a new mixture on an almost weekly basis such that a constant humidity could be maintained in the jar.

The mass of each sample was measured, with the sample still inside the jar, at regular intervals. When some kind of equilibrium state was reached the test was finished by drying the samples at 105°C during 24 h whereby the dry mass was quantified. The final water content was then calculated from the total mass before the drying and the dry mass determined after the test. Whether the

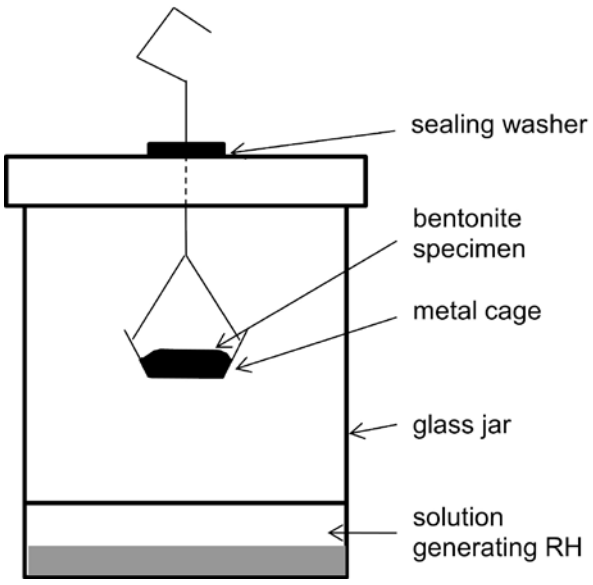

Figure 2-1. *Schematic view showing the test equipment.*

equilibrium state was reached, was evaluated by a limit of the parameter Ω, Equation (2-4) where m is the mass (g) and t is the time (s). The parameter and the limit value $\Omega \leq 5 \cdot 10^{-9}$ s^{-1} were suggested by Wadsö et al. (2004).

$$\Omega = \frac{dm}{dt} \times \frac{(RH_f - RH_i)/100}{m(t) - m_i} \tag{2-4}$$

The subscripts f and i refer to the initial and final states, respectively. In the evaluation of Ω, the initial relative humidity was set to RH_i = 75%, 80%, and 1% for the materials with initial water contents of w_{ini} = 18%, 21%, and 2%, respectively.

2.2.4 Results

The final measured water contents for the four series are presented in Table 2-1 and in Figure 2-2. The limit of Ω was achieved for all specimens but one, marked in Table 2-1. This specimen had almost the same final as initial mass and since the change in mass is used in the denominator in Equation (2-4) the value of Ω will be sensitive to even small changes in mass. However, the value before the last one was well within the criterion also for this specimen.

Table 2-1. Final water contents w_f(%) determined with the jar method at 25°C after dismantling. The specimens were prepared either as bulk samples (powder or pieces) or as Na converted fine fraction of powder samples (Na-fines).

Material	Preparation	Initial water content	mol. sieve RH(%) 0	LiCl RH(%) 11	$MgCl_2$ RH(%) 33	NaBr RH(%) 58	NaCl RH(%) 75	KCl RH(%) 84	NaCl 2m RH(%) 93	K_2SO_4 RH(%) 97
TR04_R	powder	18.0	0.2	2.7	9.1	15.2	18.1	20.3	24.6	36.1[2]
TR04_032_A31	pieces	20.5	0.3	3.3	10.6	17.3	20.3	21.7	23.9	33.1[2]
TR4_R	Na-fines	1.5	0.1	1.5	4.1	10.1	18.9	23.0	30.1	44.5
TR04_032_A31	Na-fines	1.6	0.2	1.4[1]	4.4	10.6	19.4	23.6	30.5	43.1

[1] $\Omega > 5 \cdot 10^{-9}$ s^{-1}.

[2] Longer testing time than other specimens.

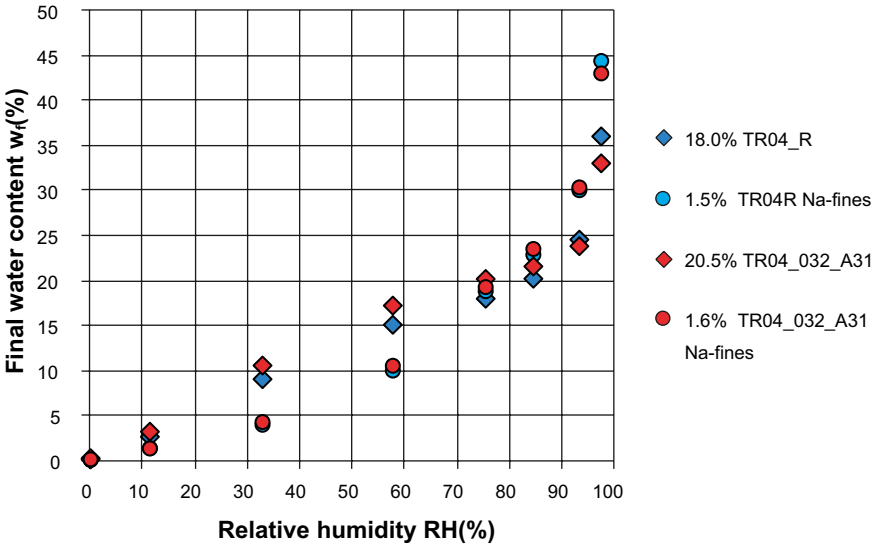

Figure 2-2. *Final water contents w_f determined with the jar method at 25°C after dismantling. The specimens were prepared either as bulk samples (diamonds) or as Na-converted fine fraction (circles). The colours blue and red denote reference material and material from the field experiment, respectively. The initial water contents are given in the labels.*

To achieve the limit of Ω, different testing times were used for the different specimens. For most of the specimens less than 3,000 h was needed but two specimens were kept in their environments for about 8,000 h, marked in Table 2-1. The time evolutions of water contents from all series are shown in Figure 2-3 where the bulk specimen from the field material placed at RH = 97% changed the most. A second set of results was evaluated as the water content after a specific time together with the difference between the maximum and the minimum water content Δw between that specific time and the dismantling. The water content at the specific time 2,000 h w_t and the corresponding differences Δw are shown in Table 2-2 and Table 2-3, respectively.

Table 2-2. The water content determined with the jar method at 25°C and evaluated at the specific time 2,000 h w_t(%). The specimens are the same as presented in Table 2-1.

Material	Preparation	Initial water content	mol. sieve RH(%) 0.0	LiCl RH(%) 11.3	$MgCl_2$ RH(%) 32.8	NaBr RH(%) 57.6	NaCl RH(%) 75.3	KCl RH(%) 84.4	NaCl 2m RH(%) 93.1	K_2SO_4 RH(%) 97.3
TR04_R	powder	18	0.2	2.8	9.2	15.2	18.0	20.3	24.2	35.2
TR04_032_A31	pieces	20.5	0.4	3.5	10.8	17.4	20.5	21.8	23.9	29.4
TR04_R	Na-fines	1.5	0.0	1.3	4.0	10.0	18.8	22.9	29.9	44.8
TR04_032_A31	Na-fines	1.6	0.2	1.3	4.3	10.5	19.3	23.6	30.6	42.4

Table 2-3. Differences between maximum and minimum water contents Δw after the specific time 2,000 h.

Material	Preparation	Initial water content	mol. sieve RH(%) 0.0	LiCl RH(%) 11.3	$MgCl_2$ RH(%) 32.8	NaBr RH(%) 57.6	NaCl RH(%) 75.3	KCl RH(%) 84.4	NaCl 2m RH(%) 93.1	K_2SO_4 RH(%) 97.3
TR04_R	powder	18	0.0	0.1	0.1	0.0	0.1	0.1	1.2	1.0
TR04_032_A31	pieces	20.5	0.1	0.2	0.1	0.0	0.1	0.1	0.2	5.3
TR04_R	Na-fines	1.5	0.0	0.1	0.1	0.0	0.1	0.1	0.4	0.5
TR04_032_A31	Na-fines	1.6	0.1	0.1	0.1	0.0	0.0	0.1	0.4	1.1

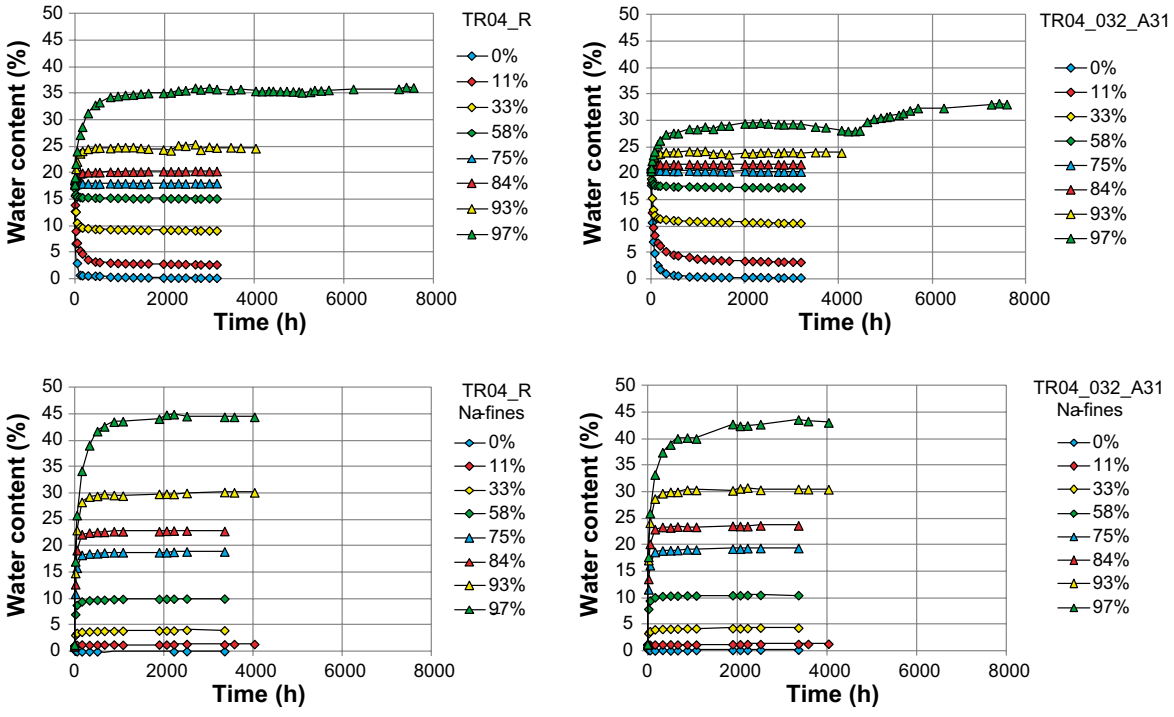

Figure 2-3. Time evolutions of water contents from all test series. The legends show the relative humidity RH(%) above each salt used.

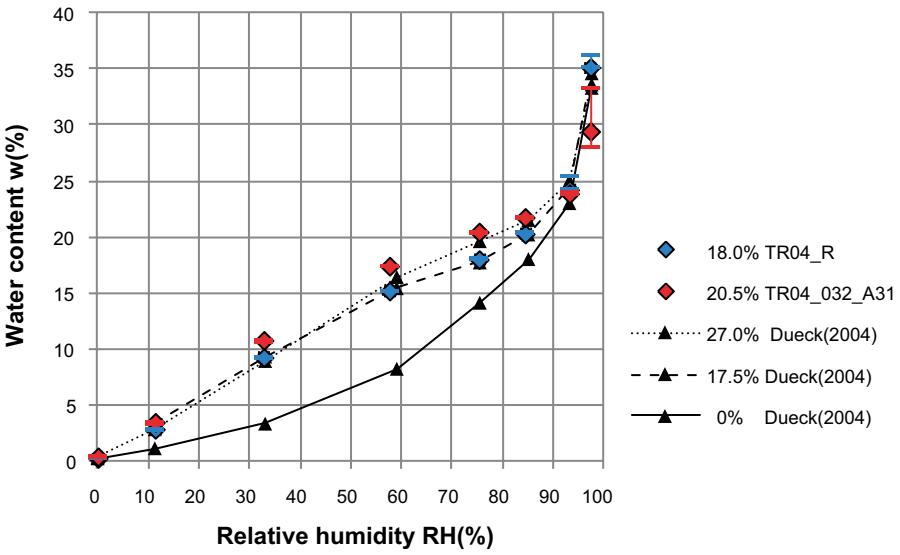

Figure 2-4. *Retention curves determined with the jar method at 25°C. The initial water contents are given in the labels. The colours blue and red denote reference material and material from the field experiment, respectively. Results from a previous study is also shown.*

2.2.5 Discussion

The results from the bulk material, from Table 2-2 and Table 2-3 are presented in Figure 2-4 with comparable results presented by Dueck (2004). The maximum and minimum of water content after 2,000 h are marked as error bars from each measurements made at 2,000 h.

The results from the bulk materials, both reference material and material from the field experiment, coincided well with previous results on bulk material of MX-80 taking the initial water contents into account. However, the water content of the specimens from the field material placed at $RH = 97\%$ deviates. This specimen was the same as previously commented on.

Regarding the test results from the specimens of Na converted fine fraction, Figure 2-2, no large difference was seen between the reference material and the material from the field experiment.

2.3 Hydraulic conductivity and swelling pressure

2.3.1 General

The hydraulic conductivity and swelling pressure were determined in combined tests in a swelling pressure device. The parameters are functions of the density of the sample and the chemical composition of the water and the buffer material (Karnland et al. 2006).

2.3.2 Test equipment

The hydraulic conductivity and swelling pressure were determined by use of the test equipment shown in Figure 2-5, made of acid proof stainless steel. The specimens were confined by a cylinder ring with a diameter of 35 mm or 20 mm and stainless steel filters at the top and bottom. The test volume was sealed by o-rings placed between the bottom plate and the cylinder ring and between the piston and the cylinder ring. At test start the height of the test volume was fixed to approximately 10 mm.

The axial force from the samples was determined by the load cell placed between the piston and the upper lid. The displacement of the piston due to transducer deformation is 25 µm at maximum force, which consequently corresponds to 0.25% of the sample height which was considered insignificant.

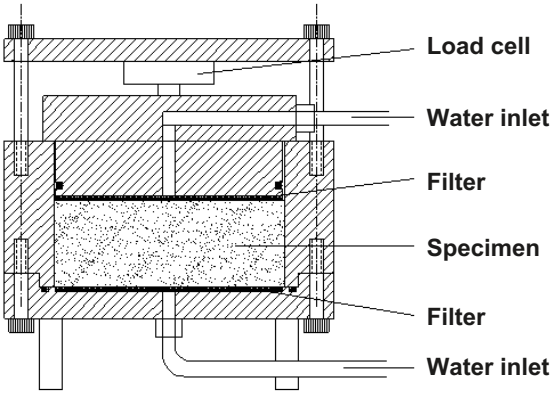

Figure 2-5. *A schematic drawing of the swelling pressure device.*

2.3.3 Preparation of specimen and test procedure

Two series were run, series 1 and 2. In series 1 three types of specimens were tested; reference specimens and specimens from the field experiment prepared in two different ways. The reference specimens were compacted from material saved from the block production to dry densities between 1,300 kg/m^3 and 1,680 kg/m^3. The specimens from the field experiment were prepared in the following ways:

- Trimmed to fit the sample holders and thus having a density close to the field value.
- Air-dried, ground to a grain size similar to the original MX-80 powder and re-compacted to a dry density of approximately 1,570 kg/m^3.

In this way series 1 consisted of all specimens from the primary scan and some specimens from the secondary scan while series 2 consistsed of the remaining part which was also the main part of the specimens from the secondary scan. The test series 2 was run on reference material but prepared differently compared to the reference specimens in series 1. The specimens in series 2 were prepared in one of the following ways:

- Drilled or ground and re-compacted from saturated larger specimens of reference material.
- Compacted from almost dry material, either dried at 105°C during 24 h or at 40°C and subsequent kept in a dry environment during 4 days.

The specimens were saturated or re-saturated after preparation by introducing water to the bottom side a couple of days before adding water also to the top side. Water was added after evacuation of air from filters and tubes by a vacuum pump. For all specimens ground water from the TBT test site, Table 1-4 was used. During the saturation a minor water pressure of approximately 2 kPa was applied. The swelling pressure was measured continuously.

After saturation of the specimens a pore pressure gradient was applied over each specimen. The gradient during the tests was between 2,000 and 40,000 m/m which corresponded to pore pressure differences of 150 kPa and 4,000 kPa over the sample height. The measurements of the outflow were made during several days in order to get stable values of the evaluated hydraulic conductivity which was calculated according to Darcy's law. The water pressure was thereafter reduced to zero and the test was terminated when the recorded axial force was stable. The swelling pressure was evaluated just before the termination and dismantling. The water content and density were determined according to section 2.1.1 after the tests.

2.3.4 Results

The results from measurements of swelling pressure and hydraulic conductivity in series 1 and 2 are given in Table 2-4 and Table 2-5, respectively.

The results from series 1 are plotted as a function of dry density in Figure 2-6 and Figure 2-7. In the diagrams the colours red, orange, yellow, light green, dark green, and blue denote the positions; 31–35, 42, 52, 62, 72, and 80 cm, respectively from the heater. In addition, the trimmed specimens and the ground and re-compacted specimens are marked with circles and triangles, respectively. The references are marked with solid black diamonds and the dashed lines represent exponential best fit lines.

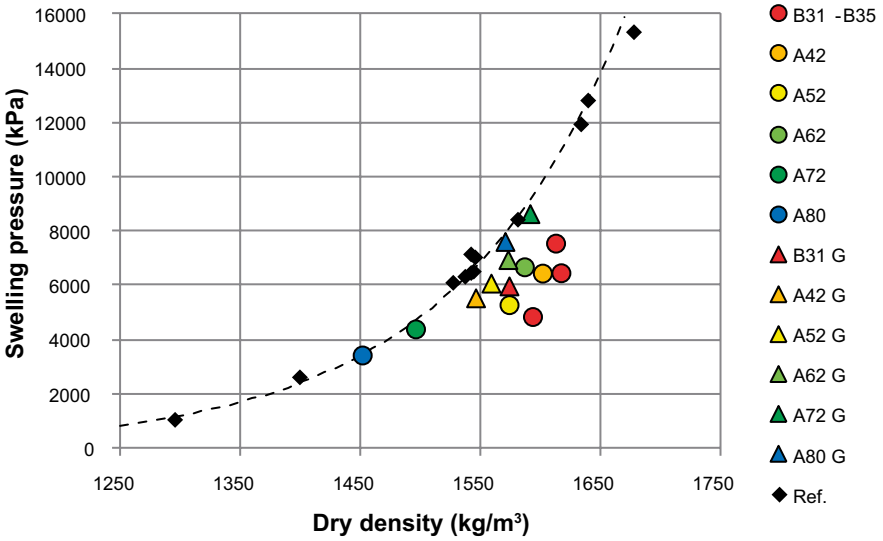

Figure 2-6. The determined swelling pressure as a function of dry density from series 1. From the warmest to the coldest the colours red, orange, yellow, green and blue are used. Black diamonds denote references. Circles and triangles denote trimmed and ground and re-compacted specimens, respectively. The labels give information about the radial positions in the specific direction of block TR04_032. The label Ref. denotes the reference material TR04_R. The letter G in the labels denote ground re-compacted specimens.

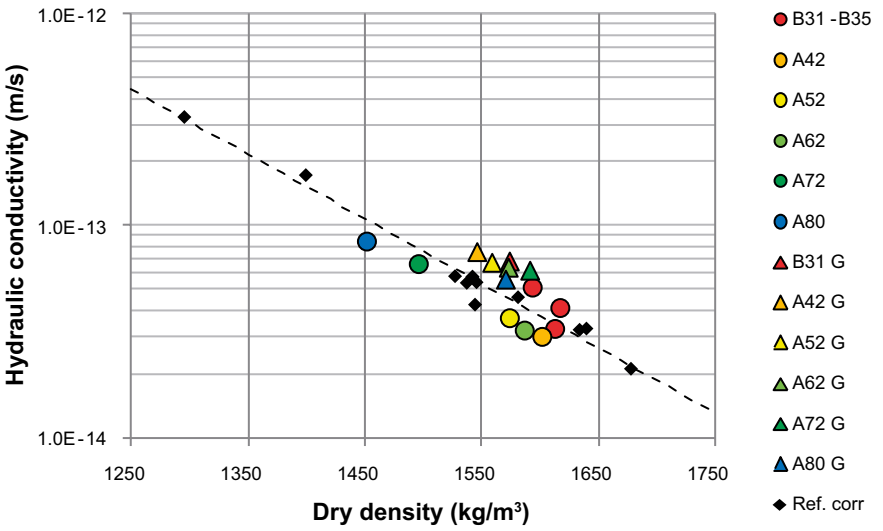

Figure 2-7. The determined hydraulic conductivity as a function of dry density from series 1. The calculated hydraulic conductivity is corrected for evaporation from tubes. The labels, markers and colours from Figure 2-6 are used.

Table 2-4. Results from the measurements of swelling pressure and hydraulic conductivity from series 1.

Material	Preparation	Diameter of specimen D mm	Dry density ρ_d kg/m^3	Water content w %	Void ratio e –	Degree of saturation S_r %	Swelling pressure P_s kPa	Gradient I m/m	Hydraulic conductivity k_w ·10^{-14} m/s
TR04_032_B31	drilled	20	1,610	26.0	0.72	100	7,600	13,000	2.4
TR04_032_B33	drilled	35	1,620	25.8	0.72	100	6,500	7,400	3.5
TR04_032_B35	drilled	35	1,590	26.3	0.75	98	4,900	7,400	4.6
TR04_032_A42	drilled	35	1,600	26.6	0.74	100	6,500	12,000	2.7
TR04_032_A52	drilled	35	1,570	27.6	0.77	100	5,300	11,000	3.4
TR04_032_A62	drilled	35	1,590	27.0	0.75	100	6,700	12,000	2.9
TR04_032_A72	drilled	35	1,500	30.9	0.86	100	4,400	7,700	6.2
TR04_032_A80	drilled	35	1,450	33.2	0.92	101	3,400	7,700	8.1
TR04_032_B31	ground and compacted	35	1,570	27.9	0.77	101	6,000	12,000	6.5
TR04_032_A42	ground and compacted	35	1,550	28.3	0.80	99	5,500	12,000	7.3
TR04_032_A52	ground and compacted	35	1,560	27.8	0.78	98	6,100	12,000	6.4
TR04_032_A62	ground and compacted	35	1,570	27.4	0.77	99	7,000	12,000	6.1
TR04_032_A72	ground and compacted	35	1,590	26.9	0.75	100	8,600	12,000	5.9
TR04_032_A80	ground and compacted	35	1,570	27.6	0.77	99	7,600	12,000	5.3
TR04_R R1	compacted	20	1,680	23.2	0.66	98	15,300	40,000	1.7
TR04_R R2	compacted	35	1,640	24.5	0.70	98	12,800	12,000	2.8
TR04_R R3	compacted	35	1,630	24.9	0.70	99	11,900	12,000	2.8
TR04_R R4	compacted	35	1,540	29.4	0.81	101	6,300	13,000	5.0
TR04_R R5	compacted	35	1,400	36.4	0.99	103	2,600	2,000	14.2
TR04_R R6	compacted	35	1,300	41.8	1.15	101	1,000	2,000	29.6
TR04_R R10	compacted	35	1,530	29.4	0.82	100	6,100	11,700	5.9
TR04_R R11	compacted	35	1,580	27.2	0.76	100	8,400	12,200	4.7
TR04_R R12	compacted	35	1,540	28.8	0.80	100	6,500	11,900	4.3
TR04_R R13	compacted	35	1,550	28.9	0.80	101	7,000	12,000	5.5
TR04_R R14	compacted	35	1,540	28.7	0.80	99	6,400	12,000	5.8
TR04_R R15	compacted	35	1,540	29.1	0.80	101	7,100	12,000	5.8

Table 2-5. Results from the measurements of swelling pressure and hydraulic conductivity from series 2.

Material	Preparation	Diameter of specimen D mm	Dry density ρ_d kg/m^3	Water content w %	Void ratio e –	Degree of saturation S_r %	Swelling pressure P_s kPa	Gradient I m/m	Hydraulic conductivity k_w ·10^{-14} m/s
TR04_R PR1	ground[1]	35	1,610	26.0	0.73	100	10,200	12,000	5.0
TR04_R PR2	ground[1]	35	1,600	26.5	0.73	100	10,600	12,000	5.1
TR04_R PR3	ground[1]	35	1,620	25.7	0.72	99	12,100	12,000	5.0
TR04_R PR4	drilled	35	1,530	29.2	0.81	100	5,500	12,000	5.0
TR04_R PR5	drilled	35	1,540	28.8	0.81	99	5,900	12,000	7.8
TR04_R PR6	drilled	35	1,530	29.2	0.81	100	6,000	12,000	6.3
TR04_R PR10	dried and ground[1,2]	35	1,530	29.0	0.81	99	5,300	6,900	9.5
TR04_R PR11	dried and ground[1,2]	35	1,570	27.7	0.77	100	6,300	7,100	8.2
TR04_R PR12	dried and ground[1,3,4]	35	1,650	23.8	0.69	97	11,700	10,800	5.1
TR04_R PR13	dried and ground[1,3,4]	35	1,660	23.2	0.67	96	12,700	11,200	4.6

[1]and compacted.

[2]dried at 105°C,

[3]dried at 40°C,

[4]At saturation, water was added to both sides simultaneously.

The swelling pressures given in Table 2-4 and Table 2-5 were determined after the measurement of hydraulic conductivity just before the dismantling, P_{sf}. The swelling pressure was also measured at saturation just before the introduction of water pressure, introduced for the measurement of hydraulic conductivity, P_{sb}. The difference in percentage between these measurements $(P_{sf}-P_{sb})/P_{sf}$ was less than 10%. The differences for the specimens in series 1 are shown as error bars in Figure 2-8.

The hydraulic conductivity given in Table 2-4 and Table 2-5 was given without consideration of evaporation, k_w. However, evaporation in the outflow of water is one possible source of error in this kind of measurement and consequently the hydraulic conductivity was also evaluated taking evaporation into account, $k_{w,corr}$. The difference in percentage $(k_{w,corr}-k_w)/k_{w,corr}$ was less than 30% for all measurements. The differences in series 1 are shown as error bars in Figure 2-9.

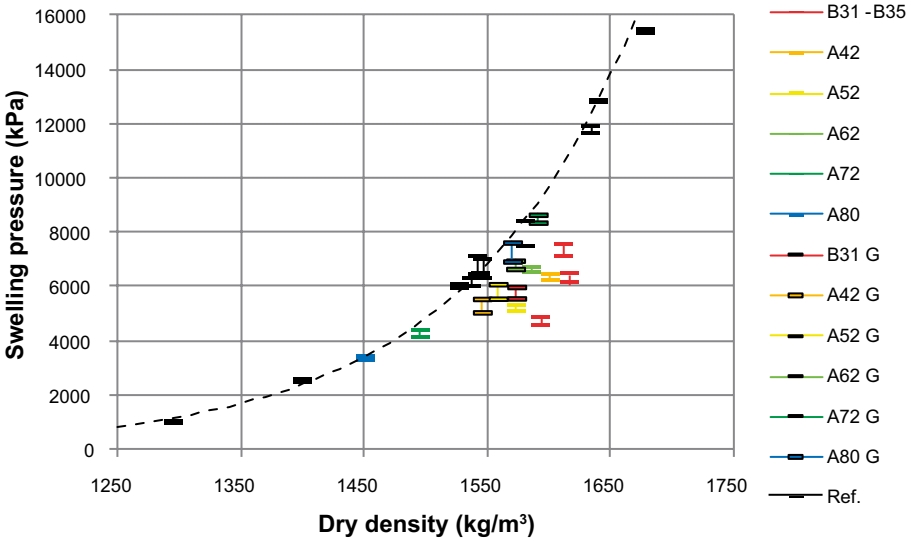

Figure 2-8. *Swelling pressure and corresponding errors, cf. Figure 2-6.*

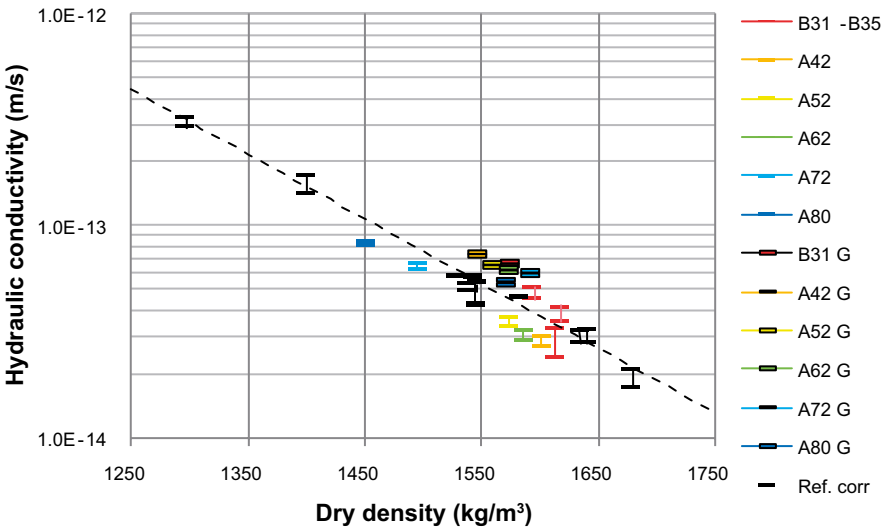

Figure 2-9. *Hydraulic conductivity and corresponding errors, cf. Figure 2-7.*

The variability in the methods was studied in the secondary scan and the results from series 2 are shown with unfilled markers in Figure 2-10 and Figure 2-11. The unfilled markers triangles, circles, and squares denote ground and re-compacted, trimmed, and compacted from dried material, respectively. Also used for the evaluation of variability was the reference specimens R10–R15, marked with black solid diamonds as the other reference specimens prepared in the same way. From the results from series 2 the following comments can be made regarding the swelling pressure;

- the scatter was approximately 10%,
- no large deviation between the results from specimens prepared by compaction, by drilling or by ground and re-compaction,
- a trend of decreased swelling pressure was seen on compacted dried material.

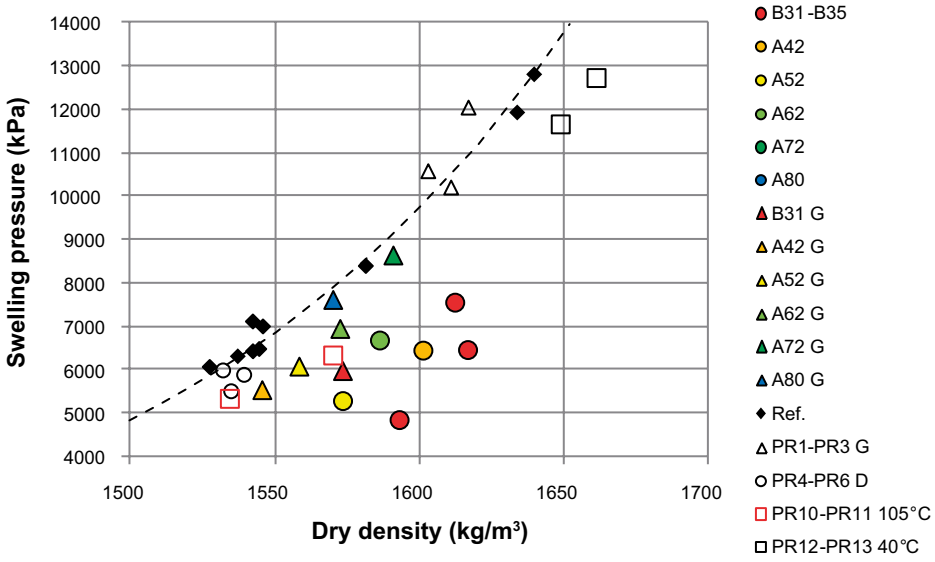

Figure 2-10. *Swelling pressure from test series 2 shown with results from Figure 2-6. In the labels for specimens in series 2 G, D, 105°C and 40°C denote ground re-compacted, drilled, dried at 105°C and dried at 40°C respectively.*

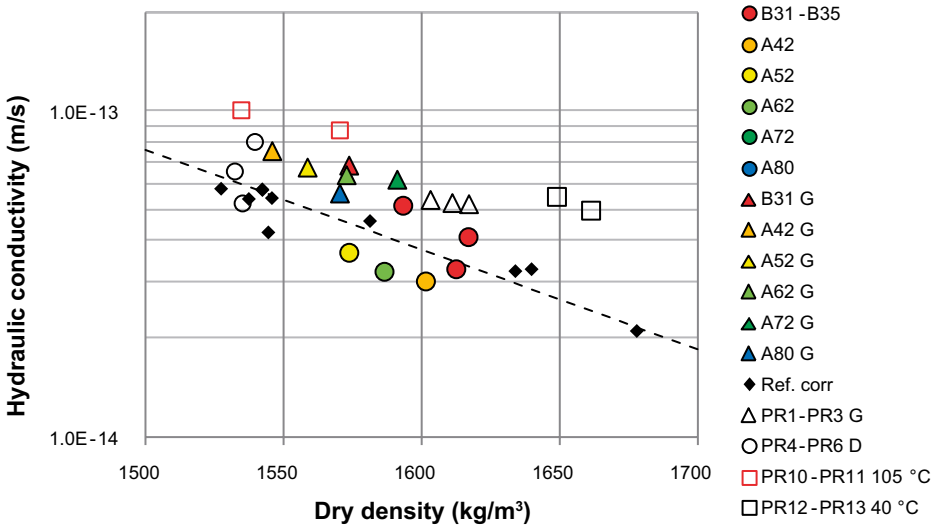

Figure 2-11. *Hydraulic conductivity from test series 2 shown with results from Figure 2-7.*

From the results from series 2 the following comments can be made regarding the hydraulic conductivity;

- the scatter was approximately 30%,
- no deviation between the results from specimens prepared by compaction and those prepared by drilling, however a scatter,
- a trend of increased hydraulic conductivity resulting from specimens ground and re-compacted compared to reference specimens only prepared by compaction,
- a trend of increased hydraulic conductivity from specimens prepared from almost dry material.

2.3.5 Discussion

Based on this investigation, where properties of material exposed to adverse conditions were compared to those of reference material, the following were found;

- a reduction in swelling pressure was observed on re-saturated specimens, especially on those from the innermost part,
- a scatter in hydraulic conductivity but a tendency towards an increase on re-saturated specimens drilled from the innermost part was seen. This was also observed on ground and re-compacted reference specimens.

From Figure 2-10 and Figure 2-11 it could be seen that drying the material might influence by decreasing the swelling pressure and increasing the hydraulic conductivity. In addition, the results presented in Figure 2-6 and Figure 2-7 could be compared to results from previous studies on the same type of material, Figure 2-12 and Figure 2-13. When making a comparison the swelling pressure from the innermost specimens of the field experiment is still deviating and less than the references. However, regarding the hydraulic conductivity the previously discussed deviation from reference specimens should instead be interpreted as a scatter.

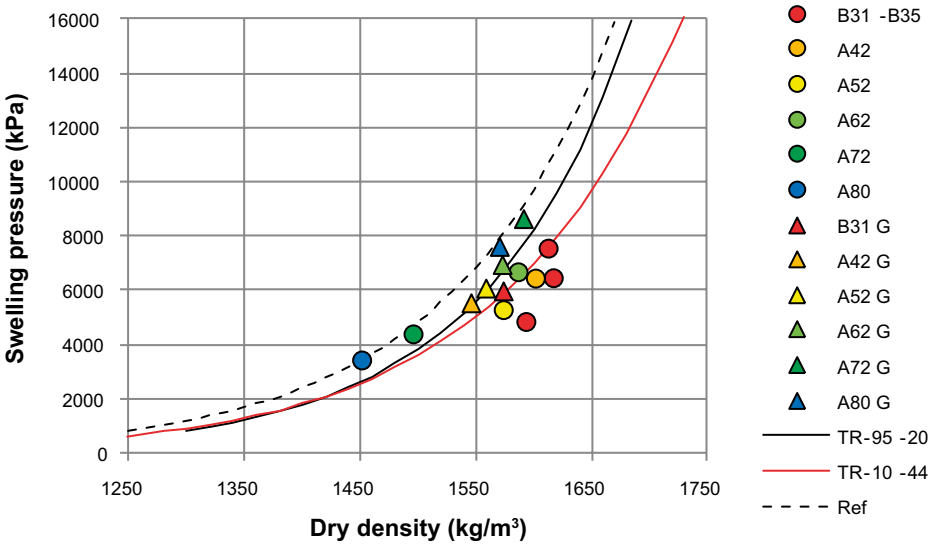

Figure 2-12. *Results from Figure 2-6 compared with results from Börgesson et al. (1995) (label: TR-95-20) and Åkesson et al. (2010) (label: TR-10-44).*

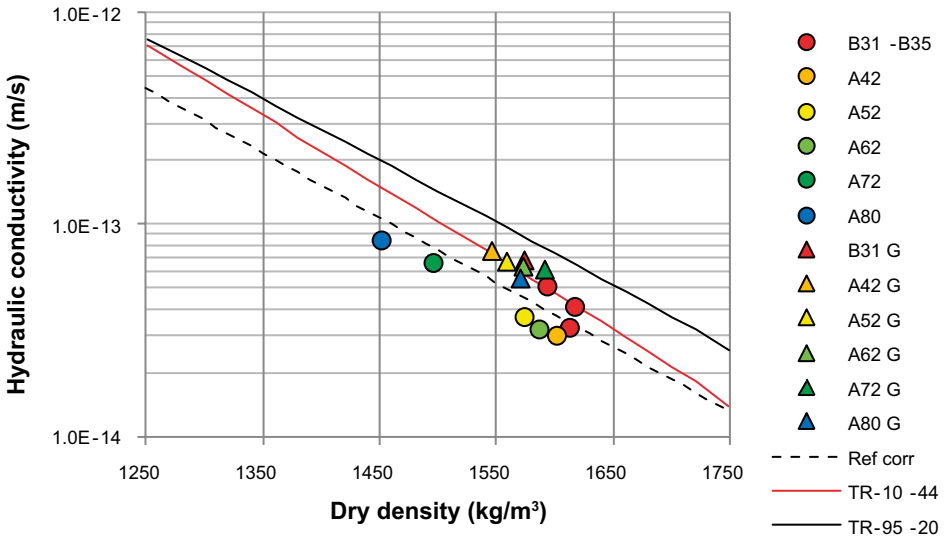

Figure 2-13. *Results from Figure 2-7 compared with results from Börgesson et al. (1995) (label: TR-95-20) and Åkesson et al. (2010) (label: TR-10-44).*

2.4 Triaxial tests

2.4.1 General

The strength of soil materials is preferably evaluated from triaxial tests. A description concerning technique and evaluation was given by Börgesson et al. (1995).

2.4.2 Test equipment

The test specimens were pre-saturated in a cylindrical saturation device equipped with a cylindrical steel filter to achieve radial saturation. A piston allowed for measurement of the axial swelling pressure during the saturation. The device was axially divisible in order to enable removal of the specimens without use of axial force.

A high pressure triaxial cell was used for the tests. The cell was equipped with standard strain gauges, force transducer and pore pressure transducers according to Figure 2-14.

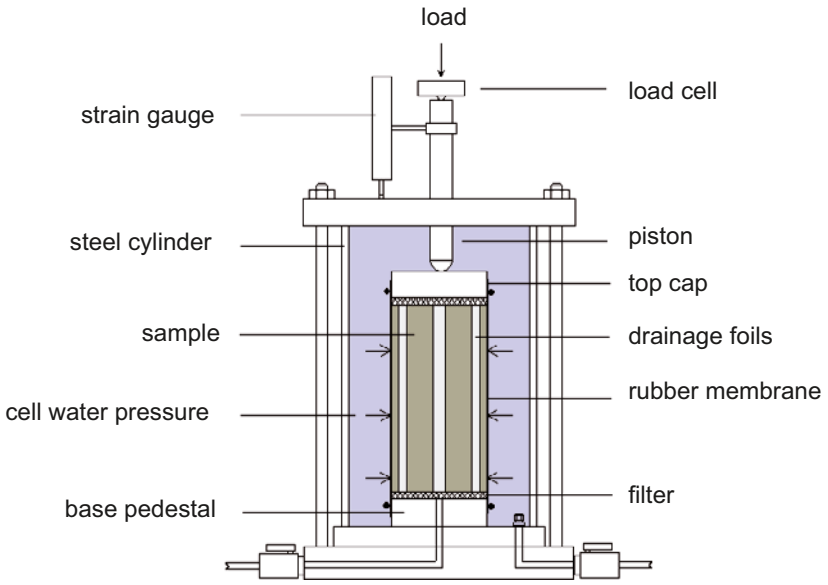

Figure 2-14. *Triaxial test equipment used in combination with a mechanical press.*

2.4.3 Preparation of specimen and test procedure

The technique requires relatively large test specimens and is resource consuming, both with respect to time and active work. The test series were therefore limited to two specimens; one from the field experiment and one reference specimen. The specimen from the field experiment was sampled from the vertical position B of the innermost part and 7 cm from the heater, i.e. at position B37.

A cylindrical specimen was prepared from material from the field experiment by sawing a rough work piece which was trimmed to a cylindrical form with a diameter of 35 mm and a height of 70 mm. The reference specimen was compacted from material saved from the block production to the same dimensions and was water saturated in the same saturation device as used for the specimen from the field experiment.

After approximately 4 weeks in the saturation device the specimens were mounted in the triaxial cell, Figure 2-14, and a cell pressure corresponding to the swelling pressure measured during the saturation was applied. The valve to the pedestal was kept closed during an equilibration period and the pore pressure u at the base pedestal was measured. Filter paper drains along the samples were used to accelerate the equalization of the pore pressure over the sample height. During both saturation and shearing ground water from the TBT test site, Table 1-4, was used.

Axial load was applied by use of a mechanical press when pressure equilibrium was reached. A constant shear rate of approximately 4 mm/week ($0.7 \cdot 10^{-5}$ mm/s) was used. In both tests the pore pressure was 500 kPa or higher at the start of the shearing, in order to avoid problems with air. After failure the water content and the density of the specimens were determined according to section 2.1.1.

During the tests the cell pressure σ_3, pore pressure u, deformation Δl, and axial force F were continuously measured. The samples were considered as undrained during shearing and no volume change was taken into account. The deviator stress was calculated from:

$$q = \frac{F}{A_0}\left(\frac{l_0 - \Delta l}{l_0}\right) \tag{2-5}$$

where A_0 is the specimen initial cross section area and l_0 the initial length of the sample. The contact area between load piston and top-cap was considered insignificant.

The vertical total stress σ_1 was calculated from:

$$\sigma_1 = q + \sigma_3 \tag{2-6}$$

The average effective stress p' was calculated from:

$$p' = \frac{1}{3}(\sigma_1 + 2\sigma_3 - 3u) \tag{2-7}$$

The strain ε was calculated from:

$$\varepsilon = \frac{\Delta l}{l_0} \tag{2-8}$$

2.4.4 Results

In Table 2-6 the results from the triaxial tests are shown in terms of final water contents, densities, stresses, and strains at maximum deviator stress. The swelling pressures measured during water saturation in the saturation device are also shown. The deviator stress versus strain resulting from the triaxial tests is shown in Figure 2-15 and the stress paths are plotted as deviator stress versus mean effective stress in Figure 2-16.

Table 2-6. Results from the triaxial tests.

	From saturation device		After removal from triaxial cell				At maximum deviator stress				
Material (Preparation)	**Dry density ρ_d kg/m³**	**Swelling pressure P_s kPa**	**Dry density ρ_d kg/m³**	**Water content w %**	**Void ratio e –**	**Degree of saturation S_r %**	**Cell pressure σ_3 kPa**	**Pore pressure u kPa**	**Effective stress p' kPa**	**Deviator stress q_{max} kPa**	**Strain at q_{max} ε %**
TR04_032_B37 (trimmed)	1,670	9,900	1,660	23.9	0.67	99	10,830	1,360	11,120	4,970	3.3
TR04_R (compacted)	1,620	10,900	1,625	25.5	0.71	100	11,230	1,480	10,890	3,370	7.6

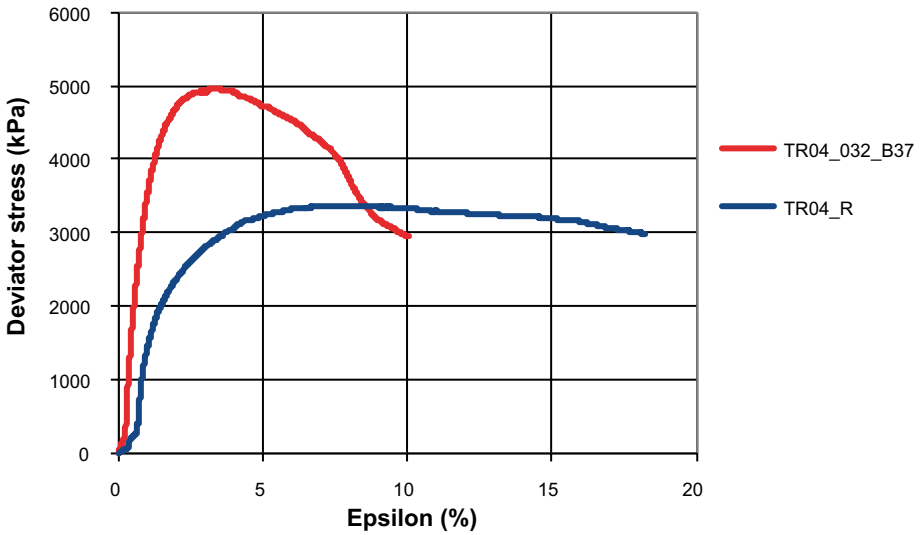

Figure 2-15. Deviator stress versus strain resulting from the triaxial tests.

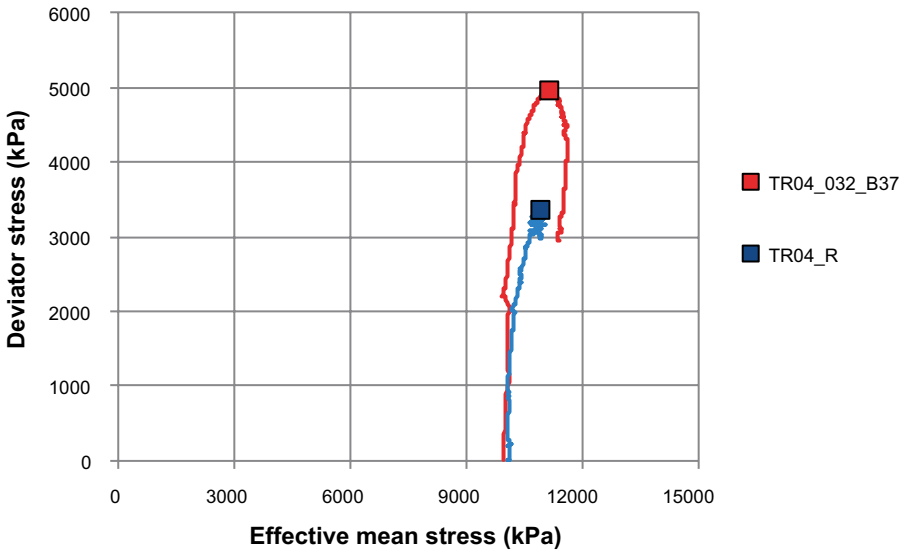

Figure 2-16. Stress paths plotted as deviator stress versus mean effective stress.

The stiffness as well as the deviator stress at failure were larger in the specimen from the field experiment compared to the reference specimen. In addition, the effective means stress was approximately the same in spite of the higher dry density in the specimen from the field experiment. However, the change in effective mean stress during the course of shearing was considered to be relatively small in both tests.

Swelling pressures evaluated during the triaxial test procedure are shown in Figure 2-17 together with previous results from section 2.3, cf. Figure 2-6. The axial swelling pressures measured during saturation are marked with squares and the swelling pressures evaluated as mean effective stress, before shearing and at failure, are used as error bars. The swelling pressures evaluated from the triaxial tests agree with the results from section 2.3.

2.4.5 Discussion

Based on the limited test series, the behaviour of the material from the field experiment was brittle, i.e. involving high stiffness, high deviator stress at failure, and low strain at failure. The deviator stress at failure is high also in comparison with previous studies on similar material and on more calcium dominated material shown in Figure 2-18. The deviator stress at failure is a measure of shear strength.

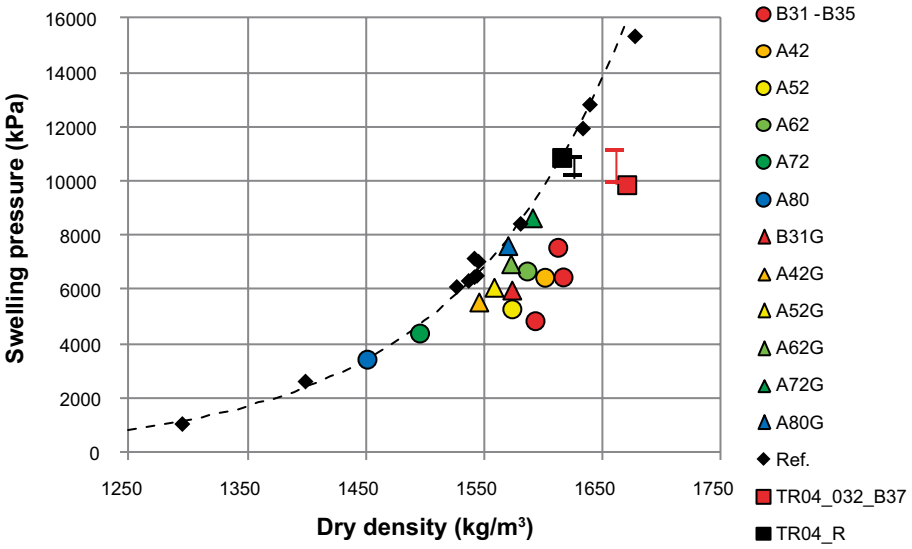

Figure 2-17. Swelling pressure evaluated from the triaxial tests procedure (squares and error bars) plotted with results from Figure 2-6.

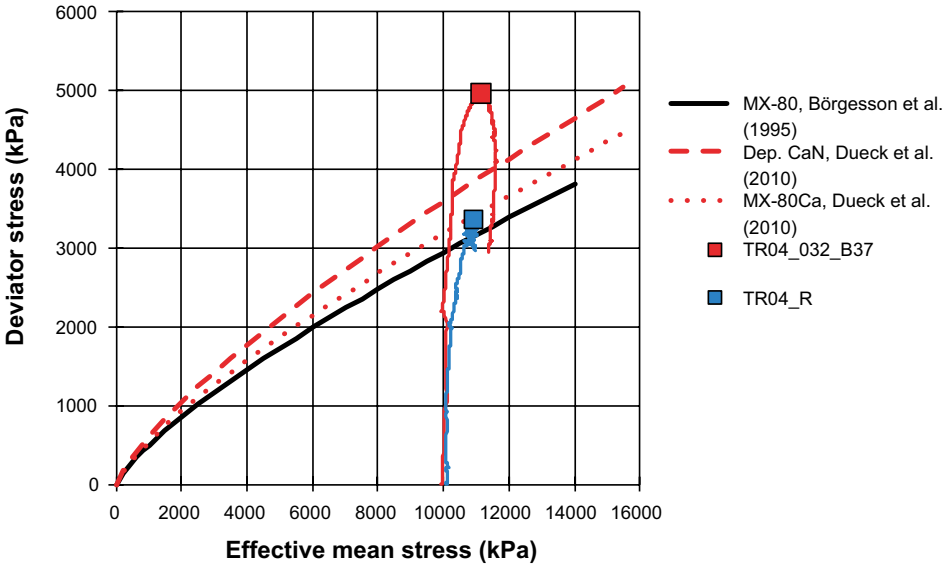

Figure 2-18. Results from the triaxial tests together with results from other studies.

2.5 Unconfined compression test

2.5.1 General

The unconfined compression test method has been used in several studies reported by Börgesson et al. (2003), Dueck et al. (2010), Karnland et al. (2009), and Dueck et al. (2011).

The unconfined compression test is an experimentally simple method where a specimen is compressed axially with a constant rate of strain with no radial confinement or external radial stress. The cylindrical specimen is compressed to shear failure. The shear strength is commonly determined on tall specimens with a height equal to double the size of the diameter to allow for the shear failure to develop without boundary effects from the end surfaces. The test method was here also used on short specimens with a height equal to the diameter, to study relative changes between different specimens.

2.5.2 Test equipment

Both short and tall specimens were tested and before the compression test the specimens were saturated in a special designed saturation device of steel. During the compression test the short specimens were placed in a mechanical press according to Figure 2-19 where a constant rate of strain was applied. The end surfaces were lubricated to minimize the end effects of the short specimens. The same mechanical press was used for the tall specimens, Figure 2-20. During both types of test the deformation and the applied force were measured by means of a load cell and a deformation transducer. All transducers were calibrated prior to the shearing of one series and checked afterwards.

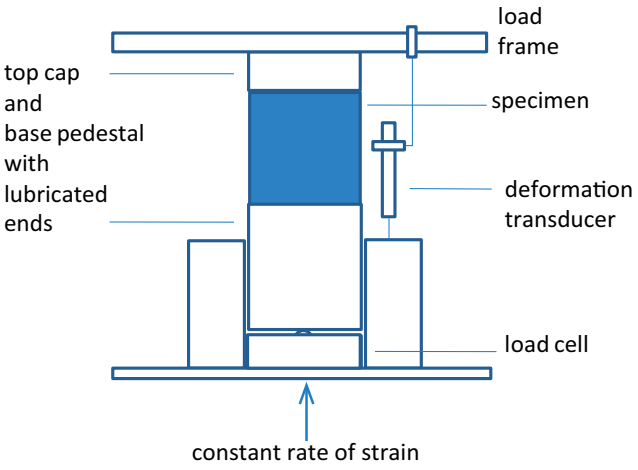

Figure 2-19. *Set-up for the unconfined compression test on short specimens.*

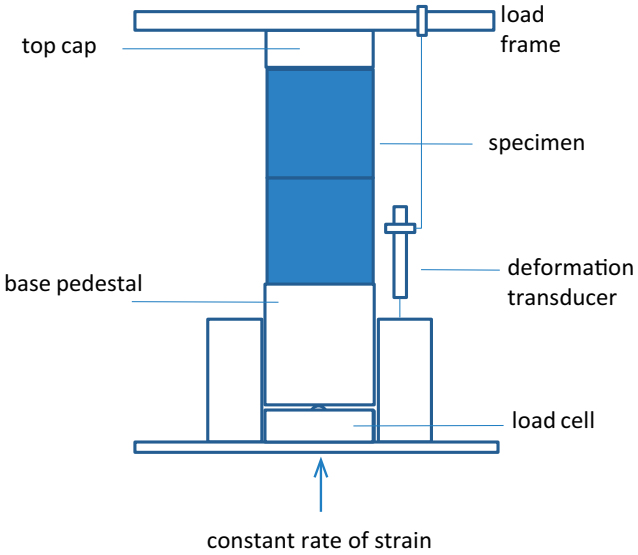

Figure 2-20. *Set-up for the unconfined compression test on tall specimens.*

2.5.3 Preparation of specimen and test procedure

Three main test series were run, two series with short specimens (UC2 and UCU2) having the height equal to the diameter aiming at relative changes between specimens and one series with tall specimens (UC4) having the height double the size of the diameter aiming at determination of shear strength. All specimens were saturated, except six short specimens compressed directly after sampling (UCU2).

Cylindrical specimens were prepared for all tests but different preparation techniques were used. The specimens were either prepared from material from the field experiment by drilling and trimming cylindrical specimens or prepared to cylindrical specimens in a compaction device from reference material saved from the block production. The tall reference specimens were compacted as two short specimens but put on top of each other in the saturation device before the saturation. The dimension of the test samples was minimized in order to get spatial resolution of the test parcel and to ensure full water saturation. The diameter was for all specimens 20 mm and the final height was 20 mm for the short and 40 mm for the tall specimens.

The saturation or re-saturation of the drilled and compacted specimens was done in a special designed saturation device where groundwater from the TBT test site, Table 1-4, was applied to the specimens after evacuation of air from the filters and tubes. The time used for the saturation of the short and the tall specimens were 2 weeks and 8 weeks, respectively. After saturation the specimens were removed from the saturation device at least 12 h before the shearing to homogenize while protected from evaporation. The specimens in the series not re-saturated were sheared within 20 minutes after sampling i.e. drilling.

An additional test series (UCH2) was run to study the influence of heating. Reference material was used for this series and the preparation was done as described above for the short saturated specimens. After the saturation the specimens, still inside the saturation device, were exposed to increased temperature of 120°C during 24 h. During heating 400 kPa in water pressure was applied.

At shearing the specimens were placed in the mechanical press and the compression started and continued at a constant strain rate of 0.8%/min which meant 0.16 mm/min for the short specimens and 0.32 mm/min for the tall specimens. During shearing the specimens were surrounded by a protective plastic sheet to minimize evaporation. After failure the water content and density were determined according to section 2.1.1.

The specimens were considered as undrained during shearing and no volume change was taken into account. The deviator stress q (kPa) and the strain ε (%) were derived from Equations (2-5) and (2-8), respectively. The results were corrected for initial problems with the contact surface in that decreasing the strain with the intercept on the x-axis, strain-axis, of the tangent to the stress-strain curve taken at a stress of 500 kPa.

2.5.4 Results

The results from the all test series are given in tabular form, Table 2-7 toTable 2-10, where maximum deviator stress and corresponding strain for each specimen are presented with the dry density, water content, void ratio, and degree of saturation. The deviator stress versus strain for all specimens in series UC2, UC4 and UCU2 is shown in Figure 2-21 to Figure 2-23 where the legends contain information about the position and dry density (kg/m^3). In Figure 2-23 the degree of saturation (%) is shown in brackets.

The results, plotted as maximum deviator stress q_{max} and corresponding strain ε versus dry density, are shown in Figure 2-24 and Figure 2-25. In the diagrams the colours refer to the positions of the specimens in the TBT field test. From the warmest to the coldest the colours red, orange, yellow, green, blue represent the intervals 30–40, 40–50, 50–60, 60–70, and 70–80 cm, respectively from the heater. In Figure 2-24 the results from the short specimens are shown and circles denote the re-saturated specimens, crosses the specimens sheared directly after drilling and the black points are the reference specimens. In Figure 2-25 the results from the tall re-saturated specimens are shown with the corresponding reference specimens.

The test series UCH2 with specimens exposed to heating in a laboratory oven at 120°C are presented as red diamonds with black marker lines in Figure 2-26, cf. Figure 2-24. The results show no increase in deviator stresses at failure but slightly reduced strains at failure compared to results from reference specimens.

Table 2-7. Results from the series with short saturated or re-saturated specimens (UC2).

Material	Preparation	Saturated with solution	Dimensions	Dry density ρ_d kg/m³	Water content w %	Void ratio e –	Degree of saturation S_r %	Maximum deviator stress q_{max} kPa	Strain at q_{max} ε %
TR04_032_B31	drilled	TBT grw	H = D	1,640	24.4	0.69	98	1,840	1.5
TR04_032_B31	drilled	TBT grw	H = D	1,620	24.8	0.71	97	2,030	2.0
TR04_032_B31	drilled	TBT grw	H = D	1,630	24.4	0.70	97	2,470	2.1
TR04_032_B35	drilled	TBT grw	H = D	1,630	24.6	0.71	97	2,490	3.1
TR04_032_A41	drilled	TBT grw	H = D	1,610	25.7	0.72	99	3,260	2.4
TR04_032_A41	drilled	TBT grw	H = D	1,600	26.1	0.73	99	3,350	3.7
TR04_032_A41	drilled	TBT grw	H = D	1,620	25.1	0.71	98	3,270	2.6
TR04_032_A41	drilled	TBT grw	H = D	1,610	25.4	0.73	97	3,760	3.2
TR04_032_A51	drilled	TBT grw	H = D	1,600	26.1	0.74	98	3,210	3.1
TR04_032_A61	drilled	TBT grw	H = D	1,580	27.0	0.76	99	2,250	2.2
TR04_032_A71	drilled	TBT grw	H = D	1,520	29.4	0.83	99	2,160	6.4
TR04_032_A80	drilled	TBT grw	H = D	1,460	33.0	0.91	101	1,590	7.0
TR04_032_B33	drilled	TBT grw	H = D	1,640	24.8	0.70	99	2,070	1.1
TR04_R R1	compacted	TBT grw	H = D	1,390	35.1	1.00	98	1,100	9.4
TR04_R R2	compacted	TBT grw	H = D	1,550	28.2	0.79	99	2,470	8.4
TR04_R R3	compacted	TBT grw	H = D	1,680	23.2	0.66	98	5,040	5.0

Table 2-8. Results from the series with tall saturated or re-saturated specimens (UC4).

Material	Preparation	Saturated with solution	Dimensions[1]	Dry density ρ_d kg/m³	Water content w %	Void ratio e –	Degree of saturation S_r %	Maximum deviator stress q_{max} kPa	Strain at q_{max} ε %
TR04_032_B31	drilled	TBT grw	H = 2D	1,630	25.3	0.70	100	3,130	1.5
TR04_032_A41	drilled	TBT grw	H = 2D	1,640	24.2	0.69	97	4,120	1.6
TR04_032_A51	drilled	TBT grw	H = 2D	1,630	24.9	0.71	98	4,000	2.0
TR04_032_A61	drilled	TBT grw	H = 2D	1,620	25.7	0.72	99	3,530	2.6
TR04_032_A71	drilled	TBT grw	H = 2D	1,550	28.9	0.80	101	2,350	4.6
TR04_032_A81	drilled	TBT grw	H = 2D	1,480	31.7	0.88	100	1,830	5.3
TR04_032_B33	drilled	TBT grw	H = 2D	1,660	24.1	0.68	99	3,520	1.5
TR04_R R1	compacted	TBT grw	H = 2D	1,400	35.3	0.98	100	1,090	6.7
TR04_R R2	compacted	TBT grw	H = 2D	1,560	28.0	0.78	100	2,390	5.5
TR04_R R3	compacted	TBT grw	H = 2D	1,690	22.4	0.64	97	5,910	3.6

[1]At saturation two specimens with H = D = 20 mm was put on top of each other.

Table 2-9. Results from the series with short specimens sheared directly after drilling (UCU2).

Material	Preparation	Saturated with solution	Dimensions	Dry density ρ_d kg/m³	Water content w %	Void ratio e –	Degree of saturation S_r %	Maximum deviator stress q_{max} kPa	Strain at q_{max} ε %
TR04_032_A31	drilled	–	H = D	1,710	21.0	0.63	93	5,870	1.7
TR04_032_A41	drilled	–	H = D	1,690	21.5	0.64	93	3,860	1.4
TR04_032_A51	drilled	–	H = D	1,680	22.2	0.66	94	5,300	1.9
TR04_032_A61	drilled	–	H = D	1,650	23.4	0.68	95	5,260	2.4
TR04_032_A71	drilled	–	H = D	1,560	27.5	0.78	99	2,570	4.9
TR04_032_A81	drilled	–	H = D	1,480	31.1	0.88	99	1,890	7.4

Table 2-10. Results from the series where influence of heating was studied (UCH2). All specimens were exposed to 120°C for 24 h.

Material	Preparation	Exposed to	Dimensions	Dry density	Water content	Void ratio	Degree of saturation	Maximum deviator stress	Strain at q_{max}
				ρ_d	w	e	S_r	q_{max}	ε
				kg/m³	%	–	%	kPa	%
TR04_R R1	compacted	120°C	H = D	1,560	28.0	0.79	99	2,850	7.7
TR04_R R2	compacted	120°C	H = D	1,560	27.9	0.78	99	3,050	6.9
TR04_R R3	compacted	120°C	H = D	1,540	28.9	0.81	99	2,640	7.7
TR04_R R4	compacted	120°C	H = D	1,560	28.5	0.79	101	2,900	6.8
TR04_R R5	compacted	120°C	H = D	1,570	27.5	0.77	99	3,180	6.6
TR04_R R6	compacted	120°C	H = D	1,570	27.7	0.77	100	3,170	5.9

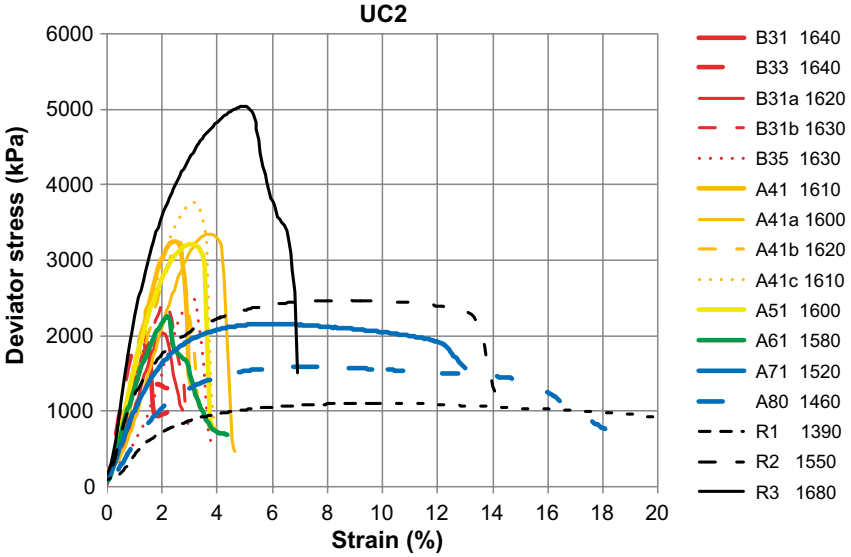

Figure 2-21. *Deviator stress versus strain from short specimens (UC2). The labels show the radial positions in the specific direction of block TR04_032 and the dry density (kg/m³). R1 to R3 denote reference material TR04_R.*

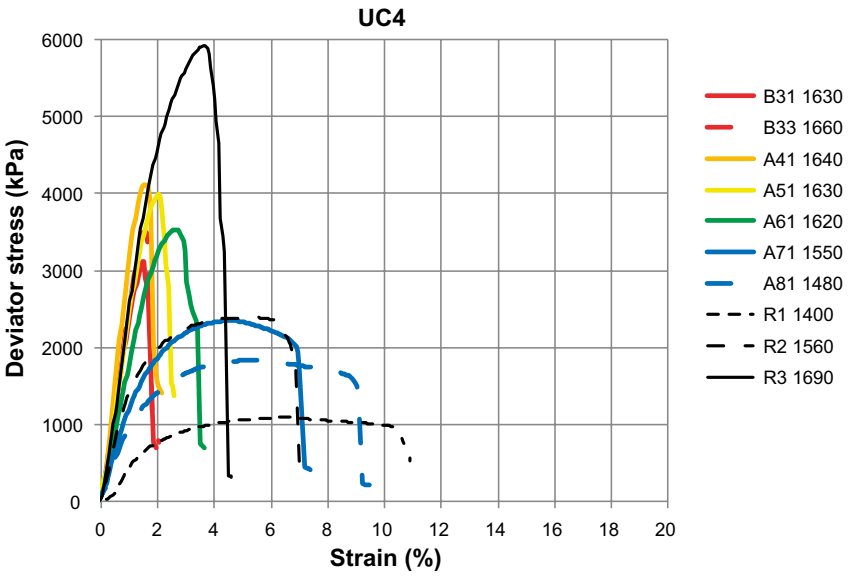

Figure 2-22. *Deviator stress versus strain from tall specimens (UC4). The labels show the position according to Figure 2-21 and the dry density (kg/m³).*

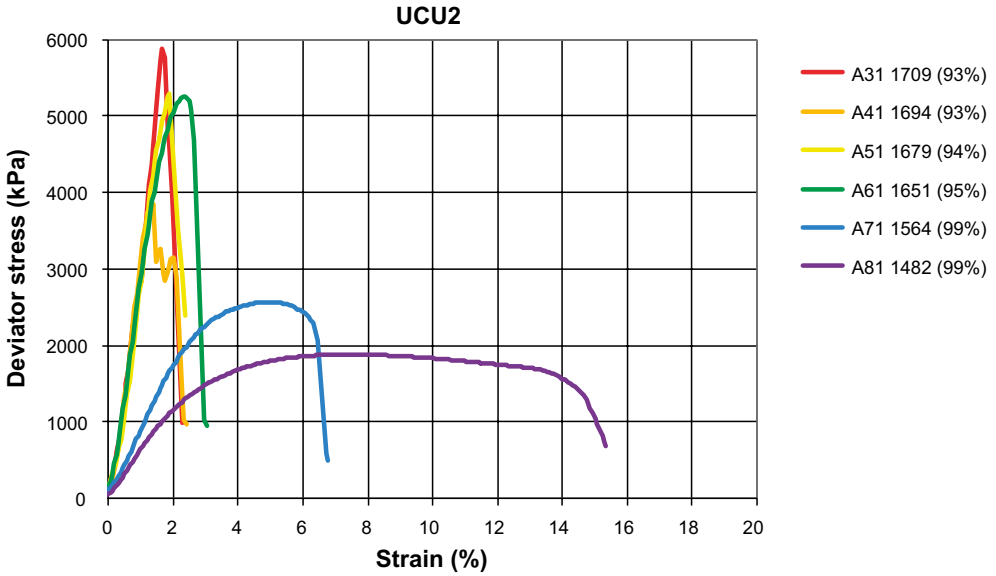

Figure 2-23. *Deviator stress versus strain for short specimens sheared directly after drilling (UCU2). The labels show the position according to Figure 2-21, the dry density (kg/m^3), and the degree of saturation (%) in brackets.*

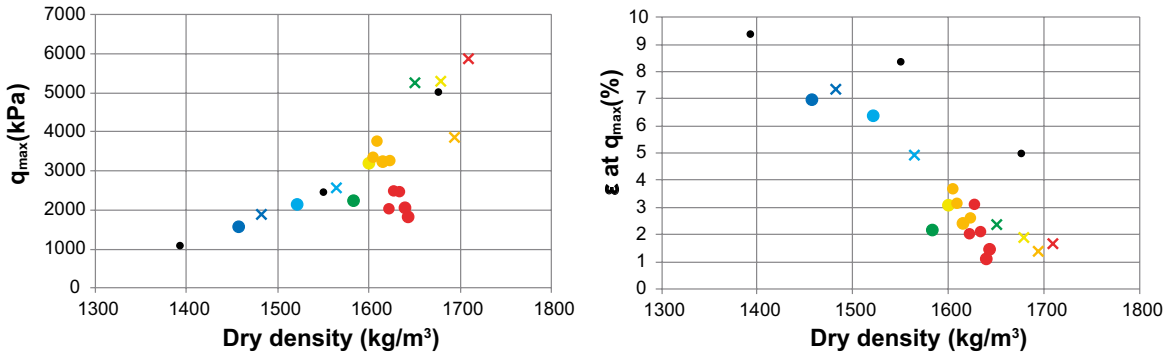

Figure 2-24. *Maximum deviator stress and strain versus dry density for test series with short saturated specimens (coloured circles) and specimens sheared directly after drilling (crosses). From the warmest to the coldest the colours red, orange, yellow, green, and blue are used. Black points denote references.*

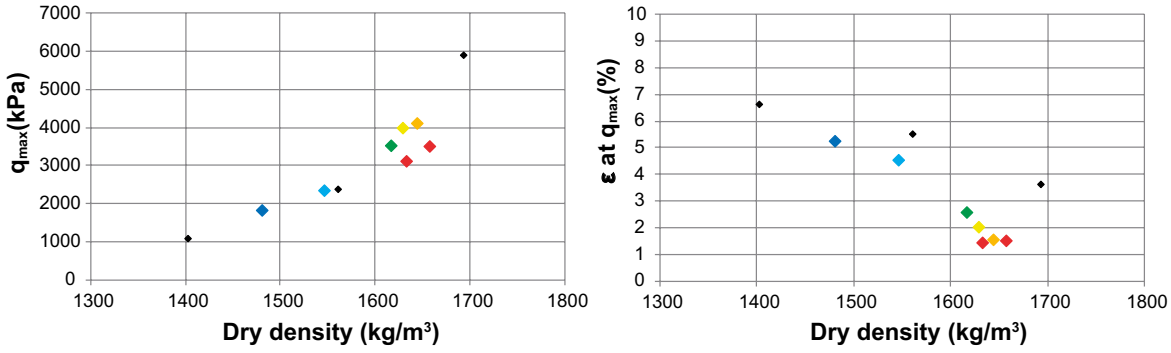

Figure 2-25. *Maximum deviator stress and strain versus dry density for test series with tall saturated specimens (coloured diamonds). From the warmest to the coldest the colours red, orange, yellow, green, and blue are used. Black points denote references.*

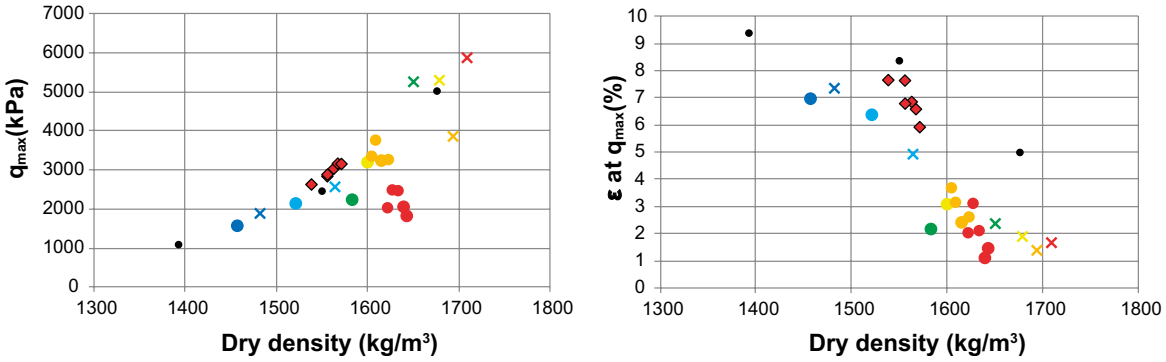

Figure 2-26. *Results from the series with specimens exposed to 120°C in a laboratory oven together with results from Figure 2-24.*

2.5.5 Discussion

Reduced strain at failure, less strain than the references was seen on all specimens from the field material.

Regarding the maximum deviator stress less values compared to the reference specimens were seen at the innermost position for the re-saturated short and tall specimens. Regarding the specimens sheared directly without re-saturation no deviation from the reference specimens were seen. More effort was given to find intact specimens to shear directly compared to the specimens being re-saturated. This might indicate that the better and more intact specimen the better agreement with the references, independent of re-saturation.

The LOT project (Karnland et al. 2009) provided an opportunity to make similar comparison of mechanical properties of buffer material exposed to field conditions relative to the initial properties of reference buffer material. One conclusion, based on the results from the unconfined compression tests on specimens from the warm section of the LOT project (90°C–120°C) was the significantly reduced strain at failure. This corresponds well with the results from the present study where reduced strain at failure was seen on specimens from all positions of the warm section which in the present project involved a temperature of 150°C. In addition, reduced strain at failure was also seen on the specimens exposed to short time laboratory heating at 120°C during 24 h in the present project.

In Figure 2-27 the maximum deviator stress from the triaixial tests are shown as a function of dry density together with the results from the unconfined compression tests shown in Figure 2-25. From Figure 2-27 it can be seen that results from the triaxial tests follow the trend shown by the unconfined compression tests on tall specimens. In section 2.4 where the triaxial test results were presented as the deviator stress versus mean effective stress, the behaviour was interpreted as brittle and deviating from references as well as from previous studies. However, the deviating behaviour can be considered as consistent with the low swelling pressure observed on specimens from approximately the same position, cf. section 2.3, if the interpretation of the deviator stress at failure as being relatively high instead is interpreted as a failure which occurred at a relatively low mean effective stress.

A comparison between the results from short and tall reference specimens gives that the only difference is the strain at failure. Thus, the influence of the end surfaces of the short specimens can be disregarded when considering deviator stress but not when considering the corresponding strain. However, the reduced strain at failure was seen on both types of specimens evaluated in comparison with their respective references.

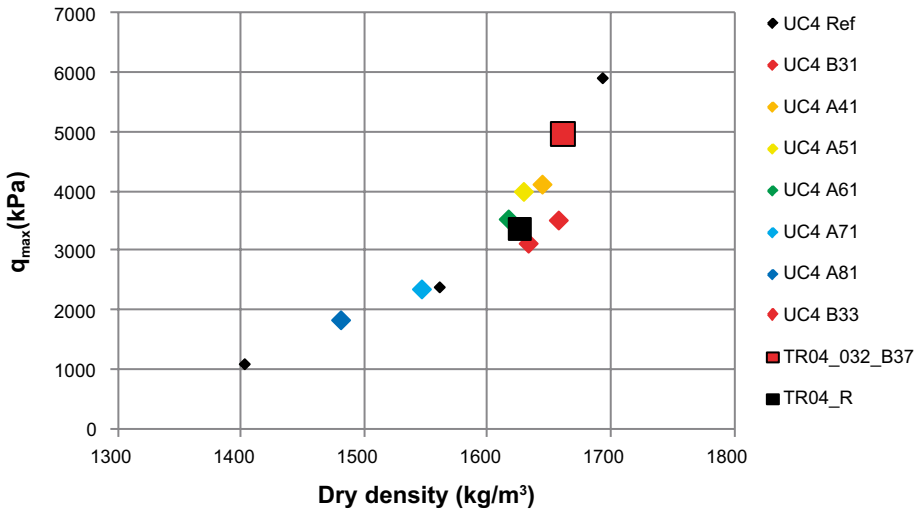

Figure 2-27. *Maximum deviator stress versus dry density for the test series with tall specimens from Figure 2-25 plotted with the results from the triaxial tests (squares).*

2.6 Summary and conclusions

Based on this investigation, where properties of material exposed to adverse conditions were compared to those of reference material, the following were found from the determination of retention curves;

- no large deviation was seen on the Na converted fine fraction of the material from the innermost positions,
- marked deviation was observed on the bulk material from the innermost position in equilibrium with $RH = 97\%$,

and the following were found from the determination of swelling pressure and hydraulic conductivity;

- a reduction in swelling pressure was observed on re-saturated specimens, especially on those from the innermost part,
- a scatter in hydraulic conductivity but a tendency towards an increase on re-saturated specimens drilled from the innermost part and a similar tendency was also observed on ground and re-compacted specimens and specimens prepared from dried material,

and the following from the triaxial tests;

- brittle behaviour involving high stiffness, high shear strength, and low strain at failure, was seen on the one specimen from the inner part,

and finally from the unconfined compression tests the following was observed;

- reduced strain at failure on all specimens from the field material,
- reduced maximum deviator stress on the re-saturated specimens from the innermost position.

The clearly observed reduced strain at failure was previously seen on results from the comparable field experiment in the LOT project (Karnland et al. 2009). In addition, the swelling pressure measured on material from the innermost position in the present project was found to be lower than expected. However, the innermost material was exposed to higher temperature in the present project than in the comparable LOT project. The lower swelling pressure is consistent with the behaviour seen in the results from the triaxial test on material from the innermost of the field experiment if the deviating failure behaviour is interpreted as a failure which occurred at a lower average stress than expected from the density.

3 Chemical and mineralogical analyses

3.1 Introduction

The design criteria for the KBS-3 repository stipulate that the temperature should never exceed 100°C at any position in the buffer. Compared with the expected KBS-3 conditions, the TBT field experiment represented adverse conditions with respect to temperature and temperature gradient, which are factors that will accelerate alteration processes in the bentonite buffer. According to the monitored temperature evolution (Figure 1-3) the entire volume of block R4 had been exposed to temperatures exceeding ~75°C and the innermost centimetres to temperatures up to ~155°C. From the test start in 2003 the bentonite buffer was wetted with the Na-Ca-Cl dominated groundwater from the granitic bedrock (composition in Table 1-1), which, however, was replaced by deionsed water after four years (details given in section 1.1).

The aim of the chemical/mineralogical characterization of the bentonite from block R4 was to elucidate how the 6 year-long hydrothermal experiment had affected the bentonite.

3.2 Materials and methods

3.2.1 Sampling and sample labels

Dismantling of the test package was completed in April 2010 and, awaiting analysis, the pieces of bentonite blocks were stored in evacuated and welded bags of aluminum laminate. Sampling of block R4 from the lower half of the buffer was made in July 2010. Six samples, A31–A81, were taken along the block radius in the top level (A) of the block (cf. Figure 1-7), each sample representing a radial width of approximately 2 cm. To increase the spatial resolution at the canister, the inner surface of the block was sampled separately by scraping off a 1–2 mm thick layer, which was labeled A30.

Sampling was made under normal laboratory conditions without any precautions to avoid oxidation of the samples. Separate samples for determination of the oxidation state of iron were, however, taken under anoxic conditions in a glove box (cf. Chapter 4).

The outer surface of the block was contaminated with sand added at the installation in the slot between the buffer and the borehole wall. This layer was removed and discarded prior to the sampling.

Individual samples were labeled with the block number, the vertical level in the block (A, B or C), the compass direction in the borehole and the radial position in cm from the center of the steel heater (cf. section 1.3). A suffix **b** or **c** indicates wether the sample consists of the bulk material or the fine clay fraction.

Uncompacted MX-80 bentonite stored since the manufacturing of the block was used as reference materials.

3.2.2 Sample preparation

Both the bulk samples and the Na-converted <0.5 μm fractions of the bentonite were analyzed for mineralogy, cation exchange capacity, and chemical composition (cf. Table 3-1). The bulk material was not subject to any pre-treatments prior to the analyses, apart from drying at 60°C and grinding.

In order to get as pure a smectite fraction as possible, thereby making element allocations in formula calculations less ambiguous, the <0.5 μm fraction, instead of the conventional <2 μm clay fraction, was chosen. Furthermore, the clay was saturated with one single, non-structural cation – in this case sodium – to make the allocation of cations to exchange and structural sites, respectively, less ambiguous. In order to facilitate separation of the <0.5 μm fraction, the bentonite was first suspended in deionised water and the clay was converted to homo-ionic Na-clay by addition of NaCl p.a. (final concentration 1M), followed by centrifugation and decantation of the clear supernatant.

Table 3-1. Analyses of bentonite samples from block R4 of the TBT test package.

		Bulk				Na-fines					
Sample Id	**WS**	**EA**	**EC**	**CEC**	**XRD***	**EA**	**CEC**	**XRD (oriented)**	**XRD (random)**	**CBD**	**GK**
TR04_032_A30	1	1	1	4	1	1	2	2	1	1	1
TR04_032_A31	1	1	1	4	1	1	2	2	1	1	2
TR04_032_A41	1	1	1	4	1	1	2		1	1	2
TR04_032_A51	1	1	1	4	1	1	2		1	1	2
TR04_032_A61	1	1	1	4	1	1	2		1	1	2
TR04_032_A71	1	1	1	2	1	1	2		1	1	2
TR04_032_A81	1	1	1	4	1	1	2		1	1	2
TR04_R	5	3	3	4	2	3	2	2	1	1	2

*XRD-analyses on bulk samples from which results are presented here were part of the *Secondary scan* (see section 1.2). Corresponding results from the *Primary scan* were fairly noisy and are therefore not included in this report. WS=water soluble salts; EA=element analysis incl C and S; EC=exchangeable cations; CEC=cation exchange capacity; XRD=X-ray diffraction (oriented and random); CBD=CBD-extractable iron, GK=Greene-Kelly test.

The procedure was repeated twice. Excess salt was thereafter removed by centrifuge-washings followed by dialysis (Spectrapore 3, 3500 MWCO dialysis membrane) against deionized water until the electrical conductivity of the external water remained <10 µS/cm for five days. After completed dialysis the slurry was dispersed in deionized water and centrifuged with a centrifugation time/speed calculated by use of Stokes´ Law to correspond to a particle separation at an equivalent diameter of 0.5 µm. After separation, the fine clay fraction was again treated with NaCl and dialyzed, and, finally, dried at 60°C and ground.

3.2.3 Aqueous leachates

Aqueous leaching of the bulk bentonite was used to obtain information about the composition of solutes and soluble salts in the bentonite. The dried (105°C) and ground bentonite was dispersed in deionised water (solid:liquid ratio 1:100) by ultrasonic treatment for 30 minutes and stirring overnight. The suspension was left for 5 days at room temperature to allow equilibration and sedimentation. After phase separation by centrifugation and stepwise ultra-filtration using filters of decreasing pore size (from 2 to 0.2 µm syringe filters Acrodisc PF), major anions, total C and N, and inorganic C were determined by use of ion chromatography and a C/N analyzer, respectively, at the Department of Ecology, Lund University.

3.2.4 Chemical analysis of bentonite and purified, homoionic Na-clay

The chemical composition of the bulk material and of the Na-converted <0.5 µm fraction of the bentonite was determined by ICP emission and mass spectroscopy at a certified laboratory (ACME Analytical Laboratories, Canada), using standard techniques for silicate analysis ($LiBO_2/Li_2B_4O$ fusion followed by nitric acid digestion). These analyses include major, minor and trace elements (incl. REE). Loss on ignition (LOI) was determined as the difference in weight of the dried (at 105°C) and the ignited sample (at 1,000°C).

Total carbon and sulfur were determined by evolved gas analysis (EGA) at the same laboratory by combustion of the samples in a Leco furnace, equipped with IR-detectors for CO_2 and SO_2. Carbonate carbon was determined as CO_2 evolved on treatment of a sub-sample with hot 15% HCl. All samples were ground, dried at 105°C and stored in desiccators prior to the chemical analysis, i.e. all analytical results are expressed in wt% (major oxides) or ppm (trace elements) of the dry mass of the sample.

3.2.5 Cation exchange capacity (CEC) and exchangeable cations

The cation exchange capacity (CEC) of bulk materials and of fine clay fractions (<0.5 µm) was determined by exchange with copper(II)triethylenetetramine following the procedure of Meier and Kahr (1999), modified according to Ammann et al. (2005) to ensure complete exchange.

The ground sample (~400 mg) was dispersed in 50 ml deionised water by ultrasonic treatment and shaking until complete dispersion. 20 ml of ~15 mM Cu(II)-triethylenetetramine solution was added to the suspension, which was left to react for 30 minutes on a vibrating table. After centrifugation, the absorbance at 620 nm of the supernatant was measured using a spectrophotometer (Shimadzu) and CEC calculated on the basis of the uptake of Cu by the clay. The water content of the clay was determined for a separate sample dried at 105°C for 24 h. All CEC determinations were at least duplicated.

The exchangeable cations of the bulk bentonite were determined by extraction into alcoholic ammonium chloride solution (0.15 M NH_4Cl in ~80% ethanol) according to a procedure originally recommended for CEC determinations of gypsiferous/calcareous soils (e.g. Belyayeva 1967, Jackson 1975). An alcoholic solution was used to minimize dissolution of gypsum and calcite, which are soluble in aqueous solutions. Ideally, i.e. when there is a minimum of easily soluble salts, such as chlorides and carbonates of alkali metals, the sum of extracted cations should be equivalent to the CEC of the sample.

0.8 g of the ground sample was shaken for 30 minutes in approximately one third of a total volume of 50 ml of the extractant. After centrifugation the supernatant was collected. This treatment was repeated three times. After evaporation of the alcohol and adjustment of the volume with deionised water, the concentration of Ca, Mg, Na and K was determined by use of an ICP-AES equipment at the Department of Ecology, Lund University. The water content of the bentonite was determined for a separate sample.

3.2.6 CEC of the fine clay fraction after Li-saturation and heating (Greene-Kelly test)

The CEC of the <0.5 μm fractions was determined also after Li-saturation and heating according to the so called Greene-Kelly test (Greene-Kelly 1953, 1955).

The experimental procedure follows Lim and Jackson (1986). The samples were washed three times with aqueous 3M LiCl and twice with 0,01M LiCl in 90% alcohol. The clay was allowed to dry at room temperature, and was thereafter heated at 250ºC overnight. CEC was determined by exchange with copper(II)triethylenetetramine following the procedure described in 3.2.5. Due to lack of material, only one CEC determination was made on sample A30, whereas determinations were duplicated for the rest of the samples.

3.2.7 X-ray diffraction analysis (XRD)

The mineralogical composition was determined by X-ray diffraction analysis of two different types of preparations, one type consisting of randomly oriented powders, the other type consisting of aggregates with maximised preferred orientation of the clay minerals.

Random powders of bulk samples are needed for a general characterization of the bentonite and for quantitative evaluations. These specimens were prepared after grinding the bulk material to a grain-size <10 μm. The powders were scanned in the 2θ interval 2–66° with a scanning speed of 1° 2θ/min.

Also the distinction between di- and trioctahedral types of clay minerals by measurements of d(060) requires an X-ray diffraction profile of a randomly oriented sample. The <0.5 μm fractions were therefore X-ray scanned as randomly oriented powders in the region 60–64° 2θ using a slow scanning speed (step size 0.02; count time 10 s) to increase resolution.

The <0.5 μm fraction of the samples from the innermost part of the block and of the reference were X-ray scanned also as oriented specimens, which give strongly enhanced basal (*00l*) reflections, and little or no evidence of the hk reflections of clay minerals. This type of preparation is used for clay mineral identification and is necessary for tests of the swelling properties and identification of interstratified structures. In order to give unambiguous diffraction characteristics, the samples were suspended in deionised water and saturated with magnesium by addition of $MgCl_2$ (0.5M). After removal of excess salt by centrifuge-washings, oriented aggregates were prepared of the clay slurry according to the “smear-on-glass” method” (Moore and Reynolds 1989) and dried at room temperature. The oriented mounts were X-ray scanned with a step size of 0.02° 2θ/scanning speed of 1° 2θ/min in the interval 2–36° 2θ. In order to test the swelling properties, the samples were re-scanned after solvation with ethylene glycol (EG) at 60°C for 48 hours.

A Seifert 3000 TT X-ray diffractometer with CuKα radiation and automatic divergence slit was used for the X-ray diffraction analyses.

Mineral identifications were made by comparison of the diffractograms of the randomly oriented powders with the Siroquant v.30h database, Sietronics Pty Ltd. The subsequent mineral quantification was made by use of the Siroquant Analytical Software. The modeling is principally based on a Rietveld refinement method of least squares fit of calculated to measured XRD profiles (Rietveld 1969). The method is described in general and also used for montmorillonite in Taylor and Matulis (1994). The precision in quantitative bentonite Siroquant analyses was assessed in Karnland et al. (2006).

3.2.8 Determination of "free iron oxides"

The chemical data and SEM-analyses of the bentonite from the heater contact clearly indicated that corrosion products of iron had been incorporated. Therefore, the content of free iron oxides in the <0.5 μm fractions was determined by the CBD-method (citrate-bicarbonate-dithionite) of Mehra and Jackson (1960) in order to improve the accuracy in formula calculations. Iron derived from iron oxides/oxyhydroxides can be extracted more or less selectively by this method, which employs sodium dithionite for the reduction of ferric iron, sodium bicarbonate as a buffer at neutral pH, and sodium citrate as a complexing agent for iron.

The procedure follows the recommendation of Jackson (1975). Na-citrate (0.3M) and $NaHCO_3$ (1M) were added at a ratio of 8:1 to the pre-weighed, dried sample in a centrifuge tube and the temperature of the suspension was brought to 75–80°C in a waterbath. Na-dithionite was added by means of a pre-calibrated spoon and the mixture was stirred for 5 minutes. The addition of dithionite was repeated twice, or until no reddish coloration of the clay was visible. After centrifugation the supernatant was collected in a volumetric flask. Fe, Si and Mg were determined by ICP-AES at the Department of Ecology, Lund University.

3.2.9 Transmission Electron Microscopy (TEM)

Analyses of isolated particles from the fine fractions (<0.5 μm) were made on reference and iron/bentonite interface material. Slides were prepared by dispersion of a minor amount of material in alcohol and the suspensions were thereafter placed on carbon Cu-grids. The main aim of the study was to detect possible morphological and/or chemical alteration in the montmorillonite as a result of the harsh test conditions. The analyses were performed by professor Reine Wallenberg at the Division of Polymer and Material Chemistry, Lund University, by use of a Jeol 3000F analytical high-resolution (scanning) transmission electron microscope. The microscope was equipped with a SDD X-ray detector and a Gatan imaging filter. Attainable point resolution is 0.17 nm in conventional TEM mode.

3.2.10 Scanning Electron Microsopy (SEM)

The iron heater surface and bulk material from defined positions close to the Fe/bentonite interface were examined by use of a HITACHI S-3400N scanning electron microscope equipped with an INKA X-sight detector from Oxford instruments. The bentonite was frozen and subsequently dried at low air pressure in order to reduce transport of dissolved species. The bentonite samples were broken to give a fresh surface, and thereafter again vacuum dried and carbon sputtered to give a cover of approximately 1 nm thick carbon film, in order to increase the electrical conductivity and thereby prevent charging of the samples by the electron beam. A secondary electron detector was used to study morphology. Spot, line and area analyses were performed at different distances from the iron/bentonite interface by use of an EDX detector, and a backscatter electron detector, in order to study element distribution.

3.3 Results

3.3.1 Aqueous leachates

The concentrations of anions, total organic carbon (TOC), inorganic carbon (IC) and total nitrogen (TN) extracted by dispersion of bentonite in deionised water are listed in Table 3-2. The distribution of chloride, sulfate and inorganic carbon are also plotted in Figure 1-1.

Table 3-2. Major anions, total organic carbon (TOC), inorganic carbon (IC) and total nitrogen (TN) in mg/g dry clay, extracted by dispersion of bentonite in deionised water in a solid:liquid ratio of 1:100. n.d.=not determined.

Sample Id	F mg/g	Cl mg/g	NO_3-N mg/g	SO_4-S mg/g	TOC mg/g	IC mg/g	TN mg/g
TR04 032 A30	0.006	0.55	0.010	1.44	0.430	0.34	0.096
TR04 032 A31	0.012	0.65	0.017	1.51	0.493	0.73	0.129
TR04 032 A41	0.014	0.51	0.015	1.40	0.493	0.96	0.129
TR04 032 A51	0.017	0.39	0.017	1.41	0.472	1.13	0.107
TR04 032 A61	0.025	0.96	0.036	1.72	1.250	1.26	0.366
TR04 032 A71	0.008	0.49	0.021	1.16	0.779	1.15	0.141
TR04 032 A81	0.025	1.00	0.029	0.73	1.113	1.27	0.271
TR04 Rb-1	0.008	0.16	0.038	1.27	0.605	1.64	0.115
TR04 Rb-2	0.018	0.20	0.031	1.27	0.725	1.47	0.173
TR04 Rb-3	0.008	0.19	0.035	1.26	0.522	1.21	0.138
TR04 Rb-4	0.006	0.16	0.027	1.27	n.d.	1.52	n.d.
TR04 Rb-5	0.007	0.16	0.051	1.28	n.d.	1.56	n.d.

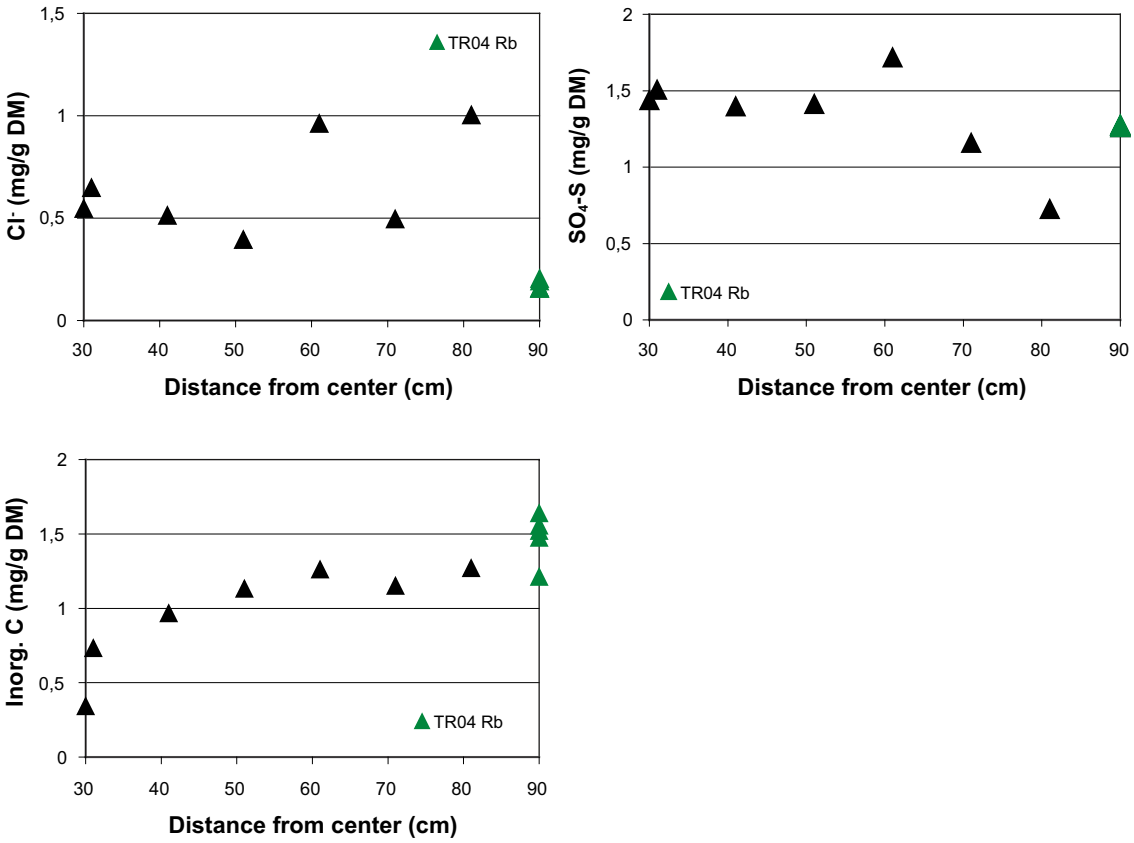

Figure 3-1. The radial distribution of Cl^-, SO_4^{2-} and inorganic C in water extracts of the bulk samples. The concentrations of five reference samples are plotted at position 90 cm.

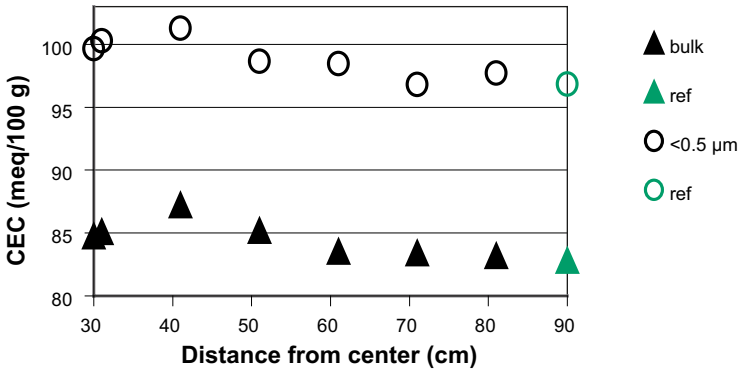

Figure 3-2. *Mean CEC values of the bulk samples and of the <0.5 µm fractions. Mean values for the references are plotted at the position 90 cm.*

The concentration of chloride has increased in the entire block but the distribution is irregular with peak values at 61 and 81 cm. This is probably a consequence of the artificial saturation with groundwater (cf. Table 1-1), and the subsequent use of deionized water for the saturation. The peripheral maximum is associated with a rather abrupt increase in the water content of the bentonite (cf. Figure 1-5).

The primary source of sulfate in the water extracts is the inventory of calcium sulfate in MX-80, whereas the contribution from the groundwater is minor (cf. Table 1-1). A loss in sulfate in the proximity of the hydration source and an increase in the inner part of block R4 suggest that calcium sulfate, which has temperature dependent solubility, has been re-distributed along the gradients in temperature and hydration that prevailed during the test period. XRD analyses show that the re-precipitated calcium sulfate phase is anhydrite ($CaSO_4$). Despite differences in experimental conditions, the results conform to those reported for the medium-scale LOT field test with MX-80 bentonite heated at 130°C (Karnland et al. 2009).

The inorganic carbon originates from carbonate minerals, which dissolved more or less completely during the leaching with water. Consequently, inorganic carbon is strongly correlated to the acid-soluble carbon content of the bentonite (cf. section 3.3.4) and both parameters display similar trend, which suggests that carbonates were dissolved in the warmest part of the block during the field test. Considering the temperature-dependant solubility of carbonates, this distribution pattern may be somewhat unexpected, but is indicated also in the FTIR-pattern of the samples investigated by B+Tech (Chapter 4). Karnland et al. (2009) reported analogous results for the medium-scale LOT field test.

3.3.2 Cation exchange capacity (CEC)

CEC of the bulk samples and of the <0.5 µm fractions are listed in Table 3-3 and plotted in Figure 3-2. The mean CEC of the bulk reference samples, 83 meq/100 g, matches the Cu-CEC values previously reported for the bentonite MX80 (e.g. Karnland et al. 2009, Dohrmann et al. 2012).

A tendency of increasing CEC towards the heater may be seen in both data sets but the changes relative the references are close to the resolution of the method. Furthermore, changes in CEC may result as a net effect of the various dissolution/precipitation reactions that have occurred in the proximity of the steel heater (cf. section 3.3.4).

Table 3-3. Cation exchange capacity (CEC) of bulk samples and of <0.5 µm fractions, determined by exchange against the Cu-trien complex.

Sample id	Bulk samples (meq/100 g)					Fractions <0.5 µm (meq/100 g)		
	CEC_1	CEC_2	CEC_3	CEC_4	CEC_{mean}	CEC_1	CEC_2	CEC_{mean}
TR04 032 A30	85.0	85.2	84.0	84.7	85	99.1	100.2	100
TR04 032 A31	85.4	84.5	84.7	85.6	85	100.6	100.0	100
TR04 032 A41	86.7	86.4	88.3	87.4	87	101.3	101.3	101
TR04 032 A51	84.6	83.8	86.4	85.9	85	99.0	98.3	99
TR04 032 A61	82.7	83.9	83.2	84.2	84	98.4	98.5	98
TR04 032 A71	83.5	83.3			83	97.0	96.6	97
TR04 032 A81	82.6	83.1	83.3	83.7	83	97.3	98.1	98
TR04 R	83.2	82.5	83.2	82.2	83	97.3	96.4	97

Table 3-4. Exchangeable cations of the bentonite of block R4. Cations extracted by exchange with NH_4^+ in alcoholic solution.

Sample id	Ca		K		Mg		Na		Sum
	meq/100 g	%	meq/100 g	%	meq/100 g	%	meq/100 g	%	meq/100 g
TR04 032 A30b	25.9	32	2.5	3.1	6.9	8	46.8	57	82
TR04 032 A31b	27.9	32	1.9	2.1	6.4	7	51.9	59	88
TR04 032 A41b	25.3	28	1.8	2.0	7.8	8	57.1	62	92
TR04 032 A51b	21.8	24	1.9	2.1	9.4	10	57.6	63	91
TR04 032 A61b	23.6	24	2.1	2.2	11.1	11	59.8	62	97
TR04 032 A71b	19.3	23	1.9	2.2	8.3	10	56.3	66	86
TR04 032 A81b	17.8	21	1.7	2.0	8.4	10	56.7	67	85
TR04 Rb-1	18.7	23	1.9	2.3	7.4	9	54.4	66	82
TR04 Rb-2	16.2	21	1.6	2.0	6.5	8	52.9	69	77
TR04 Rb-3	17.2	22	1.6	2.0	6.3	8	54.7	69	80

3.3.3 Exchangeable cations

The data on the exchangeable cations extracted by exchange with ammonium in alcoholic solution are compiled in Table 3-4 and plotted in Figure 3-3. The extractable Fe content in the iron-rich sample was very low (<2 mg/100 g dry clay), suggesting that iron existed mainly in a form that was not extractable into the NH_4 solution. Fe was therefore not included in the analyses.

Non-reactive solutes and easily soluble salts, such as chlorides and carbonates of alkali metals, will necessarily contribute to the extracted cation pool, which is an inherent problem in extraction methods for exchangeable cations. In general, the sum of cations exceeds the CEC by a few units, but sample A61 is exceptional in this respect, having a cation sum exceeding CEC by 13 meq/100 g. Thus, the contribution from soluble salts seems to be significant in this sample and most of the cations, but magnesium in particular, display a more or less pronounced maximum at this position in the block.

The relative proportion of the extracted cations in the reference samples is: 68% sodium, 22% calcium, 8% magnesium and 2% potassium. In the innermost part of block R4, the proportion of calcium has increased at the expense of sodium mainly (Figure 3-4), suggesting some exchange of sodium for calcium. Such exchange would be an expected effect of the dissolution of Ca-carbonate, which would affect the composition of the pore water and, accordingly, the exchangeable cation pool. Sodium is, however, the predominant cation in all samples also after the field test.

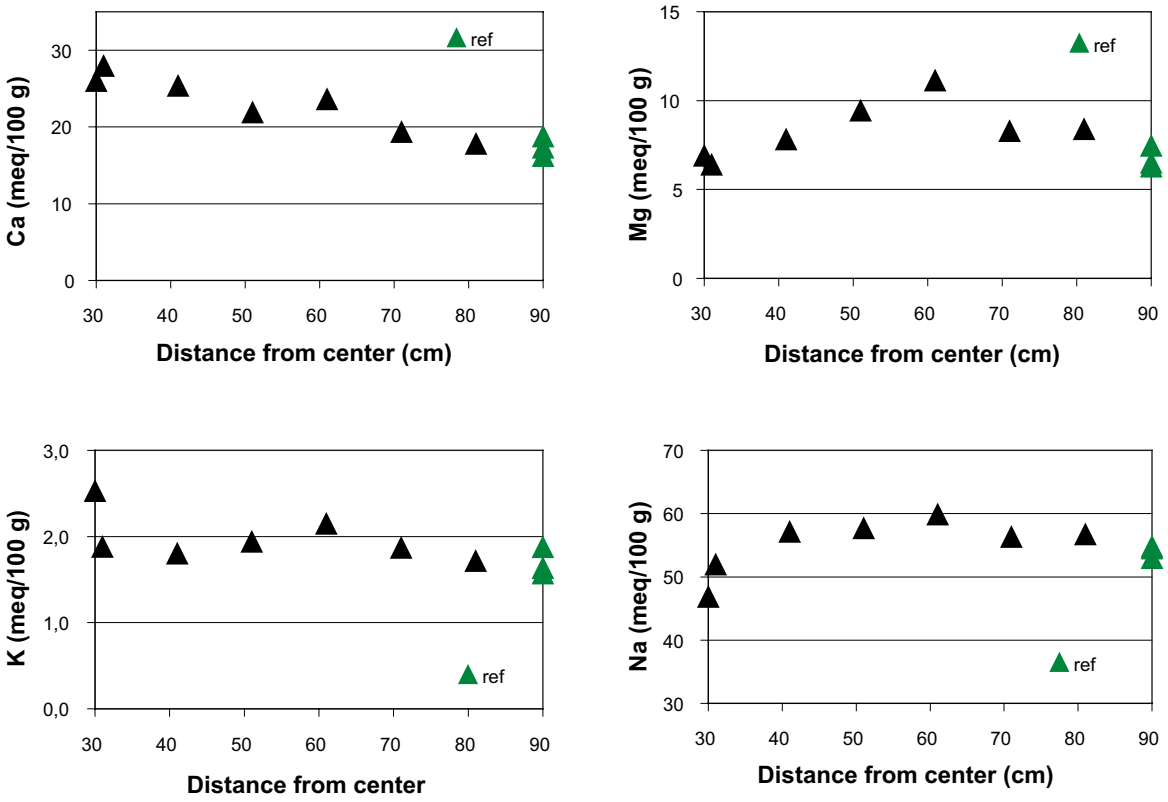

Figure 3-3. *Exchangeable Ca, Mg, K and Na plotted versus the distance from the center of the heater. Values of the reference samples are plotted at position 90.*

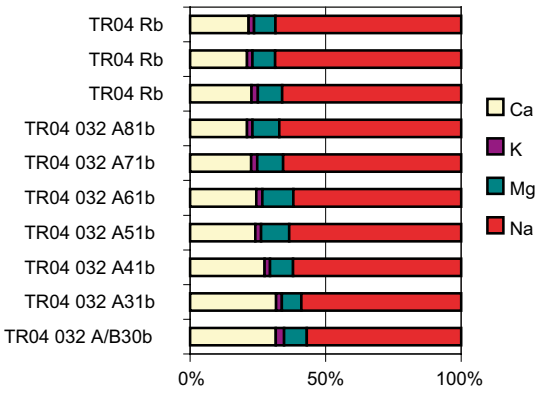

Figure 3-4. *Relative proportions of the cations extracted by exchange against NH_4 in alcoholic solution.*

3.3.4 Chemical composition of the bentonite

The chemical composition of the bulk bentonite samples is given in Table 3-5 and of the Na-converted <0.5 µm fraction in Table 3-6.

The carbonate and sulfate minerals are trace constituents (<1.5%) in MX80, but attention is paid to these minerals because of their temperature-dependent solubility. Dissolution-precipitation reactions under the non-isothermal conditions with steep temperature and hydration gradients that will prevail during the early operational phase of a repository may lead to redistribution of these minerals within the bentonite buffer.

The mean total carbon content of the reference bentonite is 0.283% (st. dev 0.015; N=3; DL=0.02), and the average content of acid-soluble carbon, which is derived mainly from carbonate, is 0.168 (st. dev 0.019). The remaining, acid-insoluble carbon fraction is most likely organic. Whereas the content of the latter carbon fraction varies insignificantly, the acid-soluble carbon displays a clear trend of decreasing values from the middle of the block towards the heater (Figure 3-5 upper left), which suggests that carbonates were dissolved in the warmest part during the field test. As should be expected, the acid soluble carbon content of the bentonite is strongly correlated (R^2=0.8) to the inorganic carbon content extracted by leaching the bentonite with water (cf. section 3.3.1).

The exact composition of the carbonate phase is not known but the calcium content remaining after allocating Ca to $CaSO_4$, and to the exchangeable cation pool, respectively, matches stoichiometrically the carbonate content fairly well, which suggests that Ca-carbonate is predominant (Figure 3-5 left bottom; cf. also Figure 1-1). No other carbonate phases have been detected.

The mean concentration of total sulfur in the reference samples is 0.287% (st. dev 0.015; N=3; DL=0.02%). According to the data on water-soluble salts (Table 3-2) approximately 45% of the total sulfur is derived from water-soluble sulfate minerals, mainly gypsum ($CaSO_4 \cdot 2H_2O$). The remaining fraction originates from sulfides and possibly also sulfates of low solubility (e.g. $BaSO_4$).

In the retrieved block R4 the distribution of total sulfur (Figure 3-5 right) is consistent with the results of the aqueous leaching, which indicates sulfate depletion in the peripheral part and accumulation in the middle part of the block.

Corrosion of the steel heater resulted in contamination of the inner block surface by iron, which has increased from 3.66% Fe_2O_3 (mean of three reference samples) to 7.49% Fe_2O_3 in sample A30 (Figure 3-6 left). The corrosion products occur as stains on the block surface, but it is clear that iron also has been incorporated into the bentonite matrix in sample A31 (cf. SEM analyses in section 3.3.8). All concentrations plotted in Figure 3-6 are expressed on an ignited basis to eliminate artifacts that may arise due to variable amounts of volatiles among the samples. Other heavy metals, such as Zn and Pb, which also have increased in the surface sample (Table 3-5 and Table 3-6), are probably associated with the corrosion products.

The excess iron of the innermost samples is insignificantly reduced by the fractionation used for purification of the smectite (Figure 3-6 left; Table 3-6), but most of the excess (90–95%) dissolves in a citrate-bicarbonate-dithionite solution (Table 3-7), which more or less selectively extracts “free” iron oxides (e.g. hematite, magnetite) and oxyhydroxides (e.g. goethite).

Also the magnesium distribution displays a gradient with a distinct maximum at the heater (Figure 3-6 right), where the MgO content of the bulk bentonite has increased from 2.49% to 4.47%. The outer part of the block is slightly depleted in magnesium, suggesting an inward transfer of magnesium along the thermal gradient.

All fine clay fractions of the block samples have gained some magnesium compared to the reference, although the increase in sample A30c is outstanding (Figure 3-6 right; Table 3-6). Less than 15% of the excess magnesium in sample A30c is extracted into the CBD-solution (Table 3-7), and this fact, together with the facts that the fine clay is Na-converted and carbonate-free (cf. Table 3-6), suggests that the major fraction of the magnesium excess exists in a non-exchangeable, insoluble form.

Again, the observations are analogous to those reported by Karnland et al. (2009) for the medium-scale LOT field test , but also small-scale laboratory experiments with MX-80 bentonite have demonstrated a migration of Mg as a consequence of steep thermal gradients (e.g. Jodin-Caumon et al. 2010)

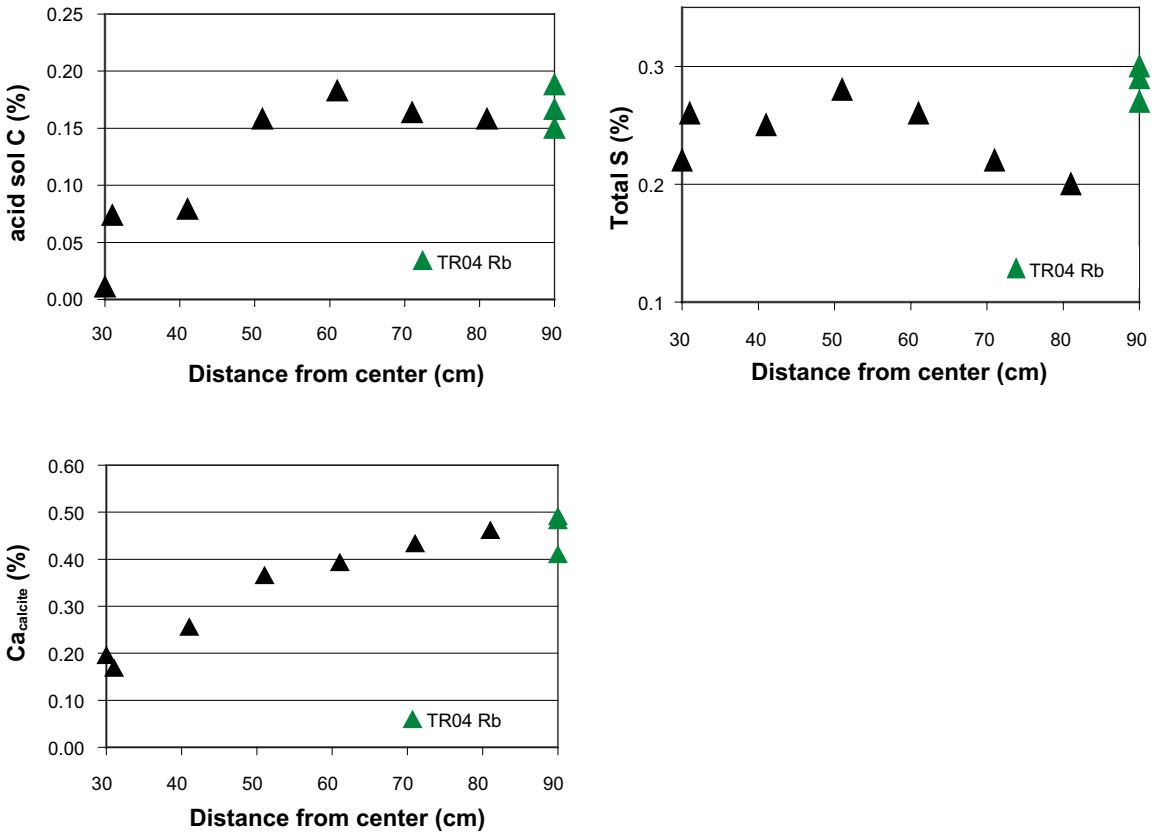

Figure 3-5. *The distribution of acid soluble carbon (upper left), Ca in calcite (lower left; see text for explanation) and total sulfur (upper right) in bulk samples. The reference samples are plotted at the position 90 cm.*

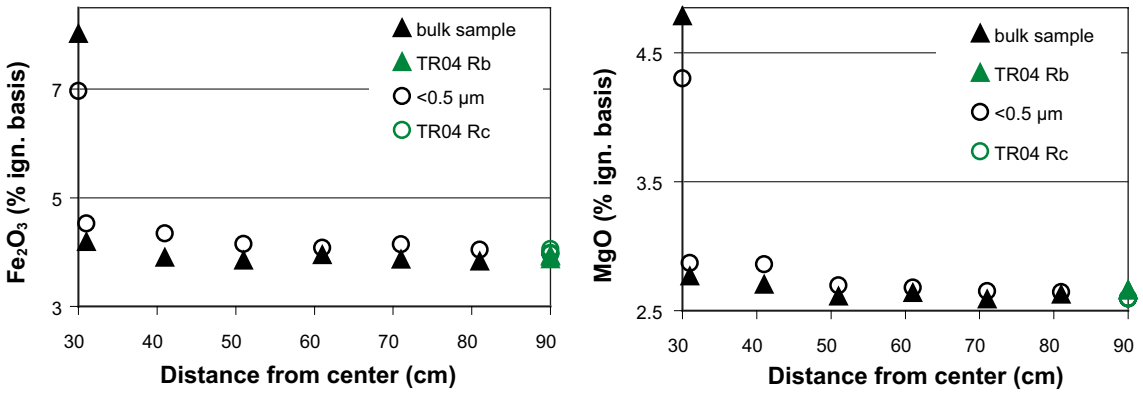

Figure 3-6. *The distribution of iron (left) and magnesium (right) in bulk samples and in Na-saturated fine clay fractions. Concentrations in weight % on an ignited basis. The reference samples are plotted at the position 90 cm.*

Table 3-5. Chemical composition of the bulk bentonite samples. Concentrations expressed on the dry weight (105°C) of the samples. DL=detection limit.

Sample id		SiO_2	Al_2O_3	Fe_2O_3	MgO	CaO	Na_2O	K_2O	TiO_2	P_2O_5	MnO	Cr_2O_3	LOI	Sum	TOT/C	TOT/S	acid sol C
		%	%	%	%	%	%	%	%	%	%	%	%	%	%	%	%
	DL	0.01	0.01	0.04	0.01	0.01	0.01	0.01	0.01	0.01	0.01	0.002	5.1	0.01	0.02	0.02	0.02
TR04 Rb-1		63.08	20.15	3.67	2.49	1.32	2.07	0.54	0.15	0.05	<0.01	<0.002	6.3	99.85	0.27	0.27	0.17
TR04 Rb-2		62.81	20.28	3.62	2.49	1.35	2.06	0.54	0.15	0.05	<0.01	<0.002	6.5	99.86	0.28	0.29	0.15
TR04 Rb-3		63.04	20.12	3.69	2.49	1.39	2.06	0.55	0.14	0.05	0.01	<0.002	6.3	99.85	0.3	0.3	0.19
TR04 032 A30b		58.67	18.8	7.49	4.47	1.25	1.78	0.53	0.14	0.05	0.02	<0.002	6.6	99.82	0.14	0.22	0.01
TR04 032 A31b		62.73	20.18	3.92	2.59	1.28	1.97	0.55	0.15	0.05	0.01	<0.002	6.4	99.86	0.22	0.26	0.07
TR04 032 A41b		63.30	19.90	3.65	2.53	1.31	2.06	0.55	0.15	0.05	<0.01	0.002	6.4	99.86	0.22	0.25	0.08
TR04 032 A51b		62.94	20.44	3.61	2.45	1.37	2.13	0.55	0.15	0.05	<0.01	<0.002	6.2	99.85	0.27	0.28	0.16
TR04 032 A61b		62.4	20.08	3.68	2.46	1.51	2.08	0.57	0.15	0.05	<0.01	<0.002	6.8	99.82	0.29	0.26	0.18
TR04 032 A71b		62.79	19.95	3.60	2.41	1.35	2.09	0.54	0.16	0.05	<0.01	0.002	6.9	99.85	0.28	0.22	0.16
TR04 032 A81b		63.26	20.15	3.59	2.46	1.27	2.15	0.52	0.15	0.05	0.01	<0.002	6.3	99.87	0.26	0.20	0.16

Table 3-5. Continued.

Sample id		Ba	Be	Co	Cs	Ga	Hf	Nb	Rb	Sc	Sn	Sr	Ta	Th	U	V	W	Zr
		ppm	ppm	ppm	ppm	ppm	ppm	ppm	Ppm	ppm	Ppm	Ppm	ppm	ppm	ppm	ppm	ppm	ppm
	DL	1	1	0.2	0.1	0.5	0.1	0.1	0.1	1	1	0.5	0.1	0.2	0.1	8	0.5	0.1
TR04 Rb-1		287	1	1.1	0.4	28.1	8.9	30.4	12.6	6	9	248.2	3.2	40.2	14.1	<8	<0.5	197.5
TR04 Rb-2		291	1	0.8	0.4	28.2	8.6	29.2	12.7	6	9	262.0	3.2	39.7	13.6	<8	<0.5	181.7
TR04 Rb-3		266	1	1.1	0.4	27.3	7.5	30.6	12.9	6	10	243.1	3.3	39.4	13.2	<8	<0.5	194.7
TR04 032 A30b		257	2	1.1	0.6	25.2	7.7	28.5	13.9	6	9	223.4	3.0	37.1	13.9	<8	<0.5	183.7
TR04 032 A31b		254	1	1.0	0.5	27.1	8.0	29.9	12.8	6	9	240.0	3.2	38.6	13.6	<8	<0.5	180.8
TR04 032 A41b		291	1	0.9	0.4	28.0	8.5	29.5	12.5	6	9	228.3	3.2	38.4	13.6	<8	<0.5	188.1
TR04 032 A51b		309	2	1.2	0.4	27.0	8.3	29.3	12.5	6	8	215.1	3.1	38.1	13.6	<8	<0.5	189.1
TR04 032 A61b		531	1	1.1	0.4	26.4	8.5	29.7	12.4	6	9	285.2	3.1	41.6	14.1	<8	<0.5	184.9
TR04 032 A71b		302	2	1.0	0.3	28.2	8.6	30.4	12.8	6	9	304.4	3.2	38.3	13.5	<8	<0.5	197.7
TR04 032 A81b		253	2	1.0	0.4	28.1	9.3	30.0	12.6	6	9	163.3	3.0	39.3	13.4	<8	<0.5	186.9

Table 3-5. Continued.

Sample id	Y	La	Ce	Pr	Nd	Sm	Eu	Gd	Tb	Dy	Ho	Er	Tm	Yb	Lu
	ppm	ppm	ppm	ppm	ppm	ppm	ppm	Ppm	ppm	Ppm	ppm	ppm	ppm	ppm	ppm
DL	0.1	0.1	0.1	0.02	0.3	0.05	0.02	0.05	0.01	0.05	0.02	0.03	0.01	0.05	0.01
TR04 Rb-1	42.2	53.5	115.5	13.22	50.8	10.32	0.65	9.09	1.48	8.32	1.61	4.31	0.62	4.01	0.56
TR04 Rb-2	40.0	51.2	112.7	13.02	49.6	10.15	0.66	8.96	1.46	8.3	1.54	4.09	0.57	4.03	0.52
TR04 Rb-3	43.2	52.7	114.1	13.20	50.4	10.20	0.68	9.21	1.47	8.52	1.53	4.21	0.63	4.02	0.53
TR04 032 A30b	39.7	48.9	105.0	12.20	49.4	9.14	0.61	8.41	1.42	8.26	1.49	4.18	0.57	3.97	0.52
TR04 032 A31b	41.3	52.6	113.0	13.09	50.1	10.02	0.66	9.19	1.46	8.52	1.54	4.28	0.61	4.07	0.54
TR04 032 A41b	40.8	52.3	112.5	12.92	50.2	9.91	0.61	8.82	1.45	8.14	1.51	4.30	0.60	4.01	0.55
TR04 032 A51b	40.1	50.5	110.8	12.43	47.3	9.66	0.62	8.58	1.42	8.28	1.46	4.15	0.59	3.98	0.53
TR04 032 A61b	40.8	50.6	110.9	12.68	47.8	9.83	0.65	8.80	1.45	8.15	1.52	4.21	0.59	3.93	0.54
TR04 032 A71b	41.5	52.4	111.7	13.05	51.4	10.12	0.67	8.75	1.47	8.24	1.52	4.29	0.61	4.04	0.55
TR04 032 A81b	41.1	52.2	115.9	13.23	51.0	10.31	0.62	9.35	1.49	8.32	1.52	4.13	0.61	3.85	0.53

Table 3-5. Continued.

Sample id	Mo	Cu	Pb	Zn	Ni	As	Cd	Sb	Bi	Ag	Au	Hg	Tl	Se
	ppm	ppm	ppm	ppm	ppm	ppm	ppm	Ppm	ppm	Ppm	ppm	ppm	ppm	ppm
DL	0.1	0.1	0.1	1	0.1	0.5	0.1	0.1	0.1	0.1	0.5	0.01	0.1	0.5
TR04 Rb-1	2.1	2.9	38.3	78	3.1	9.0	0.3	0.2	1	0.1	<0.5	<0.01	0.2	0.6
TR04 Rb-2	1.9	2.7	33.9	74	3.0	8.3	0.2	0.2	0.9	0.1	0.7	<0.01	0.2	<0.5
TR04 Rb-3	1.9	2.9	35.2	71	3.2	8.7	0.3	0.2	0.9	0.1	0.7	<0.01	0.2	0.7
TR04 032 A30b	2.6	6.1	44.8	111	3.7	11.2	0.4	0.2	0.9	0.1	1	<0.01	0.1	0.6
TR04 032 A31b	2.1	3.1	34.2	62	3.5	9.2	0.3	0.1	1	0.1	2.5	<0.01	0.1	<0.5
TR04 032 A41b	2.6	3.7	43.9	81	3.7	7.1	0.3	0.2	1	0.2	0.9	0.01	0.2	<0.5
TR04 032 A51b	2.7	3.6	45.8	86	3.6	8.8	0.3	0.3	1	0.2	<0.5	0.02	0.2	<0.5
TR04 032 A61b	2.4	4.9	44.6	76	3.9	8.9	0.3	0.3	1	0.2	<0.5	<0.01	0.2	<0.5
TR04 032 A71b	1.9	3.2	37.0	69	3.0	9.0	0.3	0.2	1	0.1	13.9	0.04	0.2	0.6
TR04 032 A81b	0.8	3.1	37.4	85	3.4	8.5	0.3	0.1	0.9	0.1	1.4	<0.01	0.2	0.6

Table 3-6. Chemical composition of the Na-saturated <0.5 µm fraction of the bentonite samples. Concentrations expressed on the dry weight (105°C) of the samples. DL=detection limit.

Sample id		SiO_2	Al_2O_3	Fe_2O_3	MgO	CaO	Na_2O	K_2O	TiO_2	P_2O_5	MnO	Cr_2O_3	LOI	Sum	TOT/C	TOT/S	acid sol C
		%	%	%	%	%	%	%	%	%	%	%	%	%	%	%	%
	DL	0.01	0.01	0.04	0.01	0.01	0.01	0.01	0.01	0.01	0.01	0.002	5.1	0.01	0.02	0.02	0.02
TR04 Rc-1		62.48	22.11	3.81	2.44	0.02	2.88	0.03	0.13	0.02	<0.01	<0.002	6.0	99.93	0.10	<0.02	0.02
TR04 Rc-2		62.63	22.16	3.75	2.44	0.02	2.84	0.03	0.13	0.02	<0.01	<0.002	5.9	99.93	0.10	<0.02	0.03
TR04 Rc-3		62.76	22.02	3.73	2.44	0.01	2.85	0.02	0.12	0.02	<0.01	<0.002	5.9	99.93	0.11	<0.02	0.02
TR04 032 A30c		59.52	20.77	6.54	4.04	0.04	2.77	0.02	0.11	0.03	<0.01	<0.002	6.1	99.9	0.13	<0.02	0.04
TR04 032 A31c		62.01	21.91	4.26	2.70	0.01	2.95	0.03	0.12	0.02	<0.01	<0.002	5.9	99.92	0.11	<0.02	0.03
TR04 032 A41c		61.97	22.11	4.09	2.69	0.03	2.91	0.02	0.12	0.02	<0.01	<0.002	5.9	99.91	0.09	<0.02	0.04
TR04 032 A51c		62.41	22.24	3.91	2.54	0.04	2.80	0.02	0.12	0.02	<0.01	<0.002	5.8	99.92	0.11	<0.02	0.03
TR04 032 A61c		62.40	22.22	3.84	2.52	0.01	2.86	0.02	0.13	0.02	<0.01	<0.002	5.9	99.92	0.14	<0.02	0.02
TR04 032 A71c		62.64	22.18	3.91	2.50	0.03	2.80	0.03	0.13	0.02	<0.01	<0.002	5.7	99.93	0.10	<0.02	0.02
TR04 032 A81c		62.43	21.88	3.79	2.48	0.02	2.91	0.03	0.13	0.02	<0.01	<0.002	6.2	99.93	0.11	<0.02	0.03

Table 3-6. Continued.

Sample id		Ba	Be	Co	Cs	Ga	Hf	Nb	Rb	Sc	Sn	Sr	Ta	Th	U	V	W	Zr
		ppm	ppm	ppm	ppm	ppm	ppm	ppm	ppm	ppm	Ppm	Ppm	ppm	ppm	ppm	ppm	ppm	ppm
	DL	1	1	0.2	0.1	0.5	0.1	0.1	0.1	1	1	0.5	0.1	0.2	0.1	8	0.5	0.1
TR04 Rc-1		7	2	0.8	<0.1	30.3	7.7	23.7	1.1	7	10	5.9	3.2	33.8	10.6	10	<0.5	145
TR04 Rc-2		8	2	0.7	1.2	31.5	8.1	24.0	1.2	7	10	5.9	3.5	33.9	10.8	<8	<0.5	150
TR04 Rc-3		6	2	0.7	<0.1	31.3	7.8	24.2	1.1	7	11	5.7	3.2	34.8	11.2	<8	<0.5	143
TR04 032 A30c		4	1	1.2	<0.1	29.2	7.5	20.0	0.7	6	10	4.8	3.1	34.0	10.4	11	<0.5	130
TR04 032 A31c		7	1	0.9	<0.1	31.9	8.4	22.1	1.0	7	11	5.9	3.2	33.5	10.8	12	<0.5	143
TR04 032 A41c		6	1	1.2	0.2	31.8	7.9	22.7	0.9	7	11	5.6	3.2	33.6	10.5	<8	<0.5	142
TR04 032 A51c		5	1	1.0	<0.1	31.9	7.7	23.7	1.1	7	11	5.6	3.2	33.8	10.5	<8	<0.5	145
TR04 032 A61c		7	1	1.0	0.3	32.3	9.9	22.4	1.1	7	10	5.0	3.1	31.1	9.4	8	<0.5	211
TR04 032 A71c		5	1	1.4	<0.1	31.2	7.6	23.1	1.0	7	11	5.7	3.1	32.3	10.0	<8	<0.5	148
TR04 032 A81c		7	2	0.9	<0.1	29.5	7.6	24.0	1.3	7	10	6.2	3.1	34	10.5	9	<0.5	147

Table 3-6. Continued.

Sample id	Y	La	Ce	Pr	Nd	Sm	Eu	Gd	Tb	Dy	Ho	Er	Tm	Yb	Lu
	ppm	ppm	ppm	ppm	ppm	ppm	ppm	ppm	Ppm	ppm	Ppm	Ppm	ppm	ppm	ppm
DL	0.1	0.1	0.1	0.02	0.3	0.05	0.02	0.05	0.01	0.05	0.02	0.03	0.01	0.05	0.01
TR04 Rc-1	23.9	41.5	90.6	10.33	38.4	7.46	0.4	6.26	1.02	5.24	0.96	2.42	0.33	1.99	0.26
TR04 Rc-2	25	44.1	96.3	10.55	39.3	7.79	0.39	6.73	1.05	5.44	0.94	2.4	0.35	2.14	0.26
TR04 Rc-3	24.3	41.1	90.5	10.26	37	7.41	0.39	6.56	1.04	5.33	0.94	2.39	0.33	2.07	0.26
TR04 032 A30c	22.4	40.5	87.0	10.15	37.6	7.30	0.39	6.24	0.99	5.05	0.87	2.26	0.3	1.81	0.24
TR04 032 A31c	25	43.4	95.0	10.57	41.3	7.74	0.42	6.63	1.07	5.22	0.99	2.53	0.36	2.06	0.28
TR04 032 A41c	23.9	44.0	95.1	10.46	39	7.66	0.4	6.71	1.03	5.19	0.91	2.33	0.33	2.01	0.25
TR04 032 A51c	23.4	41.6	91.1	10.3	37.2	7.24	0.39	6.28	0.98	5.16	0.92	2.31	0.32	1.89	0.25
TR04 032 A61c	22.8	42	90.7	9.84	36	7.19	0.38	6.24	0.96	5.00	0.89	2.30	0.32	1.95	0.24
TR04 032 A71c	23.2	41.9	92.9	10.17	38.3	7.59	0.38	6.34	0.98	5.38	0.92	2.31	0.32	1.91	0.24
TR04 032 A81c	24.3	42.0	91.5	10.48	38.5	7.35	0.4	6.52	1.03	5.38	0.96	2.38	0.32	1.98	0.27

Table 3-6. Continued.

Sample id	Mo	Cu	Pb	Zn	Ni	As	Cd	Sb	Bi	Ag	Au	Hg	Tl	Se
	Ppm	ppm	ppm	ppm	ppm	ppm	ppm	ppm	ppm	ppm	ppm	Ppm	ppm	ppm
DL	0.1	0.1	0.1	1	0.1	0.5	0.1	0.1	0.1	0.1	0.5	0.01	0.1	0.5
TR04 Rc-1	0.5	3.2	12.2	33	5.2	1.4	0.1	0.1	0.4	<0.1	6.3	0.02	<0.1	<0.5
TR04 Rc-2	0.2	2.8	11.0	30	1.7	1.3	<0.1	<0.1	0.4	<0.1	2.5	0.01	<0.1	<0.5
TR04 Rc-3	0.2	2.9	10.7	30	2.4	1.1	<0.1	<0.1	0.4	<0.1	0.7	<0.01	<0.1	<0.5
TR04 032 A30c	1.0	5.7	27.5	72	3.6	6.5	<0.1	0.2	0.3	<0.1	2.9	<0.01	<0.1	<0.5
TR04 032 A31c	0.5	2.2	20.3	30	2.7	3.5	<0.1	0.1	0.6	<0.1	3.1	<0.01	<0.1	<0.5
TR04 032 A41c	0.5	3.9	18.1	49	3.6	1.9	<0.1	0.3	0.4	<0.1	1.2	0.01	<0.1	<0.5
TR04 032 A51c	0.4	6.2	17.0	44	3.5	2.2	<0.1	0.3	0.4	<0.1	1.4	<0.01	<0.1	<0.5
TR04 032 A61c	0.4	5.9	13.5	29	3.0	2.3	<0.1	0.3	0.4	<0.1	1.9	<0.01	<0.1	<0.5
TR04 032 A71c	0.4	10.5	12.9	29	3.2	2.3	<0.1	0.3	0.4	<0.1	1.4	0.02	<0.1	<0.5
TR04 032 A81c	0.2	5.9	17.8	31	3.1	2.5	<0.1	0.4	0.5	<0.1	2.2	<0.01	<0.1	<0.5

3.3.5 Smectite composition

The chemical composition of the Na-converted <0.5 µm fractions (Table 3-6) has been used for calculations of the average structural formula of the smectite. The calculation is based on the structures of 2:1 layer silicate, assuming an anionic charge of –44 (Newman and Brown 1987), in addition to the following assumptions and simplifications:

The **iron** content was corrected for CBD-extractable iron (Table 3-7), since this extraction clearly indicated that the major fraction of the excess iron in the samples proximal to the heater was not fixed in the structure of the smectite but present as an "impurity".

The remaining iron was allocated to the octahedral sheet of the smectite and assumed to be trivalent. The Mössbauer data (Chapter 4) provide some support to this assumption, although the oxidation state of iron in the purified <0.5 µm fractions was not determined. If also ferrous iron exists in the structure, the octahedral charge will be underestimated .

Potassium (0.02–0.03% K_2O) in the Na-converted clay was considered non-exchangeable and was allocated to illite, the amount of which is too small (<0.5%) for detection by use of XRD analysis. The proportion was calculated assuming the potassium content of illite to be 8.5%, which is intermediate between the extreme values reported for clay-sized illite (Newman and Brown 1987); the SiO_2 and Al_2O_3 contents were adjusted accordingly.

Any **calcium** that may exist after the dialysis of the Na-converted clay (0.01–0.04% CaO) was assigned to the pool of interlayer cations.

Magnesium, corrected for the CBD-extractable fraction (Table 3-7), was assigned to the octahedral sheet because the fine clay had been saturated with sodium and dialyzed prior to the chemical analysis. The interlayer charge would be underestimated if some of the magnesium found by chemical analysis of the fine clay is exchangeable.

Silica was corrected for the small amounts extracted by the CBD-treatment (Table 3-7) and the rest was allocated to the tetrahedral sheet of the smectite. A "contamination" of the smectite with free silica would decrease the calculated tetrahedral charge.

The calculated average structural formulae of the smectite of block and reference samples are given in Table 3-8. The structural formulae of the reference samples are almost identical ($(Al_{3.16}Mg_{0.45}Fe^{3+}_{0.34})(Si_{7.87}Al_{0.13})O_{20}(OH)_4X_{0.70}$ where X is a monovalent interlayer cation) and typical of montmorillonite, in which the charge arises mainly from divalent cations in octahedral sites.

The smectite structure of most of the block samples deviates insignificantly from that of the reference samples, sample A30c being the most conspicuous exception. The formula of the latter sample suggests a major redistribution of the charge between the tetrahedral and octahedral sheets, as an effect of a significant substitution of octahedral Al by Mg, and a corresponding substitution of tetrahedral Si by Al.

Table 3-7. The CBD-extractable iron, magnesium and silica contents (as oxides in weight% of the dry matter) of the Na-saturated <0.5 µm fractions. The total concentrations are also given together with the CBD-extractable fractions.

	CBD-extractable (%)			Total (%)			CBD-extractable fraction		
Sample id	Fe_2O_3	MgO	SiO_2	Fe_2O_3	MgO	SiO_2	Fe_2O_3	MgO	SiO_2
TR04 032 A30c	2.43	0.24	0.77	6.54	4.04	59.52	0.37	0.059	0.013
TR04 032 A31c	0.48	0.08	0.39	4.26	2.7	62.01	0.11	0.030	0.006
TR04 032 A41c	0.26	0.10	0.32	4.09	2.69	61.97	0.06	0.036	0.005
TR04 032 A51c	0.29	0.08	0.31	3.91	2.54	62.41	0.07	0.030	0.005
TR04 032 A61c	0.26	0.06	0.32	3.84	2.52	62.4	0.07	0.024	0.005
TR04 032 A71c	0.25	0.05	0.26	3.91	2.5	62.64	0.06	0.020	0.004
TR04 032 A81c	0.24	0.06	0.26	3.79	2.48	62.43	0.06	0.024	0.004
TR04 Rc	0.17	0.03	0.13	3.76	2.44	62.76	0.05	0.014	0.002

Table 3-8. Calculated mean structural formula of the purified smectite fraction. The calculations are based on the chemical composition of the Na-saturated <0.5 µm fraction (Table 3-6) corrected for CBD-extractable elements (Table 3-7). The result for sample A30c (in red) is discussed in the text.

	TR04 032 with correction for CBD-extractable Fe, Si, Mg									
	Rc-1	Rc-2	Rc-3	A30c	A31c	A41c	A51c	A61c	A71c	A81c
Si	7.86	7.87	7.88	7.72	7.83	7.81	7.84	7.84	7.86	7.87
Al	0.14	0.13	0.12	0.28	0.17	0.19	0.16	0.16	0.14	0.13
Σ tet	8.00	8.00	8.00	8.00	8.00	8.00	8.00	8.00	8.00	8.00
Al okt	3.15	3.16	3.15	2.94	3.11	3.12	3.15	3.15	3.15	3.14
Ti	0.01	0.01	0.01	0.01	0.01	0.01	0.01	0.01	0.01	0.01
Fe^{3+}	0.34	0.34	0.34	0.41	0.36	0.36	0.34	0.34	0.35	0.34
Mg	0.45	0.45	0.45	0.74	0.50	0.49	0.46	0.46	0.46	0.46
Σ oct	3.96	3.96	3.95	4.10	3.98	3.98	3.97	3.97	3.97	3.95
Ca	0.003	0.003	0.003	0.006	0.001	0.004	0.005	0.001	0.004	0.003
Na	0.71	0.70	0.70	0.71	0.73	0.72	0.69	0.70	0.69	0.72
Interlayer charge	0.71	0.70	0.70	0.72	0.73	0.72	0.70	0.70	0.70	0.72
% tet. Charge	20	19	17	39	24	26	23	22	21	17
Molar weight	745	744	744	749	746	746	745	745	744	744
CEC calc.	96	94	94	96	98	97	94	95	94	96

To validate the results of the formula calculation, the CEC of the <0.5 µm fractions was determined after the clay had been saturated with Li and heated overnight at 250°C (Greene-Kelly test). Upon heating, small cations like Li are believed to migrate from the interlayer positions into the vacant octahedral sites, thereby eliminating the octahedral charge (the Hofmann-Klemen effect; Hofmann and Klemen 1950, Brindley and Brown 1980). The test is used for distinguishing between montmorillonite (octahedral charge >>tetrahedral charge) and beidellite (octahedral charge < tetrahedral charge), on the basis of the significant loss in cation exchange capacity and expandability exhibited by Li-montmorillonite but not by Li-beidellite. Accordingly, the remnant CEC of the samples after Li-saturation and heating should represent the tetrahedral charge of the smectite.

As shown in Table 3-9, the CEC of the heated Li-clays is more or less constant. Consequently, the charge distribution, determined by CEC measurements before and after Greene-Kelly treatment, and by formula calculations based on chemical composition, respectively, (Figure 3-7) displays a clear discrepancy for the magnesium-rich sample A30c. The cause of this discrepancy is not known, but it is notable that the total octahedral site occupancy in the formula of sample A30c is in clear excess of the normal value of 4 per $O_{20}(OH)_4$ in dioctahedral smectites. Anomalous structural formulae may arise if, for instance, amorphous or surface-sorbed impurities are present in the clay fraction or if interlayers are present in the smectite structure. It therefore remains to establish whether the allocation of all non-exchangeable magnesium to octahedral sites in smectite has a true structural foundation, or whether the sink of magnesium is a neoformed phase.

Table 3-9. CEC of the Na-saturated <0.5 µm fractions after Li-saturation and heating (Greene-Kelly test).

Sample id	CEC_1 meq/100 g	CEC_2	CEC_{mean}
R4 032 A30c	20	n.d.	20
R4 032 A31c	21	21	21
R4 032 A41c	18	17	18
R4 032 A51c	19	18	18
R4 032 A61c	23	22	22
R4 032 A71c	18	19	19
R4 032 A81c	19	18	19
R4 Rc	20	19	20

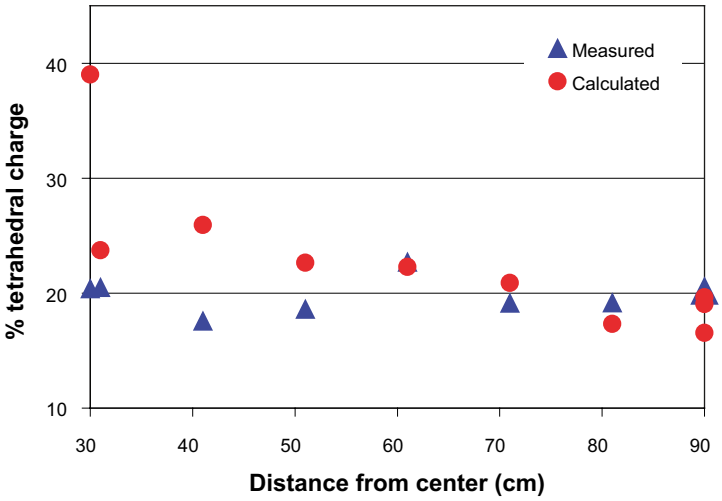

Figure 3-7. Tetrahedral charge in percentage of total charge, determined by 1. measurements of CEC before and after Greene-Kelly treatment, and 2. by calculation of the structural formulae. The reference samples for both data sets are plotted at the distance 90 cm.

3.3.6 Mineralogical composition

The diffraction pattern of random powders of the bulk samples are presented in Figure 3-8, where the strongest peaks of the major non-phyllosilicates gypsum, quartz, cristobalite, plagioclase, anhydrite and calcite are indicated together with the (001) and (003) basal reflections and the hk reflections of montmorillonite.

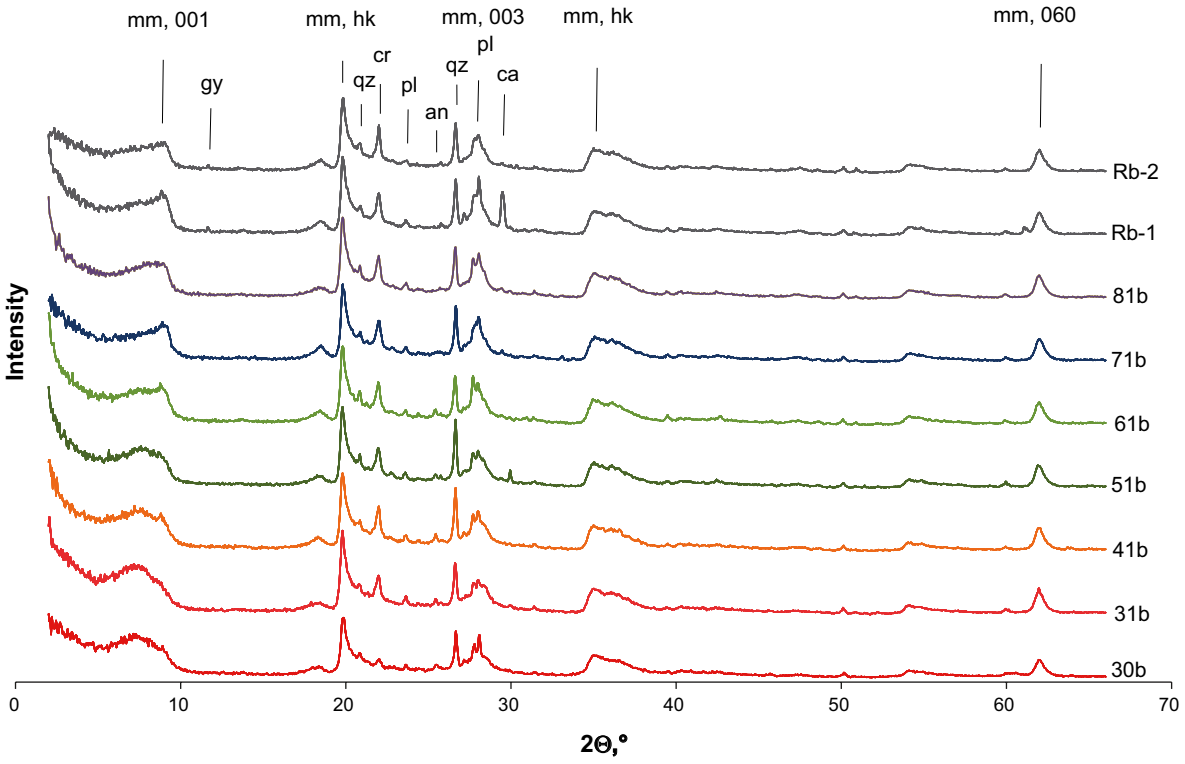

Figure 3-8. XRD profiles of all analysed bulk samples. Sample positions and references are indicated to the right. an=anhydrite; ca=calcite; cr=cristobalite; gy=gypsum; pl=plagioclase; qz=quartz; mm=montmorillonite. Random powders. CuKα radiation.

Traces of gypsum are generally found in MX80 but according to the chemical data, the maximum amount of gypsum that can exist (i.e. if all sulfur is allocated to $CaSO_4 \cdot 2H_2O$) in the reference bentonite is about 1.5%, which is close to the detection limit of the XRD method. The strongest peak of gypsum is indicated in the profile of the reference samples but cannot be detected in any of the profiles of the block samples. Instead, a peak of low intensity produced by anhydrite ($CaSO_4$) is detectable in the block samples from 61 cm and inwards. Accordingly, the mineralogical data match the chemical data, which suggest that sulfate was dissolved in the peripheral parts of the buffer where water was supplied, and accumulated in the inner, warmer parts of the block.

Also calcite is generally found in MX80, and is indicated in the chemical data but, again, the quantity (~1.0% if all acid-soluble carbon is allocated to $CaCO_3$) is close to the detection limit. The appearance of a fairly strong calcite reflection at 29.5°2θ in one of the reference samples is therefore believed to be caused by an inhomogeneity in particle size and/or by poor random mixing of the powder. A weak peak at the position of the strongest calcite peak is indicated also in the peripheral samples A71 and A81, which would be consistent with the chemical data, but the identification by XRD analysis must be considered uncertain at these low quantities.

The block samples display no significant changes in the peak intensities of quartz compared with the reference, whereas some random variation in the intensity of the feldspar peaks may be seen among the samples. However, both the excellent {010} and {001} cleavage of feldspars, which promotes preferred orientation, and the coarse grain size of feldspars, may give a variation in the peak intensities.

In contrast, a decrease of the intensity of the strongest peak of cristobalite in sample A30 at the heater is believed to be caused by dissolution. This interpretation is supported by the by results of parallel investigations by B+Tech in which evaluations were based on Fourier transform infrared spectroscopy (Chapter 4).

Despite the incorporation of a fairly high amount of CBD-extractable Fe_2O_3 in sample A30, neither iron oxides (e.g. hematite, magnetite) nor iron oxyhydroxides (e.g. goethite) can be detected in the XRD-profile of the sample, possibly because the neoformed iron phase(s) is/are poorly crystallized or X-ray amorphous.

The shape and width of the (001) basal reflection of montmorillonite vary somewhat among the samples but is generally broad and centred around 10 Å. This appearance of the peak arises because the samples were x-ray scanned in a more or less dehydrated, collapsed state. An asymmetry towards the low angle side in some of the samples suggests that the re-hydration of the smectite resulted in mixed hydration states.

The XRD patterns of the random powders were used for quantitative evaluations by use of the Siroquant software, in which the montmorillonite (02,11) and (13,20) reflections indicated as (mm, hk) in Figure 3-8 were used to evaluate the montmorillonite content. The results of the quantitative evaluations of the main identified mineral phases are presented in Table 3-10.

Table 3-10. Distribution of the main minerals in the bentonite at seven radial positions and two reference samples (Rb-1 and Rb-2). All results in weight percentages. The abbreviation m.e.o.f. indicates "mean error of fit" in the Siroquant modelling.

Mineral phase	30b	31b	41b	51b	61b	71b	81b	Rb-1	Rb-2	m.e.o.f.
Montmorillonite	90.1	89.3	87.1	86.8	87.1	87.9	87.1	87	87.1	0.63
Plagioclase	3.5	2.6	3.2	3.5	4.2	2.8	4.5	3.3	2.7	0.46
Anhydrite	0.5	0.4	0.7	0.4	0.4	0.1	0	0	0	0.20
Calcite	0	0	0	0.2	0.4	0.5	0.4	1.3	0.4	0.23
Cristobalite	0.4	2	2.3	2.2	2.1	2.1	2.1	2.2	2.8	0.14
Gypsum	0	0.2	0.5	0.5	0.7	0.9	0.7	1	1.3	0.30
Quartz	4.6	4.4	5.3	5.8	4.6	4.9	4.5	4.7	5	0.20
Sum	99.1	98.9	99.1	99.4	99.5	99.2	99.3	99.5	99.3	

A few limitations of the quantification technique by XRD and Rietveld modelling should be pointed out:

- Only crystalline phases are possible to detect by XRD analysis. This means that amorphous phases and extremely fine grained minerals are not included in the results.
- Subtraction of the background intensity is not straightforward in the XRD analysis of bentonite. In the present analyses this fact may have led to an underestimation of the plagioclase content because of the interference between the strongest plagioclase reflections and the montmorillonite 003 basal reflection. As a consequence, other minerals may be slightly overestimated.
- The reported mean error of fit (m.e.o.f.) relates to the mathematical accuracy alone and underestimates thereby the total possible error, i.e. effects related to background subtraction, amorphous content etc.

Three obvious tendencies are revealed in the quantitative data, one being the change of the calcium sulphate phase from gypsum to anhydrite in the warmer inner part of the bentonite, one being the loss of calcium carbonate (calcite) in the inner part of the bentonite, and one being a marked decrease of cristobalite in the bentonite in close proximity to the iron heater (Figure 3-9).

The two-dimensional hk-band d(060) in the region 60–64°2θ is shown in Figure 3-10, where the left diagram is a close-up of the XRD-profile of the random powders of the bulk samples, and the right diagram is a high resolution scan of random powders of the <0.5 µm fractions. The (060) reflection allows the distinction between di- and trioctahedral sub-groups of clay minerals because it includes the *b* cell dimension, which is sensitive to the size of the cations and to site occupancy in the octahedral sheet. A d(060) value of 1.49–1.50 Å (62° 2θ) is typical of the dioctahedral sub-group of smectites, to which montmorillonite belongs, whereas the trioctahedral smectites have a d(060) value of 1.52 Å or larger. The exceptions are saponite (trioctahedral) and nontronite (dioctahedral), which both have values of 1.520 Å for d(060).

The d-value of the (060) peak in both scans is more or less identical in all samples (~1.50 Å), and provide no obvious evidence of a change in the *b* cell dimension of the clay mineral, which would be an expected effect of, for instance, a change of the cations or the site occupancy in the octahedral sheet, or of a change of the amount of Al in tetrahedral coordination, as was indicated in the structural formula of sample A30. However, in contrast to the rest of the diffractograms, the background is raised on the low-angle side of the (060) peak in both scans of sample A30, and a broad, diffuse reflection may possibly exist at ~60.6° 2θ (1.528 Å). Quartz has a peak of low intensity at 1.541 Å, which may interfere with the (060) peak in the XRD-profile of a bulk samples, but the <0.5 µm fraction is free of quartz at the detection limit of XRD. Identification of the phase that produces this subtle and diffuse change in the diffraction pattern is not possible based on the available XRD-data.

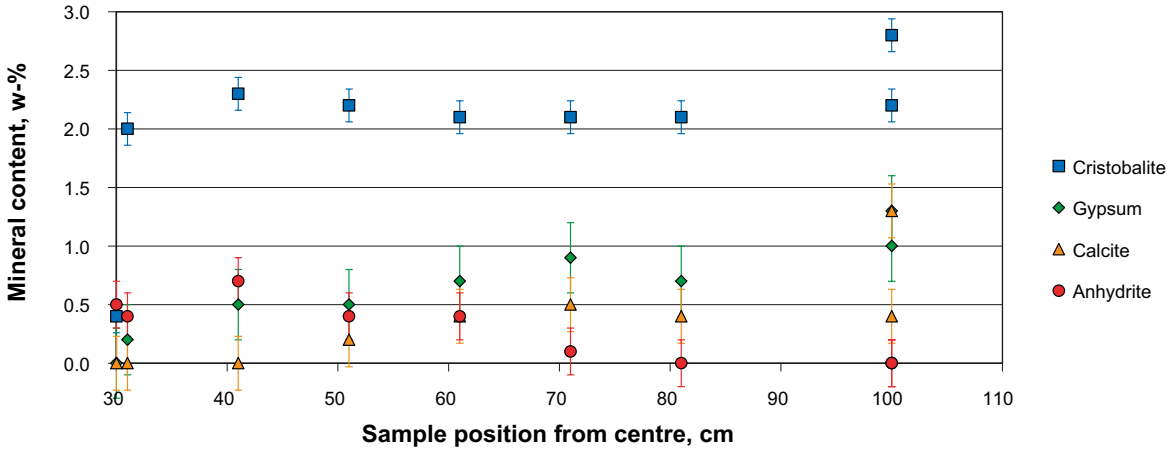

Figure 3-9. *Content of cristobalite, gypsum, calcite and anhydrite versus radial distance in the analysed section. Results for the reference samples Rb-1 and Rb-2 are shown at the fictive distance 100 cm.*

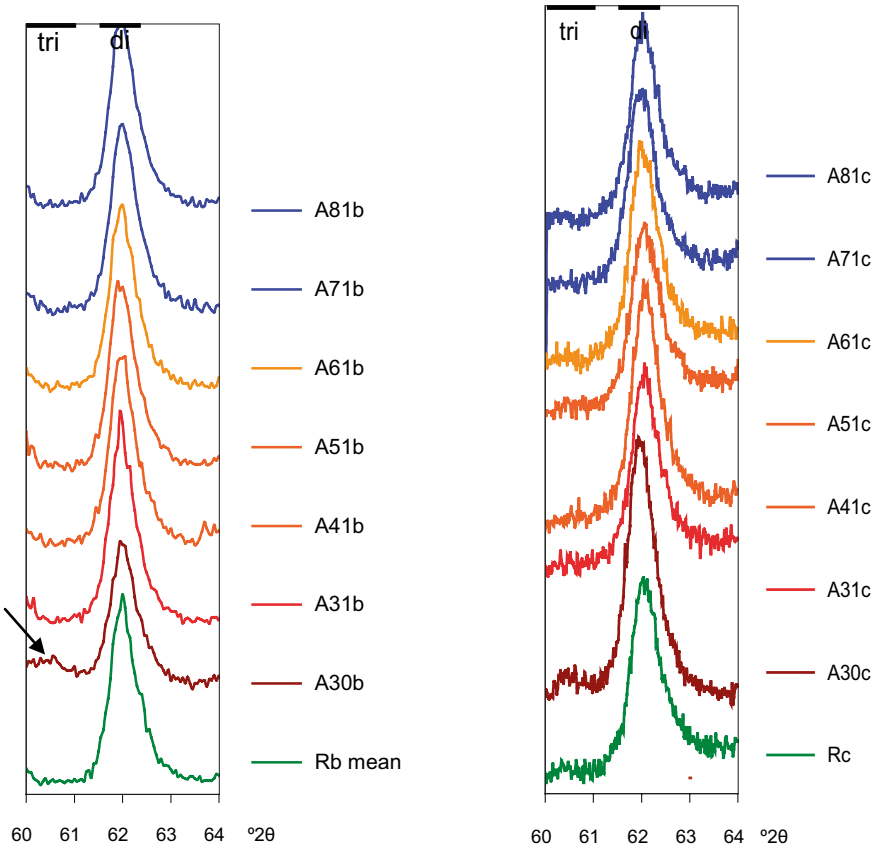

Figure 3-10. *The (060) peak. Left: Close-up of the XRD-profiles of the bulk samples. Right: High resolution scan of the <0.5 µm fractions. Random powders. CuKα radiation.*

XRD-profiles of oriented mounts of the Mg-saturated, air-dried and EG-solvated <0.5 µm fraction of the two innermost samples are shown in Figure 3-11 together with one reference sample. Traces of cristobalite may still occur, but apart from this mineral, the fine clay fractions appear to be pure montmorillonite. The air-dried samples have a basal spacing ranging from 14.7 to 14.9 Å (relative humidity 50±10%) and the diffraction patterns of the block samples match the basic features of the reference sample, but the higher order basal reflections of sample A30 are broader. Peak broadening may be an indication of mixed-layering, but in the EG-solvated state all samples produce a complete rational series of basal reflections, which is indicative of well-ordered stacking sequences with virtually no interstratification. No difference is seen in the expansion behaviour of the clays, which all expand to approximately 16.9 Å upon EG-solvation.

In summary, the available XRD data provide no clear evidence of any structural changes in the montmorillonite. Those changes that exist in the chemical composition of some of the <0.5 µm fractions cannot be coupled to changes in the XRD characteristics of the montmorillonite or to neoformed crystalline phases. However, the resolution of the XRD-technique may be inadequate for detecting small-scaled structural changes and poorly crystallized and/or X-ray amorphous phases may escape detection completely.

3.3.7 Transmission Electron Microscopy (TEM)

Analyses of isolated particles from the fine fractions (<0.5 µm) were made on reference and Fe/bentonite interface material. No significant morphological differences were found. Typical montmorillonite structures dominated both materials (Figure 3-12, left), but more grain-like structures (Figure 3-12, point 7) were occasionally found.

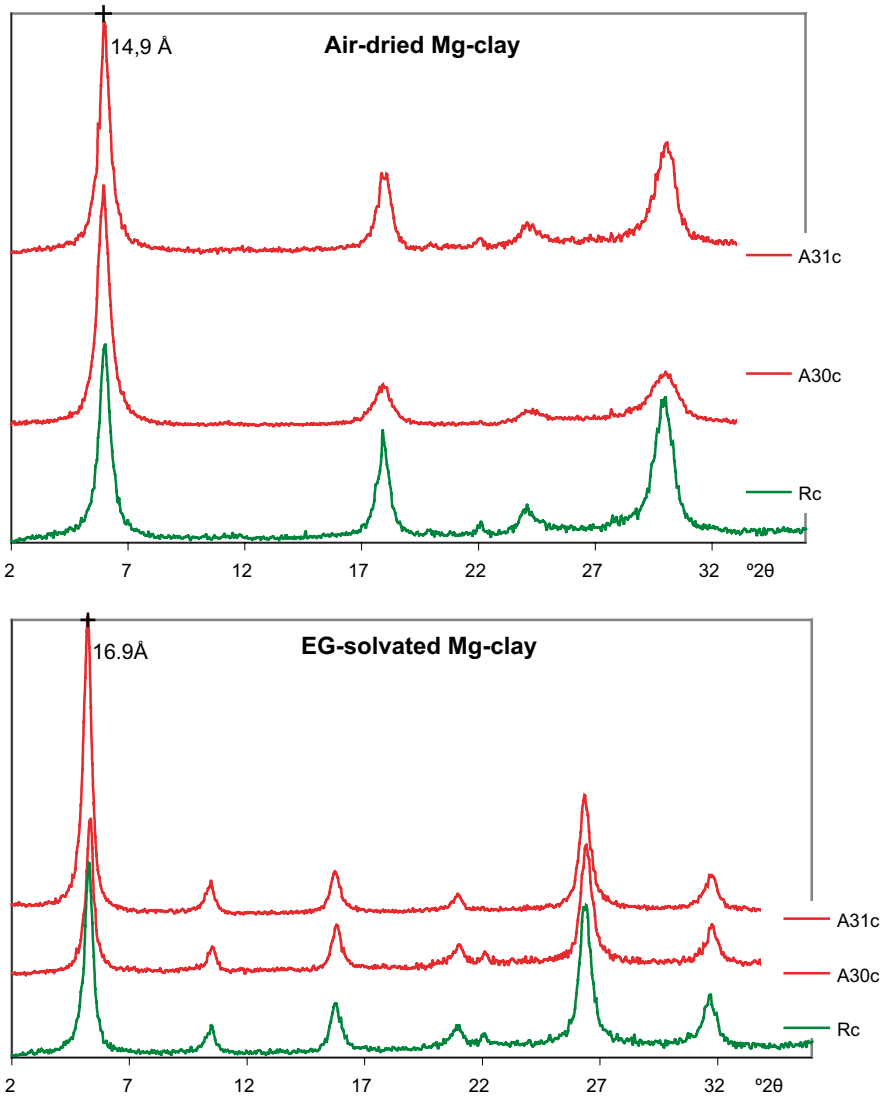

Figure 3-11. *XRD-profiles of Mg-saturated samples of the <0.5 µm fractions of samples A30, A31, and the reference sample. Upper diffractograms show the air-dried samples; lower diffractograms show the EG-solvated samples. CuKα radiation.*

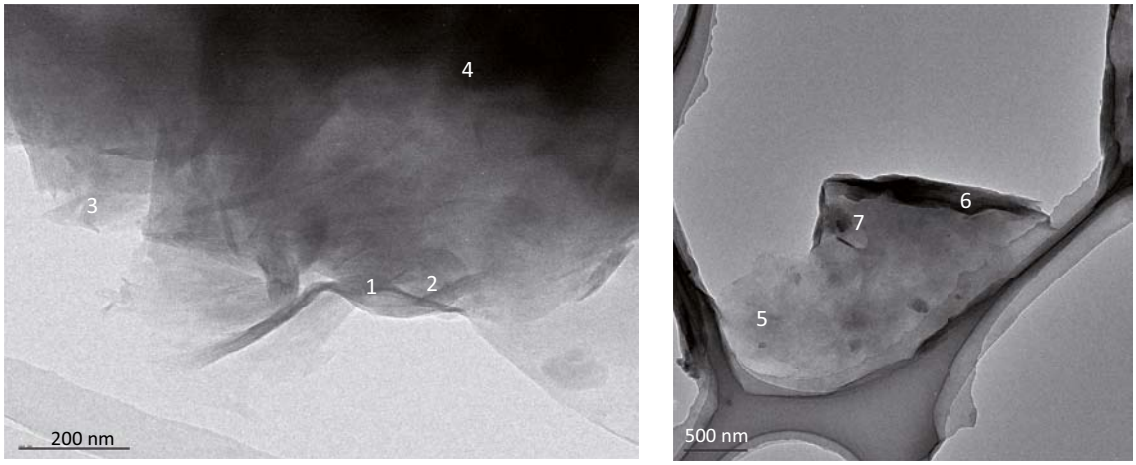

Figure 3-12. *TEM images from typical clay structures in the vicinity of the bentonite/iron interface. The figures 1 to 7 in the images refer to the points where the spectra in Table 3-11 were recorded.*

Table 3-11. Spectra from clay in the vicinity of the bentonite/iron interface. All results in atomic %.

Spectrum	O	Na	Mg	Al	Si	K	Ca	Fe	Zn
Spectrum 1	63.78	0.36	1.78	9.76	23.07	0.09	0.05	0.96	0.16
Spectrum 2	62.12		1.34	10.38	25.01			1.01	0.14
Spectrum 3	68.06		1.73	8.4	20.83			0.79	0.19
Spectrum 4	62.5	0.56	1.98	9.45	23.54	0.11	0.04	1.66	0.15
Spectrum 5	72.85			6.24	20.48			0.44	
Spectrum 6	70.73	0.72	2.36	6.95	17.87	0.08	0.05	1.17	0.07
Spectrum 7	70.98	0.62	2.09	4.25	21.14	0.08		0.73	0.1

Most analyses (Figure 3-12) showed element compositions typical for montmorillonite (Table 3-11), but the grain-like structures had significantly increased Si/Al ratio (spectrum 7). Spectra 1, 4 and 6 represents typical montmorillonite structures and include all relevant elements, and may thereby be used for calculating structural the formulas as follows:

Spectrum 1: $Si_{7.90}\ Al_{0.10}\ Al_{3.24}\ Fe\ (III)_{0.33}\ Mg_{0.61}\ Ca_{0.02}\ K_{0.03}\ Na_{0.12}$

Spectrum 4: $Si_{7.83}\ Al_{0.17}\ Al_{2.98}\ Fe\ (III)_{0.55}\ Mg_{0.66}\ Ca_{0.01}\ K_{0.04}\ Na_{0.19}$

Spectrum 6: $Si_{7.75}\ Al_{0.25}\ Al_{2.76}\ Fe\ (III)_{0.51}\ Mg_{1.02}\ Ca_{0.02}\ K_{0.03}\ Na_{0.31}$

The content of Na^+ in all the three formulas is unrealistically low compared to what is expected from the cation exchange capacity and the fact that the material has been ion-exchanged against Na^+. Since the low Na^+ value likely is related to the analytical problem with lighter elements, we may re-calculate the formulas by use of a realistic Na^+ value in order to compare the present TEM results with the ICP/AES based formulas. Using the Na^+ value which gives the measured CEC and the mean value of the above spectrums we get the following mean structural formula for the A30c montmorillonite structure:

$$Si_{7.75}\ Al_{0.25}\ Al_{2.88}\ Fe\ (III)_{0.46}\ Mg_{0.76}\ Ca_{0.02}\ K_{0.03}\ Na_{0.65}$$

The result may thereby be compared with the ICP/AES results in Table 3-8, which in principle include the same type of information.

3.3.8 Scanning Electron Microsopy (SEM)

SEM/EDX element analyses of the heater surface material were used to check if the steel itself, or remnants from blast sand, could be the source of the accumulated magnesium found in the inner part of the bentonite. No indications of blast sand was however found, and the Mg content in the steel alloy was insignificant. There was consequently no indication that the heater was the origin of the accumulated magnesium.

The exposed bentonite was studied radially from the steel/bentonite interface and outwards with respect to visible precipitates and element distribution. The general picture was that no significant morphological differences were found along the studied radius. The only exception was distinct iron-rich clusters which were found in the proximity of the steel/bentonite interface. The size of the individual clusters was less than 50 µm. The iron content in the clusters was however up to 50% by weight according to the EDX analyses. Figure 3-13 shows a standard image (left) and a backscatter image (right) of the same cluster-rich area.

Generally, there is a significant scatter in measured element distribution in this kind of SEM/EDX analyses, partly due to true local variation in the element distribution in the MX-80 bulk material, and partly due to steric artefacts related to the sample preparation. In order to minimize the scatter and study the general trends, area analyses (A = 250 µm × 250 µm) were performed at increasing distances from the iron/bentonite interface. The results showed the typical element distribution in MX-80 bentonite, but with significantly higher content of iron and magnesium in the innermost centimetres (Table 3-12 and Figure 3-14).

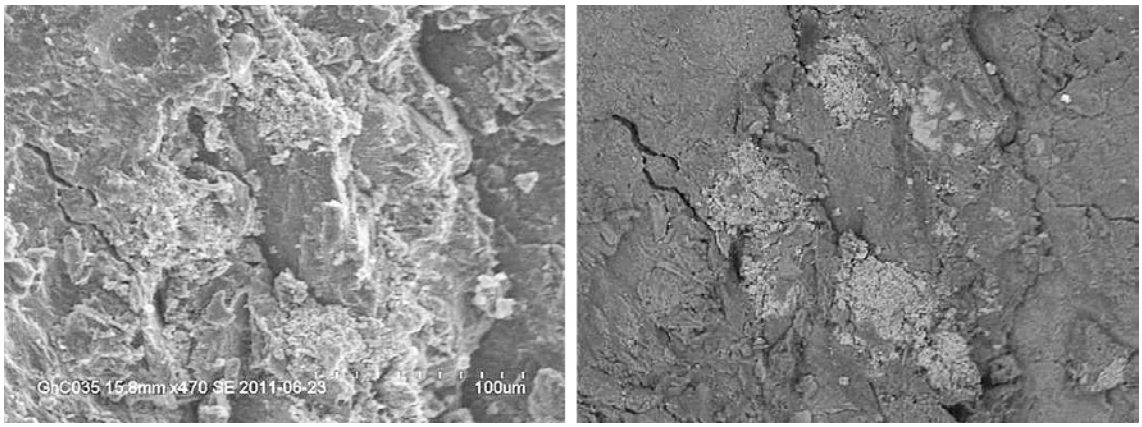

Figure 3-13. SEM-photos of iron-rich clusters in the proximity of the steel/bentonite interface. Left: standard image (from secondary electrons) of an area with several iron-rich clusters. Right: the same area recorded by backscatter electrons, in which the iron-rich clusters appear brighter.

Table 3-12. Measured distribution of elements at different distances from the steel/bentonite interface. Figures show atomic % and represent the mean content in a 250 µm × 250 µm area.

Element	Mid position of analyses in mm from Fe interface											
	0.125	0.25	1	1	2	5	10	20	20	50	100	150
Na	1.8	1.6	1.8	1.6	1.6	1.3	1.8	1.8	1.7	1.7	1.4	1.9
Mg	5.4	5.1	4.4	4.3	4.3	2.9	2.9	2.9	2.7	2.6	2.6	2.8
Si	25.5	26.7	26.5	26.4	26.4	28.2	28.3	28.3	28.9	29.1	28.8	28.9
K	0.3	0.3	0.2	0.1	0.1	0.3	0.3	0.3	0.3	0.3	0.3	0.2
Ca	0.3	0.5	0.5	0.6	0.6	0.7	0.7	0.7	0.8	1.0	0.9	0.6
Fe	4.0	2.8	3.3	3.7	3.7	2.4	2.2	2.2	1.3	1.2	1.7	1.4
O	62.8	63.1	63.2	63.3	63.3	64.1	63.9	63.9	64.1	64.2	64.2	64.1

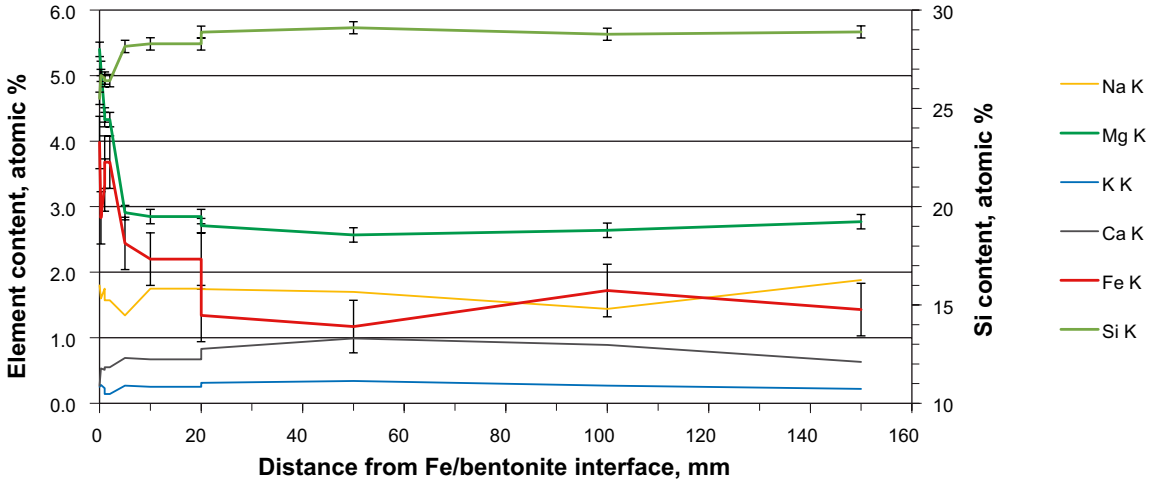

Figure 3-14. Mean results from SEM/EDX areas analyses (A = 250 × 250 µm^2) plotted against the distance from the iron/bentonite interface to the area midpoint. Error bars indicate ± 1 stdv based on 5 analyses in the outer part of the bentonite.

4 Mössbauer and FTIR analyses

4.1 Mössbauer spectroscopy

4.1.1 Methods

Six samples (TR03-ref (samples 1 and 2), TR03_250_C31, TR03_250_C33, TR03_250_C35 and TR03_250_C39 were studied with Mössbauer spectroscopy. Samples were dried in N_2-atmosphere inside a glovebox and ground to a fine powder (at Clay Technology AB). Samples were sent to Åbo Akademi under N_2-atmosphere, where the samples were placed immediately to glovebox (concentration of O_2/H_2O less than 1 ppm). Each sample was prepared at maximum a few days before the measurement was started. 50 mg of sample powder was mixed with epoxy glue in an Al-cup in N_2-atmosphere. The mixture was spread evenly on the bottom of Al-cup (area of ~3 cm^2), air bubbles (if present) were pierced with a needle and the samples were allowed to dry in a glovebox in N_2-atmosphere. Just before the measurement, sample was taken out from the glovebox.. The analyses were carried out by Johan Lindén, Åbo Akademi, Department of Physics.

First, all spectra were collected at 77 K in transmission mode using a sinusoidal velocity scale with a maximum Doppler velocity of 10.1 mm/s. The velocity was chosen to allow detection of the magnetic lines of Fe oxides and hydroxides. For paramagnetic samples this scale was a bit too large, but weak magnetic lines were anticipated to be present (Kumpulainen et al. 2011), hence this velocity scale was chosen. The 77 K temperature prevents the oxidation of the samples during the long measurement. The geometry, i.e. source-to-detector distance, absorber area and collimation was the same for all samples, as well as the settings for the gamma-ray window. Data were collected for six days for each sample, yielding a folded background level of ~$25 \cdot 10^6$ counts. The sample TR03-ref-1 was measured first and sample TR03-ref-2 was measured after all other samples were measured.

Sample cooling was achieved using an Oxford ITC-4 continuous-flow cryostat operated with liquid nitrogen. The 14.4-keV Mössbauer quanta were produced by a Cyclotron Co. ^{57}Co:*Rh* (25 mCi April 2009) source and detected using a LND 4546 proportional counter with a beryllium window. A Fast ComTec MA-250 velocity transducer was used for moving the source. It was equipped with a Halder MR-351 drive unit. The data was gathered using a Fast ComTec MCA-3 multichannel-analyzer PCI card in an ordinary desktop PC. The measurements were done in a multiscaling mode. The spectra were fitted using a home-made nonlinear least-squares fit program, utilizing spectral components corresponding to four paramagnetic doublets and one magnetic sextet. For the paramagnetic components, fit parameters were quadrupole splitting (Δ in mm/s), isomer shift (δ with respect to α-Fe in mm/s) and spectral intensities (I in %). For the magnetic component, the internal field (B in T) and its gaussian distribution (ΔB in T) were included as fit parameters as well. All components were constrained to have a common line width (Γ in mm/s). An alternative fit, including only three spectral components, was also prepared.

In addition, reference 1 and sample C33 were re-measured using a lower Doppler velocity of 4.59 mm/s at maximum. The lower velocity was chosen in order to detect the paramagnetic main components better. The old absorber of sample C33 was first re-measured, but it was noticed that the absorber had oxidized. Hence, new sample mounts were prepared from sample materials, which were stored under N_2 atmosphere. For these measurements data was collected for one week. In the fit of these measurements, the magnetic component seen in the 10.1 mm/s measurements was kept fixed at the parameter values observed earlier.

4.1.2 Results and discussion (5 component fit, high velocity)

The fitted Mössbauer spectrum for sample TR03-ref 1 is displayed in Figure 4-1. Spectra for other samples are presented in Appendix 1. The fittings and major part of the discussion are provided by Johan Lindén, Åbo Akademi. The five spectral components, all corresponding to various Fe species are shown. By visual inspection all samples are rather similar. The reference samples have considerably larger line widths (0.39 and 0.41 mm/s) than samples C31–C39, perhaps due to less perfect crystallinity caused by oxidation.

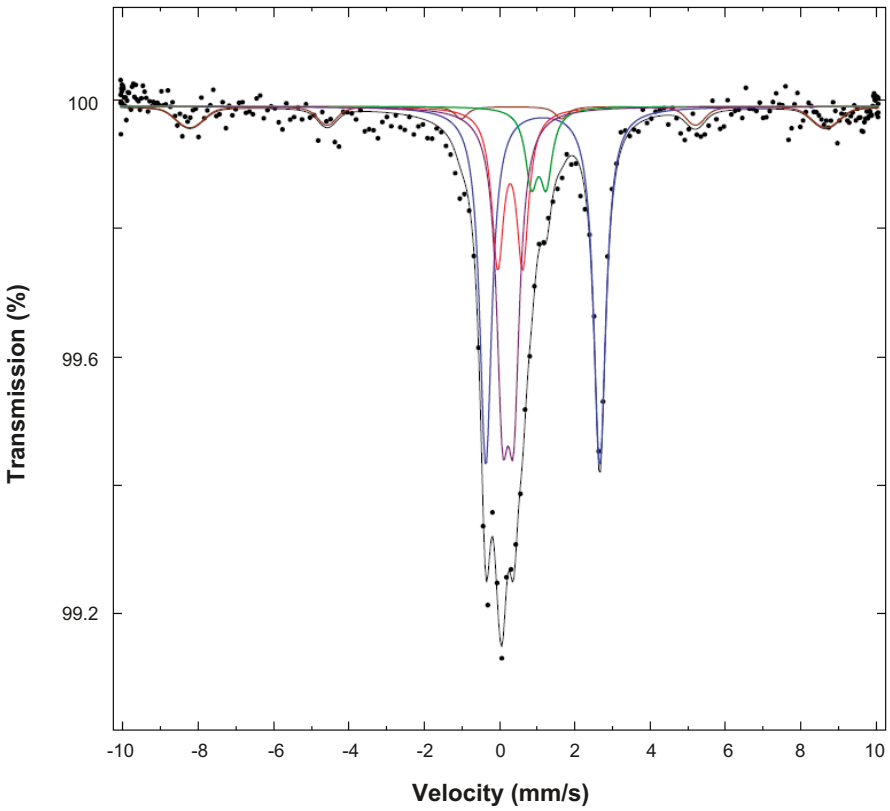

Figure 4-1. *Mössbauer spectrum recorded from sample TR03-ref1 at 77 K. Components of the fit are displayed above the spectrum. They are: component 1 in blue, component 2 in red, component 3 in violet, component 4 in brown and component 5 in green.*

In all the spectra, the dominating component is paramagnetic with a very large quadrupole coupling constant $eQV_{zz} \approx 3.0$ mm/s (component 1 in Table 4-1). This component also has a large isomer shift, which is typical of divalent Fe. The same feature was reported in the study by Carlson et al. (2007). The second divalent component (component 5, in Table 4-1) has a very high isomer shift, compatible only with high-spin Fe^{2+}, like component 1. However, the quadrupole splitting for component 5 is much smaller than for component 1. Therefore it must originate from a different surrounding than component 1.

On the inner slope of the first line of component 1 additional paramagnetic features are seen. These peaks were accounted for using two quadrupole components (components 2 and 3, in Table 4-1), as a single component was not enough to explain these features. Both components can be attributed to trivalent Fe, based on their isomer-shift values. Only one such component was reported by Carlson et al. (2007). However, they might correspond to almost the same chemical environment, reflecting a less than perfect local crystallinity of the trivalent Fe species.

All the spectra exhibit weak magnetic features, which were fit using an ordinary magnetic sextet (component 4, in Table 4-1). Due to the very low concentration of magnetic iron the fitted parameters of the magnetic Mössbauer component are very uncertain. When a paramagnetic doublet becomes magnetically split all the intensity is distributed over six resonance lines and the detection limit increases approximately with a factor of 4, i.e. the concentration of a hypothetical magnetic Fe species could be four times higher than a paramagnetic one and still remain undetected in the Mössbauer spectrum. The fitted internal field for the magnetic component (component 4) was 50–55 T, with uncertainties of at least 1 T. These values should in principle be due to Fe^{3+}, as divalent Fe seldom exhibits internal field exceeding ~48 T. Also the isomer shift values of 0.30–0.58 are compatible with high-spin Fe^{3+}. There is also a possibility that there is more than one magnetic component, which can't be ruled out due to the very weak statistics for the magnetic lines. A rough estimate of the concentration of magnetic trivalent iron in the samples is 4–8% of the total intensity, i.e., of the total amount of iron in the samples (Table 4-1).

Table 4-1. Hyperfine parameters.

Sample	Component	I (%)	Δ (mm/s)	δ (mm/s)	B (T)	Γ (mm/s)
TR03-ref-1	Component 1	38.9	3.028	1.261		0.386
	Component 2	16.4	0.66	0.40		0.386
	Component 3	28.8	0.29	0.34		0.386
	Component 4	8(1)	–0.1(1)	0.38	52(1)	0.386
	Component 5	7.7	0.29	1.16		0.386
TR03-ref-2	Component 1	36.2	3.023	1.275		0.410
	Component 2	20.9	0.73	0.42		0.410
	Component 3	29.7	0.28	0.35		0.410
	Component 4	7(1)	0.2(1)	0.30	55(1)	0.410
	Component 5	6.3	0.28	1.39		0.410
TR03_250_C31	Component 1	39.3	3.045	1.261		0.343
	Component 2	20.1	0.73	0.42		0.343
	Component 3	28.1	0.31	0.37		0.343
	Component 4	7(1)	–0.4(1)	0.49	55(1)	0.343
	Component 5	5.3	0.29	1.24		0.343
TR03_250_C33	Component 1	41.8	3.035	1.258		0.318
	Component 2	17.3	0.71	0.41		0.318
	Component 3	29.0	0.29	0.35		0.318
	Component 4	8(1)	–0.2(1)	0.53	50(1)	0.318
	Component 5	3.8	0.29	1.26		0.318
TR03_250_C35	Component 1	42.6	3.049	1.265		0.338
	Component 2	16.9	0.82	0.43		0.338
	Component 3	32.3	0.33	0.38		0.338
	Component 4	4(1)	–0.5(1)	0.35	52(1)	0.338
	Component 5	3.9	0.31	1.41		0.338
TR03_250_C39	Component 1	39.4	3.041	1.265		0.327
	Component 2	16.7	0.81	0.44		0.327
	Component 3	33.9	0.32	0.37		0.327
	Component 4	6(1)	–0.2(1)	0.58	50(1)	0.327
	Component 5	4.0	0.34	1.47		0.327

Assignments of different components to minerals

Fe^{3+} and Fe^{2+} in clay minerals can easily be distinguished by their isomer shifts and quadrupole splittings (Wagner and Wagner 2004). Tetrahedral and octahedral Fe^{3+} also differ slightly in isomer shifts (Wagner and Wagner 2004). However, due to several possible locations/environments, where Fe^{3+} or Fe^{2+} can be located in clay minerals and because clay minerals occur commonly as mixtures, usually a distribution of ill resolved quadrupole doublets can be observed for both trivalent and divalent iron in clay minerals (Wagner and Wagner 2004).

The largest components in the measured Mössbauer spectra, i.e., components 1, 2 and 3 can be assigned to iron in clay minerals (Hogarth et al. 1970, Wagner and Wagner 2004). If interactions with heater would have occurred, probably the component 1 would have grown as in Kumpulainen et al. (2011). This growth could be caused by adsorption of Fe^{2+} into smectite structure (edge sites, interlayer sites) or formation of $Fe(OH)_2$, which has similar quadrupole splitting and isomer shift as the values of component 1 (Cornell and Schwertmann 2003). However, only minor or no increase in the amount of Fe^{2+} was observed (depending on the fit and Doppler-velocity) in the studied samples according to the Mössbauer spectral intensities of component 1. No significant changes were seen in the amount of Fe^{3+} in the studied samples.

The quadrupole splitting and isomer shift values of pyrite (Evans et al. 1982) are similar as for components 2 and 3. Hence the spectrum of pyrite might be in the background of the spectra and possibly cause some uncertainty to the fitted parameters.

Mössbauer spectra are often measured in different temperatures due to different temperature dependencies of Mössbauer spectra of different iron-bearing minerals (Wagner and Wagner 2004). For instance some minerals may order magnetically at low temperatures or the quadrupole splitting of divalent iron may show temperature dependence (Wagner and Wagner 2004). At the used measurement temperature (77 K) maghemite, hematite and goethite all appear as magnetically split sextets in Mössbauer spectra unless superparamagnetism is present (Cornell and Schwertmann 2003). Also magnetite is magnetically split at the measurement temperature (Cornell and Schwertmann 2003). Hence, the magnetically split component (component 4) may be a combination of the spectra of these minerals. Due to low amount of these phases, they cannot be resolved from the background of collected Mössbauer spectra.

Component 5 could be caused by some other Fe^{2+}-containing mineral in the sample materials.

Fe^{2+}/Fe^{3+}-ratio

The main result of the analyses, i.e., the ratio of paramagnetic Fe^{2+} to Fe^{3+}, is readily obtained from Table 4-1. Assuming the recoil-free fraction to be the same for all components, the valence ratio is the intensity of components 1 + 5 to that of components 2 + 3 (Table 4-2). It is assumed that pyrite (Fe^{2+}) has no significant effect on components 2 and 3, which were assigned to Fe^{3+}.

Results from other studies are presented in Table 4-3 for comparison. In Kumpulainen at al. (2011) Mössbauer spectra was fitted with four components similarly as in this study, but without the second Fe^{2+} component (component 5). Hence, the Fe^{2+}/Fe^{3+}-ratios in this fit are similar as the ratio for the reference sample in Kumpulainen et al. (2011).

According to the results presented in Table 4-2, the ratio of Fe^{2+} and Fe^{3+} has not changed significantly. The variation in the intensities of different components of reference samples is of the same magnitude as the variation in the intensities of TBT-samples (C31, C33, C35 and C39) (Table 4-1). Some changes could have been seen in samples taken very close from the iron contact (within 5 mm) as in Kumpulainen et al. (2011) and Carlson at al. (2007). However, due to the large scale of the TBT test, it was impossible to dismantle the test under N_2-atmosphere as in Kumpulainen et al. (2011) and Carlson at al. (2007). To avoid error resulting from oxidation of the sample during dismantling, the closest TBT Mössbauer sample (C31) was taken 10 mm from the heater from a piece, which was thought to not been exposed to air.

Table 4-2. Ratio of Fe^{2+} to Fe^{3+}.

Sample	Fe^{2+}/Fe^{3+} (paramagnetic only, components 1,2,3,5)
TR03-ref-1	1.03
TR03-ref-2	0.84
TR03_250_C31	0.93
TR03_250_C33	0.99
TR03_250_C35	0.95
TR03_250_C39	0.86

Table 4-3. Mössbauer Fe^{2+}/Fe^{3+} results from other iron-bentonite interaction studies.

Sample	Fe^{2+}/Fe^{3+}
Sample 23. Reference (Kumpulainen et al. 2011)	1.024
Sample 33a. FeBe (Kumpulainen et al. 2011)	1.543
Sample 37. Corrosion products (Kumpulainen et al. 2011)	2.264
MX-80 (Carlson et al. 2007)	0.565
Coupon 30°C (Carlson et al. 2007)	0.605
Coupon 50°C (Carlson et al. 2007)	0.541
Wire 30°C (Carlson et al. 2007)	2.861
Wire 50°C (Carlson et al. 2007)	3.545

According to chemical analysis results, the amount of total iron had increased approximately 0.3 wt.% (calculated as the fraction of Fe_2O_3 from the total amount of elements presented as oxides) on average in the first 20 mm from the heater in TBT test. In Kumpulainen et al. (2011) the amount of iron had increased approximately 1 wt.% in the first 1.5 mm from the cast iron. In Carlson et al. (2007) the amount of iron had increased even more. Hence, the differences in this study are probably too small to be detected reliably with Mössbauer spectroscopy (at least when compared to the variation between the two reference samples in this study).

4.1.3 Alternative fitting (3 component fit, high velocity)

In addition, the Mössbauer spectra were fitted similarly as in Carlson at al. (2007) resulting only in three components (in Carlson et al. (2007) only two components were used, i.e., no magnetic component was detected). Component 1 is assigned to Fe^{2+} in clay minerals, component 2 to Fe^{3+} in clay minerals and component 3 (magnetic) to some accessory mineral(s) in the sample. The hyperfine parameters of these components are presented in Table 4-4. The hyperfine parameters of component 3 suggest that it is also caused by trivalent iron (see section 4.1.2). The intensity of component 1 has increased slightly in samples C31, C33 and C35 compared to reference samples and sample C39, which indicates that the amount of Fe^{2+} has increased slightly in the samples. The intensity of component 2 and thereby the amount of Fe^{3+} has not changed significantly. The intensity of component 3 has decreased slightly.

Table 4-4. Hyperfine parameters of alternative fitting.

Sample	Component	I (%)	Δ (mm/s)	δ (mm/s)	B (T)	Γ (mm/s)
TR03-ref-1	Component 1	34.1	3.034	1.257		0.386
	Component 2	58.6	0.42	0.38		0.651
	Component 3	7.3	0.37	0.24	52.4	0.386
TR03-ref-2	Component 1	32.7	3.005	1.260		0.411
	Component 2	60.1	0.44	0.38		0.703
	Component 3	7.3	0.27	0.32	54.8	0.411
TR03_250_C31	Component 1	36.5	3.046	1.261		0.341
	Component 2	57.5	0.46	0.38		0.579
	Component 3	6.0	–0.82	0.50	50.1	0.341
TR03_250_C33	Component 1	37.5	3.033	1.261		0.311
	Component 2	55.5	0.41	0.36		0.547
	Component 3	7.0	–0.52	0.53	50.3	0.311
TR03_250_C35	Component 1	37.3	3.046	1.264		0.317
	Component 2	58.9	0.44	0.38		0.598
	Component 3	3.8	–0.91	0.30	52.0	0.317
TR03_250_C39	Component 1	34.6	3.036	1.261		0.294
	Component 2	60.8	0.42	0.36		0.562
	Component 3	4.7	–0.40	0.56	49.8	0.294

The ratio of paramagnetic Fe^{2+} and Fe^{3+} determined from the alternative fitting are presented in Table 4-5. As in section 4.1.2 they are obtained from Table 4-4 as the ratio of the intensities of paramagnetic spectral components (magnetic component was not included). These values resemble the values from Carlson et al. (2007) due to the similar fitting.

Table 4-5. Ratio of Fe^{2+} to Fe^{3+}.

Sample	Fe^{2+}/Fe^{3+} for 3-component fit (paramagnetic only, components 1, 2)
TR03-ref-1	0.58
TR03-ref-2	0.54
TR03_250_C31	0.64
TR03_250_C33	0.68
TR03_250_C35	0.63
TR03_250_C39	0.57

4.1.4 Re-measurement results (low velocity)

The Mössbauer spectra of the new absorbers measured with lower Doppler velocity (4.59 mm/s) are presented in Figure 4-2 and Figure 4-3 (see also Appendix 2). The hyperfine parameters from low-velocity measurements are presented in Table 4-6.

Table 4-6. Hyperfine parameters from low-velocity measurements.

Sample	Component	I (%)	Δ (mm/s)	δ (mm/s)	B (T)	Γ (mm/s)
TR03-ref-1	Component 1	33.20	2.997	1.248		0.379
	Component 2	24.08	0.677	0.403		0.379
	Component 3	38.53	0.282	0.327		0.379
	Component 4	–	–	–	–	0.379
	Component 5	4.20	0.359	1.300		0.379
TR03_250_C33	Component 1	44.90	2.995	1.246		0.319
	Component 2	18.13	0.788	0.484		0.319
	Component 3	35.64	0.338	0.378		0.319
	Component 4	–	–	–	–	0.319
	Component 5	1.30	0.26	1.48		0.319

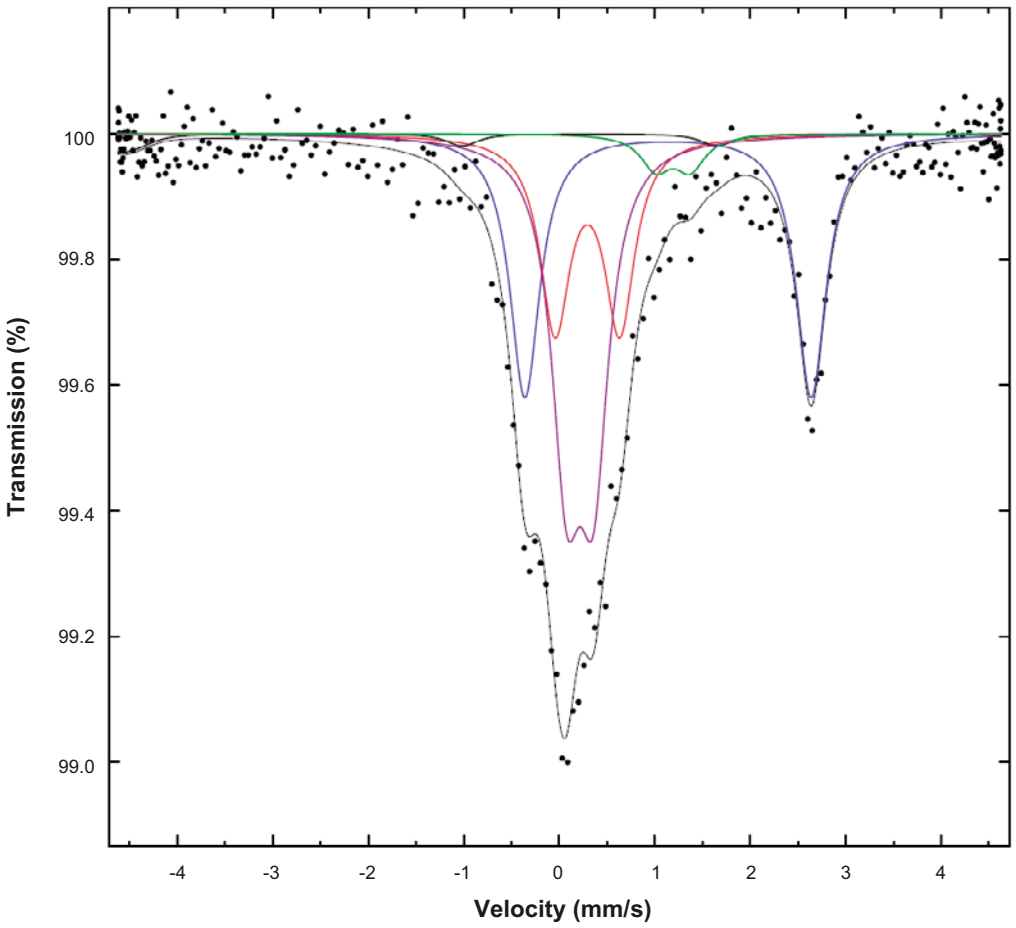

Figure 4-2. *Mössbauer spectrum recorded from reference 1 with the lower Doppler velocity.*

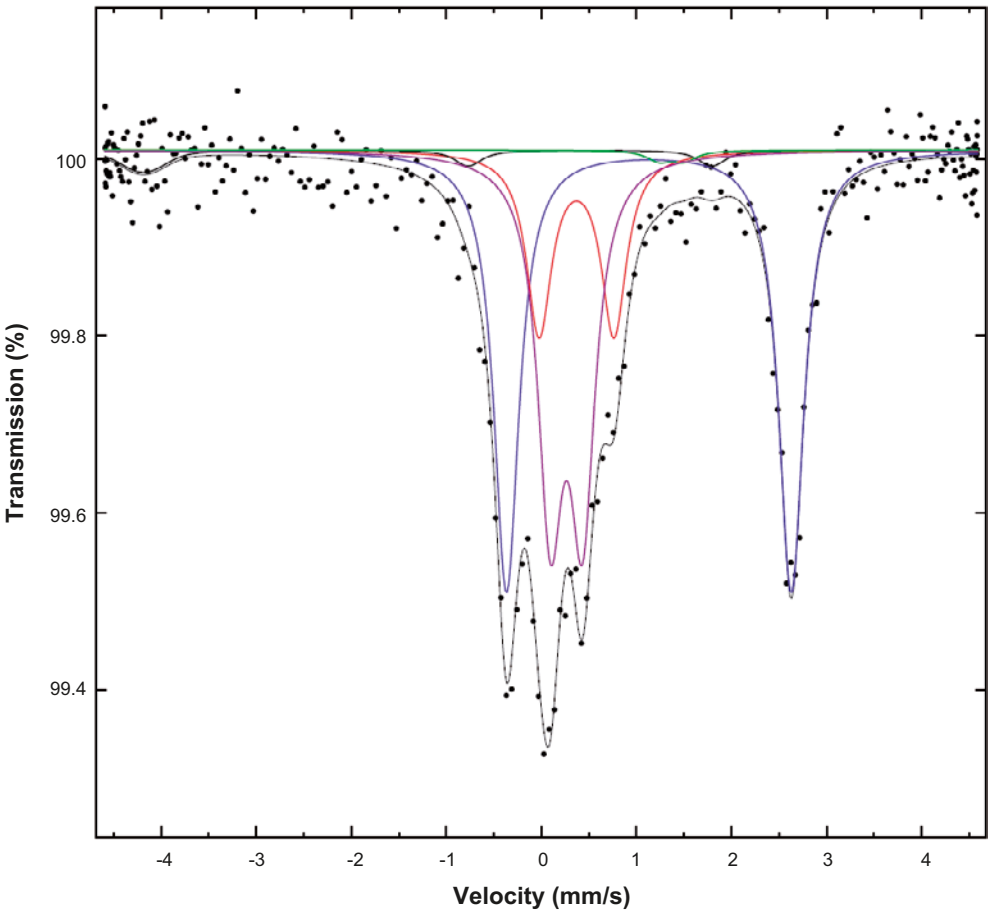

Figure 4-3. *Mössbauer spectrum recorded from sample C33 with the lower Doppler velocity.*

The ratio of paramagnetic Fe^{2+} and Fe^{3+} determined from the measurements with lower Doppler velocity are presented in Table 4-7. As in section 4.1.2 they are obtained from Table 4-6 as the ratio of the intensities of different spectral components.

Table 4-7. Ratio of Fe^{2+} to Fe^{3+}.

Sample	Fe^{2+}/Fe^{3+} from low velocity measurements (paramagnetic only, components 1, 2, 3, 5)
TR03-ref-1	0.60
TR03-ref-2	–
TR03_250_C31	–
TR03_250_C33	0.86
TR03_250_C35	–
TR03_250_C39	–

4.1.5 Comparison of different fits

The spectra measured with lower velocity confirmed that the spectra consists of several components and hence, the 5 component fit presented in section 4.1.2 is better than the simpler 3 component fit presented in section 4.1.3. Also, the intensity estimates for component 5 are considered more reliable in the fit made from low velocity measurements. The Chi-squared values for different fits are presented in Table 4-8.

Table 4-8. Chi-squared values for different fits.

Sample	Chi^2 (high velocity, 5 component fit)	Chi^2 (high velocity, 3 component fit)	Chi^2 (low velocity, 5 component fit)
TR03-ref-1	1.177	1.419	1.164
TR03-ref-2	1.220	1.375	–
TR03_250_C31	1.262	1.446	–
TR03_250_C33	0.926	1.100	0.914
TR03_250_C35	1.187	1.194	–
TR03_250_C39	1.303	1.638	–

4.1.6 Conclusions

Mössbauer spectra of bentonites are usually superpositions of several unresolved spectra due to the fact that bentonites usually occur as mixtures of several clay minerals and accessory minerals, many of them containing iron in different local environments. Hence, the evaluation of the spectra is difficult and usually just general information is gained about the relative amounts of Fe^{2+} and Fe^{3+} in the sample. Three component fit and the measurements with lower Doppler-velocity indicate that the amount of Fe^{2+} has increased slightly (based on this data it cannot be assigned to any specific mineral phase), but the five component fit doesn't support this observation. Hence, the increase in the amount of iron observed with chemical analyses was probably too small to be detected reliably with Mössbauer spectroscopy.

4.2 FTIR – Fourier transform infrared spectroscopy

4.2.1 Materials and methods

Three reference bulk samples (TR04 r bulk a, TR04 r bulk b, and TR04 r bulk c), seven bulk samples from same profile (TR04 032 a30 bulk, TR04 032 a31 bulk, TR04 032 a41 bulk, TR04 032 a51 bulk, TR04 032 a61 bulk, TR04 032 a71 bulk and TR04 032 a81 bulk), two purified and Na exchanged reference clay samples (TR04 rc Na1 and TR04 rc Na2) and one purified and Na exchanged clay samples (TR04 a31c Na) was selected to be analysed with FTIR.

Two mg of sample material was mixed with 200 mg of dry (105ºC) KBr powder in an agate mortar and pressed to 13 mm diameter discs. KBr discs were dried for 20 h at 150 ºC in order to remove adsorbed water. Infrared spectrum was recorded in triplicate both before and after drying using transmission mode in a range from 4,000 to 200 cm^{-1} with Perkin Elmer Spectrum One FTIR spectrometer at the Department of Geology, University of Helsinki. Resolution of scans was 4 cm^{-1}.

Three parallel samples were prepared from reference bulk material to study the analytical errors.

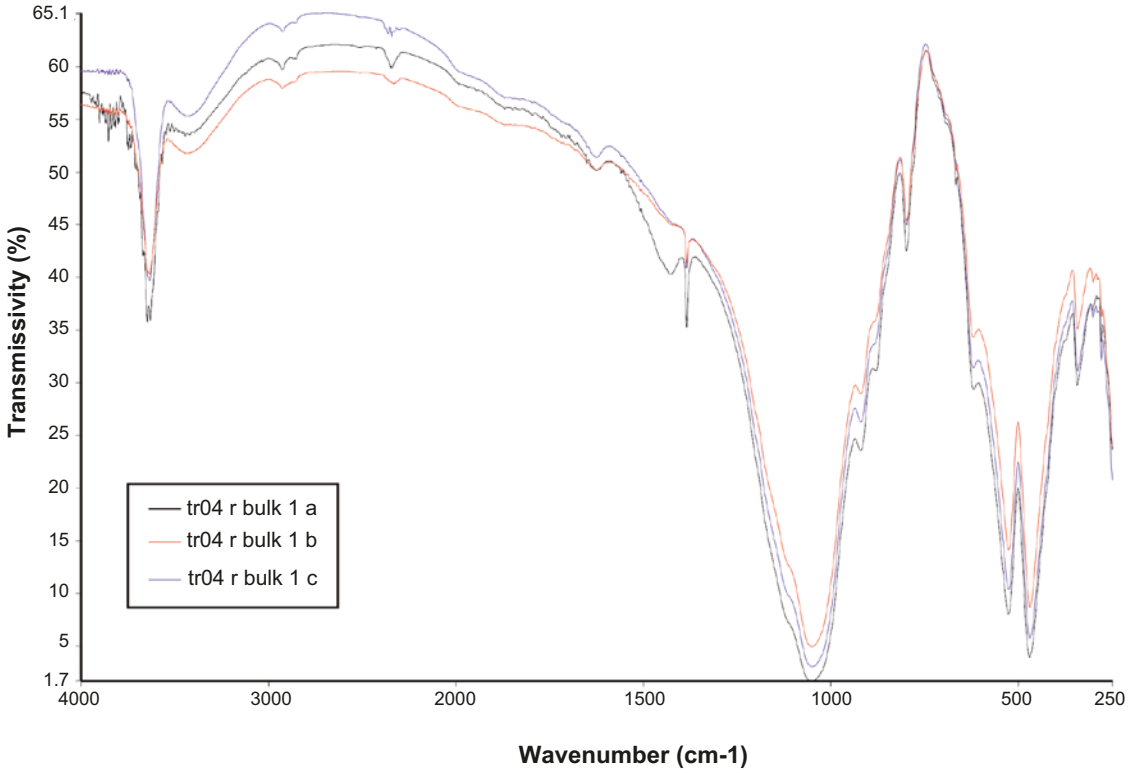

Figure 4-4. *Variances in FTIR patterns of triplicate sample.*

4.2.2 Results and discussion

Reference samples analysed in triplicate showed a small variation in band positions and intensities (Figure 4-4). Such variances may have arisen from different levels of grinding as particle size affects the background noise and band resolution (Russell 1987), as well as true variances in composition due to imperfect homogenization, because the amount of analysed sample is very small (2 mg), and the effect of homogenization is crucial. From analysed triplicate samples 1a seems to contain more carbonates than 1b and 1c indicated by greater absorption at 1,424 cm^{-1} (Figure 4-4). The same sample also shows most background noise indicating imperfect grinding. Observed differences in composition of triplicate samples highlight the importance of homogenization and sampling.

Standard deviation of the positions of major adsorption bands in triplicate sample was ±1 cm^{-1} and that of intensity ±2 cm^{-1}.

Samples analysed from profile TR04 032 showed a decrease in cristobalite (and/or opaline silica) content towards the sample a30 indicated by the decrease in intensity at wavenumbers 1,160, 798, 621, 515, 484 and 302 cm^{-1}. Additionally, potential decrease in calcite content, appearing as wide band at ~1,430 cm^{-1} towards the sample a30 was found. Also potential decrease in intensity of AlAlOH deformation band of smectite located at wavenumber ~920 cm^{-1} was seen in sample a30. No indications for change in band intensities or positions that can be assigned to calcium sulphates were found.

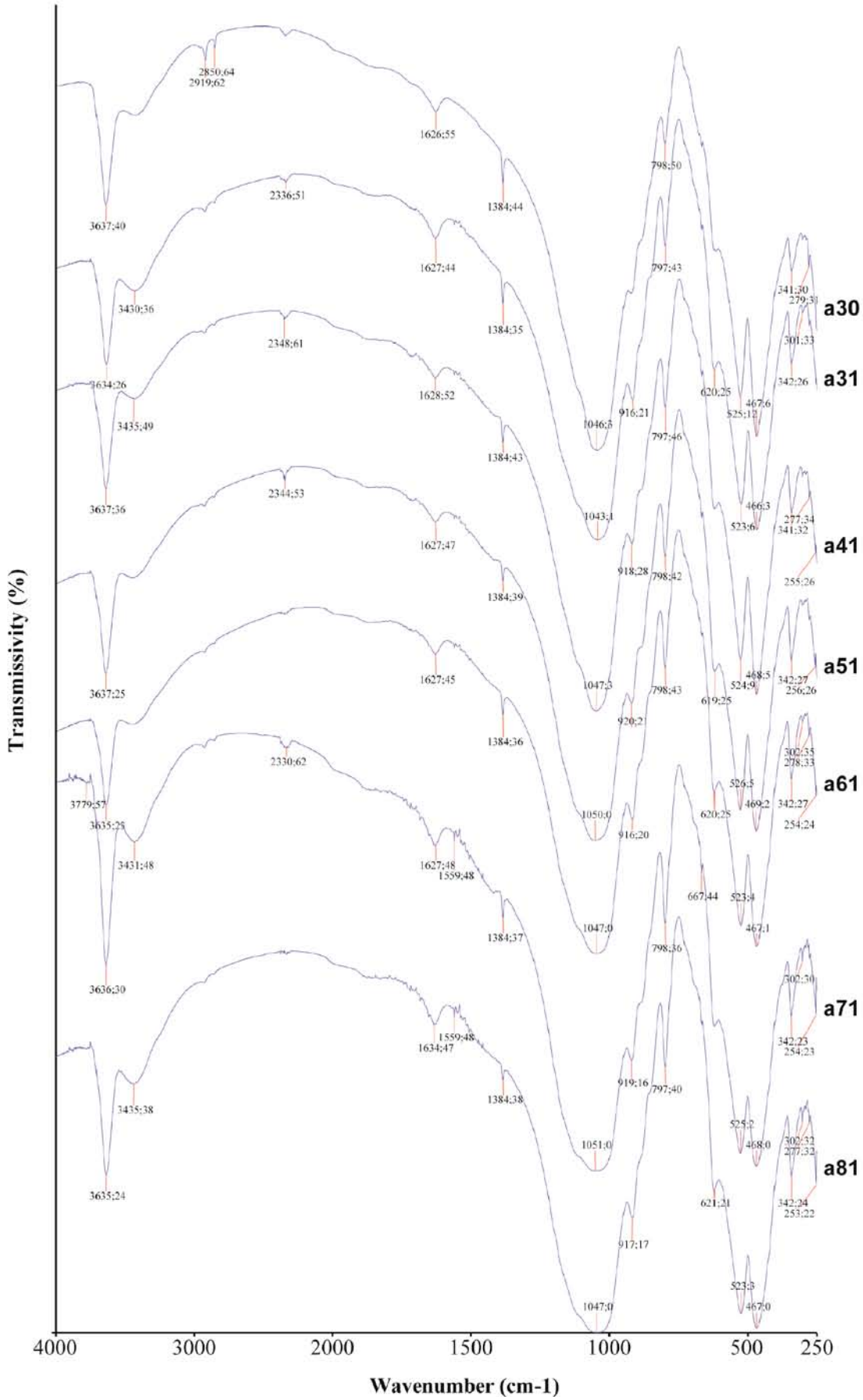

Figure 4-5. *FTIR patterns of samples a30, a31, a41, a51, a61 and a81. Most important band positions and intensities are shown (separated with ; respectively)*

Purified and sodium exchanged clay fractions still showed some impurities; band at 799 cm^{-1} which can be attributed to the presence of cristobalite and/or opaline silica, and many small bands at region 3,000–1,650 cm^{-1} to organic material. Bands assigned to organic material at 3,000–1,650 cm^{-1}, as well as sharp bands at 1,384 cm^{-1} and 667 cm^{-1} that can be assigned to carbonyl groups and adsorbed carbon dioxide have originated from impurities in KBr powder. The differences between the reference samples and the sample a31c were minor. Only small decrease in the intensity of silica band at 798 cm^{-1} was seen.

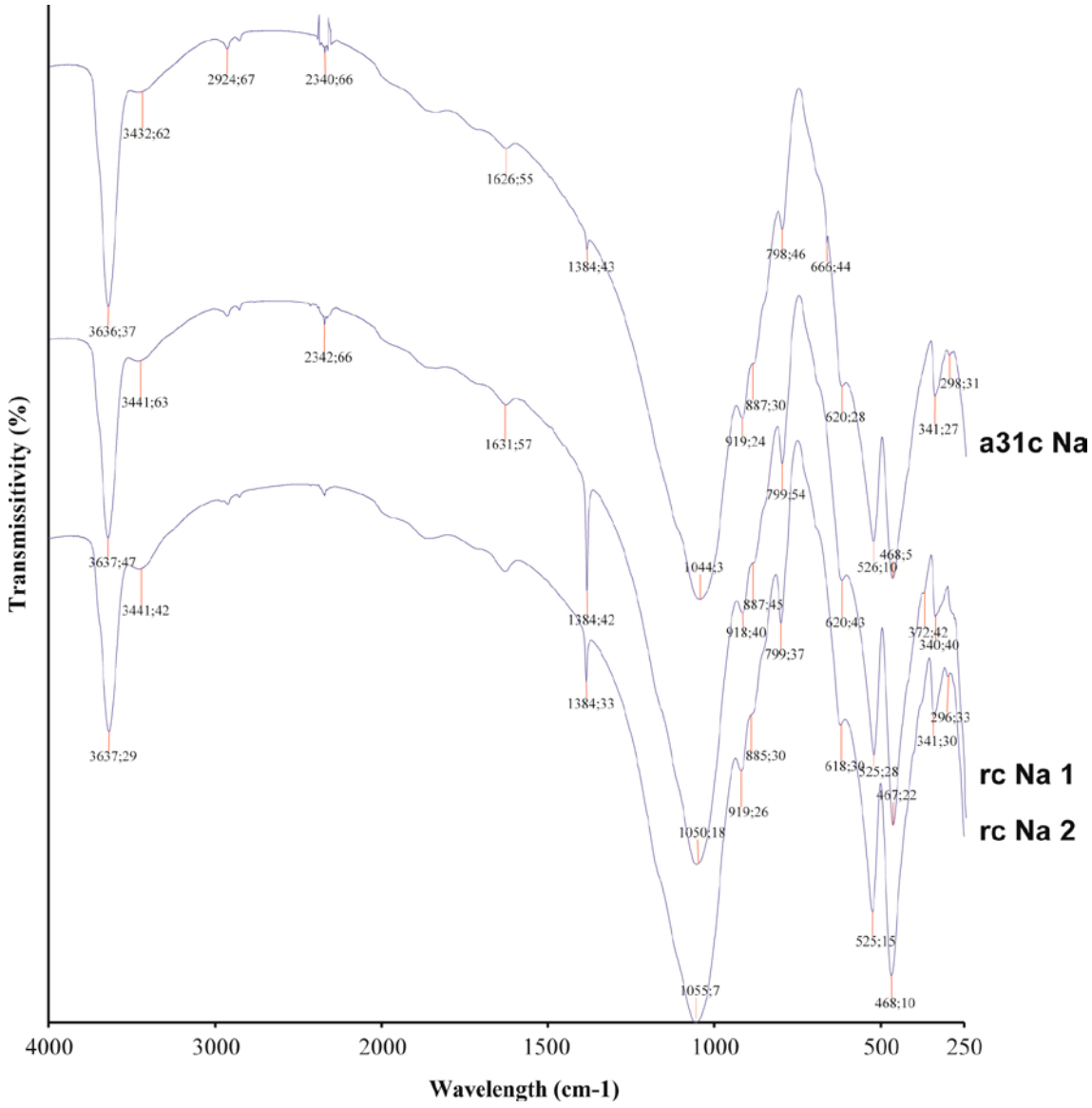

Figure 4-6. *FTIR patterns of purified and sodium exchanged clay (<0.5 µm) fractions.*

5 Summary of chemical/mineralogical analyses

The entire volume of block R4 from the bentonite buffer of the 6-year long TBT field test had been heated above ~75°C and the innermost part up to 155°C. Compared with the expected KBS-3 conditions, the TBT field experiment represented adverse conditions both with respect to temperature and temperature gradient, which are factors that will accelerate alteration processes in the bentonite buffer. The chemical/mineralogical characterization of the bentonite after the hydrothermal exposure indicates that:

- Sulfate was redistributed under the thermal and hydration gradients that were prevalent during the test. Anhydrite accumulated at some distance from the heater, whereas gypsum was dissolved in the peripheral parts of the buffer where water was supplied.
- Cristobalite was dissolved at the bentonite/heater contact.
- Calcite was dissolved in the warmest parts of the block.
- Exchangeable sodium was replaced by calcium in the warmest parts, probably as an effect of calcite dissolution, which must have affected the porewater composition.
- At the heater, the iron content of the bentonite was significantly increased due to corrosion of the steel. The excess iron was readily extractable into a citrate-bicarbonate-dithionite solution, which suggests that iron was not incorporated into the smectite structure but existed mainly as free oxides/oxyhydroxides (at least after exposure of the bentonite to oxic conditions). No neoformed iron phases were detected, neither in the XRD- nor in the FTIR profile, possibly because the neoformed iron phase(s) is/are poorly crystalline.
- The distribution of non-exchangeable magnesium displayed a clear gradient with a distinct maximum at the heater, suggesting a transfer of magnesium along the thermal gradient. The treatment of the samples prior to analysis (separation of <0.5 μm fractions, Na-conversion, dialysis) eliminates several possible sinks for Mg (e.g. Mg-carbonates, interlayer Mg) but both the source and sink of magnesium still remain to be identified.
- The Mössbauer spectroscopy with a three component fit and the measurements with lower Doppler-velocity indicated that the amount of Fe^{2+} had increased slightly, but the five component fit didn't support this observation. Hence, the increase in the amount of iron observed with chemical analyses was probably too small to be detected reliably with Mössbauer spectroscopy.

References

SKB's (Svensk Kärnbränslehantering AB) publications can be found at www.skb.se/publications.

Ammann L, Bergaya F, Lagaly G, 2005. Determination of the cation exchange capacity of clays with copper complexes revisited. Clay Minerals 40, 441–453.

Belyayeva N I, 1967. Rapid method for the simultaneous determination of the exchange capacity and content of exchangeable cations in solonetzic soils. Soviet Soil Science, 1409–1413.

Brindley G W, Brown G (eds), 1980. Crystal structures of clay minerals and their x-ray identification. London: Mineralogical Society. (Mineralogical Society Monograph 5)

Börgesson L, Johannesson L-E, Sandén T, Hernelind J, 1995. Modelling of the physical behaviour of water saturated clay barriers. Laboratory tests, material models and finite element application. SKB TR 95-20, Svensk Kärnbränslehantering AB.

Börgesson L, Johannesson L-E, Hernelind J, 2003. Earthquake induced rock shear through a deposition hole. Effect on the canister and the buffer. SKB TR-04-02, Svensk Kärnbränslehantering AB.

Carlson L, Karnland O, Oversby V M, Rance A, Smart N, Snellman M, Vähänen M, Werme L O, 2007. Experimental studies of the interactions between anaerobically corroding iron and bentonite. Physics and Chemistry of the Earth 32, 334–345.

Clarke E C W, Glew D N, 1985. Evaluation of the thermodynamic functions for aqueous sodium chloride from equilibrium and calorimetric measurements below 154°C. Journal of Physical and Chemical Reference Data 14, 489–610.

Cornell R M, Schwertmann U, 2003. The iron oxides: structure, properties, reactions, occurences and uses. 2nd ed. Weinheim: Wiley-VHC.

Dohrmann R, Genske D, Karnland O, Kaufhold S, Kiviranta L, Olsson S, Plötze M, Sandén T, Sellin P, Svensson D, Valter M, 2012. Interlaboratory CEC and exchangeable cation study of bentonite buffer materials. I. Cu(II)-triethylenetetramine method. Clays and Clay Minerals, 60, 162–175.

Dueck A, 2004. Hydro-mechanical properties of a water unsaturated sodium bentonite: laboratory study and theoretical interpretation. PhD thesis. Lund Institute of Technology, Sweden.

Dueck A, Börgesson L, Johannesson L-E, 2010. Stress-strain relation of bentonite at undrained shear. Laboratory tests to investigate the influence of material composition and test technique. SKB TR-10-32, Svensk Kärnbränslehantering AB.

Dueck A, Johannesson L-E, Kristensson O, Olsson S, 2011. Report on hydro-mechanical and chemical-mineralogical analyses of the bentonite buffer in Canister Retrieval Test. SKB TR-11-07, Svensk Kärnbränslehantering AB.

Evans B J, Johnson R G, Senftle F E, Blaine Cecil C, Dulong F, 1982. The ^{57}Fe Mössbauer parameters of pyrite and marcasite with different provenances. Geochimica et Cosmochimica Acta 46, 761–775.

Goudarzi R, Åkesson M, Nilsson U, 2010. Temperature Buffer Test. Sensors data report (Period 030326–100301) Report No: 13. SKB P-12-03, Svensk Kärnbränslehantering AB.

Greene-Kelly R, 1953. Irreversible dehydration in montmorillonite. Part II. Clay Minerals Bulletin 2, 52–56.

Greene-Kelly R, 1955. Dehydration of the montmorillonite minerals. Mineralogical Magazine 30, 604–615.

Greenspan L, 1977. Humidity fixed points of binary saturated aqueous solutions. Journal of Research of the National Bureau of Standards – A. Physics and Chemistry 81A, pp 89–96.

Hofmann V U, Klemen R, 1950. Verlust der Austauschfähigkeit von Lithiumionen an Bentonit durch Erhitzung. Zeitschrift für anorganische Chemie 262, 95–99.

Hogarth D D, Brown F F, Pritchard A M, 1970. Biabsorption, Mössbauer spectra, and chemical investigation of five phlogopite samples from Quebec. Canadian Mineralogist 10, 710–722.

Jackson M L, 1975. Soil chemical analysis: advanced course. 2nd ed. Madison,WI: Parallel Press.

Jodin-Caumon M-C, Mosser-Ruck R, Rousset D, Randi A, Cathelineau M, Michau N, 2010. Effect of thermal gradient on iron-clay interactions. Clays and Clay Minerals 58, 667–681.

Johannesson L-E, 2010. Temperature Buffer Test. Measurements of water content and density of the excavated buffer material. SKB P-12-05, Svensk Kärnbränslehantering AB.

Johannesson L-E, Sandén T, Åkesson M, Bárcena I, Garzía-Siñeriz, 2010. Temperature Buffer Test. Installation of buffer, heaters and instruments in the deposition hole. SKB P-12-02, Svensk Kärnbränslehantering AB.

Karnland O, Olsson S, Nilsson U, 2006. Mineralogy and sealing properties of various bentonites and smectite-rich clay materials. SKB TR-06-30, Svensk Kärnbränslehantering AB.

Karnland O, Olsson S, Dueck A, Birgersson M, Nilsson U, Hernan-Håkansson T, Pedersen K, Nilsson S, Eriksen T E, Rosborg B, 2009. Long term test of buffer material at the Äspö Hard Rock Laboratory, LOT project. Final report on the A2 test parcel. SKB TR-09-29, Svensk Kärnbränslehantering AB.

Kumpulainen S, Kiviranta L, Carlsson T, Muurinen A, Svensson D, Sasamoto H, Yui M, Wersin P, Rosch D, 2011. Long-term alteration of bentonite in the presence of metallic iron. SKB R-10-52, Svensk Kärnbranslehantering AB.

Lim C H, Jackson M L, 1986. Expandable phyllosilicate reactions with lithium on heating. Clays and Clay Minerals 34, 346–352.

Mehra O P, Jackson M L, 1960. Iron oxide removal from soils and clays by a dithionite-citrate system buffered with sodium bicarbonate. In proceeding of the 7th National conference on Clays and Clay Minerals, 317–327.

Meier L P, Kahr G, 1999. Determination of the cation exchange capacity (CEC) of clay minerals using the complexes of copper(II) ion with triethylenetetramine and tetraethylenepentamine. Clays and Clay Minerals 47, 386–388.

Moore D M, Reynolds R C, 1989. X-ray diffraction and the identification and analysis of clay minerals. Oxford: Oxford University Press.

Newman A C D, Brown G, 1987. The chemical constitution of clays. In Newman A C D (ed). Chemistry of clays and clay minerals. Harlow: Longman. (Mineralogical Society Monograph 6), 1–128.

Rietveld H M, 1969. A profile refinement method for nuclear and magnetic structures. Journal of Applied Crystallography 2, 65–71.

Russell J D, 1987. Infrared methods. In Wilson M J (ed). A handbook of determinative methods in clay mineralogy. London: Blackie, 133–173.

Taylor J C, Matulis C E, 1994. A new method for Rietveld Clay Analyses. Part I. Use of a universal measured standard profile for Rietveld quantification of montmorillonite. Powder Diffraction 9, 119–123.

Wadsö L, Svennberg K, Dueck A, 2004. An experimentally simple method for measuring sorption isotherms. Drying Technology 22, 2427–2440.

Wagner F E, Wagner U, 2004. Mössbauer spectra of clays and ceramics. Hyperfine interactions 154, 35–82.

Åkesson M, 2010. Temperature Buffer Test. Dismantling operation. SKB P-12-04, Svensk Kärnbränslehantering AB.

Åkesson M, Börgesson L, Kristensson O, 2010. SR-Site Data report. THM modelling of buffer, backfill and other system components. SKB TR-10-44, Svensk Kärnbränslehantering AB.

Appendix 1

Report on the TR03 series B+Tech bentonite samples

J. Lindén, Department of Physics, Åbo Akademi, FIN-20500 Turku, Finland

(Dated: January 14, 2011)

A1-1 Experimental

Five samples were investigated, each consisting of ~ 50 mg dry powder mixed with epoxy glue evenly spread on an area of ~ 3,0 cm^2. The samples were stored under a protective N_2 atmosphere in a glove box (concentration of O_2/H_2O less than 1 ppm) priortothe Mössbauer measurements. The samples were labelled: TR03-ref, TR03_250_C31, TR03_250_C33, TR03_250_C35, and TR03_250_C39. As the agreement was for six measuerements, two absorbers were made from the TR03-ref sample and measured separately. The first spectrum, denoted TR03-ref 1, was measured as number one and the second absorber, denoted TR03-ref 2, was measured after all other measurements had been completed. All spectra were collected at 77 K in transmission mode using a sinusoidal velocity scale with a maximum Doppler velocity of 10.1 mm/s. The velocity was chosen to allow detection of the magnetic lines of Fe oxides and hydroxides. For paramagnetic samples the scale is a a bit too large, but as shown by the spectra measured in 2009 weak magnetic lines are likely to be present. The geometry, i.e. source-to-detector distance, absorber area and collimation was the same for all samples, as well as the settings for the gamma-ray window. Data were collected for six days for each sample, yielding a folded background level of $\sim 25 \cdot 10^6$ counts.

Sample cooling was achieved using an Oxford ITC-4 continuous-flow cryostat operated with liquid nitrogen. The 14.4-keV Mössbauer quanta were produced by a Cyclotron Co. ^{57}Co:*Rh* (25 mCi Apr. 2009) source and detected using a LND 4546 porportional counter with a beryllium window. A Fast ComTec MA-250 velocity transducer was used for moving the source. It was equipped with a Halder MR-351 Drive unite. The data was gathered using a Fast ComTec MCA-3 multichannel-analyzer PCI card in an ordinary desktop PC. The measurement was done in the multiscaling mode.

The spectra were fitted using a home-made nonlinear least-squares fit program, utilizing spectral components corresponding to four paramagnetic doublets and one magnetic sextet. For the paramagnetic components parameters used in the fit were: The quadrupole splitting Δ, in mm/s, the isomer shift δ with respect to α-Fe, in mm/s and the spectral intensities I in %. For the magnetic component, additionally, the internal field B, in T and its gaussian distribution ΔB, in T were included as fit parameters. All components were constrained to have a common line width Γ, in mm/s.

A1-2 Results and discussion

The fitted spectra are displayed in the figures 1-6. The five components used for the analysis, all corresponding to various Fe species, are shown. Compared to the three spectra analyzed in 2009 there is one new component: Component 5 (drawn in green in all spectra). It is needed to explain the features close to the center of gravity of the spectrum. It corresponds to divalent Fe, judging by the high isomer shift value. Most probably this component was also present in smaller quantities in the three bentonite spectra measured in 2009, but remained then close to the detection limit.

By visual inspection the spectra are rather similar. The differences are rather subtle and may also partially be due to statistical variation. For example, the two first spectra are both recorded from the reference sample material (TR03-ref), but using two separate abosorbers. The spectra are by no means identical.

The dominating component is paramagnetic with a huge quadrupole splitting $\Delta \approx 3.0$ mm/s (Component 1 in Table A1-1). It has also a large isomer shift typical of divalent Fe. The same component was reported in the study by Carlsson et al. 2007. It is typical for Fe containing bentonite samples. On the inner slope of the first line of Component 1 additional paramagnetic features are seen. These were fitted using two quadrupole components (Components 2 and 3), as a single component was not enough to explain these features. Both components are due to trivalent Fe, based on the isomer-shift values. Only one such component was reported in Ref. 1. However, they might correspond to almost the same chemical environment, reflecting a less than perfect local crystallinity of the trivalent Fe species. This may be true if it is the result of a low-temperature oxidation of the divalent component. The second divalent component (Component 5) has a very high isomer shift, compatible only with high-spin Fe^{2+}, like Component 1. However, thequadrupole splitting for Component5 is much smaller than forComponent 1. Therefore, it must originate from a different surrounding than Component 1.

There are weak magnetic features in all spectra, but due to the very low concentration of magnetic iron the fitted parameters of the magnetic Mössbauer component are very uncertain. When a paramagnetic doublet becomes magnetically split all the intensity is distributed over six resonance lines and the detection limit increases approximately with 4, i.e. the concentration of a hypothetical magnetic Fe species could be four times higher than a paramagnetic one and still remain undetected in the Mössbauer spectrum. The fitted internal field for the magnetic component (Component 4) was 50–55 T, with uncertainties of at least 1 T. These values should in principle be due to Fe^{3+}, as divalent Fe seldom exhibits internal field exceeding ~ 48 T. Also the isomer shift values of 0.30-0.58 are compatible with high-spin Fe^{3+}. There is also a possibility that there are more than one magnetic component (like e.g. in magnetite), which can not be ruled out due to the very weak statistics for the magnetic lines. Assignment to a specific Fe oxide or hydroxide should therefore not be attempted. Instead one only give a rough estimate of the concentration of magnetic trivalent iron in the samples, see Table A1-1.

From Table A1-1 one immediately obtains the main result, i.e. the ratio of paramagnetic Fe^{2+} to Fe^{3+}, by assuming the recoil-free fraction to be the same for all components: 1.031 (TR03 ref 1), 0.840 (TR03 ref 2), 0.925 (C31), 0.927 (C33), 0.945 (C35) and 0.858 (C39). In this calculation the magnetic Fe was ignored. In case the magnetic Fe is lumped together with the other trivalent components (Component 2 and 3) the following results are obtained for the ratio of divalent to trivalent Fe: 0.873 (TR03 ref 1), 0.739 (TR03 ref 2), 0.805 (C31), 0.838 (C33), 0.869 (C35) and 0.767 (C39).

A1-3 Conclusions

Six bentonite absorbers from five samples were measured by ^{57}Fe Mössbauer spectroscopy at 77 K. The ratio of paramagnetic Fe^{2+} to Fe^{3+} was readily obtained. Traces (4–8% of the total intensity) of magnetic (trivalent) Fe was observed. Divalent Fe occurred in two distinct surroundings, one with a huge qudrupole splitting of ~ 3.0 mm/s, typical of bentonite samples (Carlsson et al. 2007) and the other in much smaller concentrations and a smaller quadrupole splitting. Paramagnetic Fe^{3+} occurred as two components with similar hyperfine parameters, suggesting that they migh origiante from similar chemical surroundings.

In order to reveal the detailed nature of the paramagnetic Fe^{3+} species, measurements at a lower Doppler velocity should be performed. Room-temperature measurements might suffice, in case the epoxy mixture is enough to prevent the sample from oxidizing. However, as the doublets due to Fe^{+2} are reasonably well resolved from the Fe^{3+} species the overall ratio between paramagnetic Fe^{+2} and Fe^{+3}, should remain close to the values obtained here, provided the assumption about equal the recoil-free fractions holds. Nevertheless, there is a distinct statistical uncertainty in the the intensity ratios, illustrated e.g. by the differences in the two separate measurements for the reference sample.

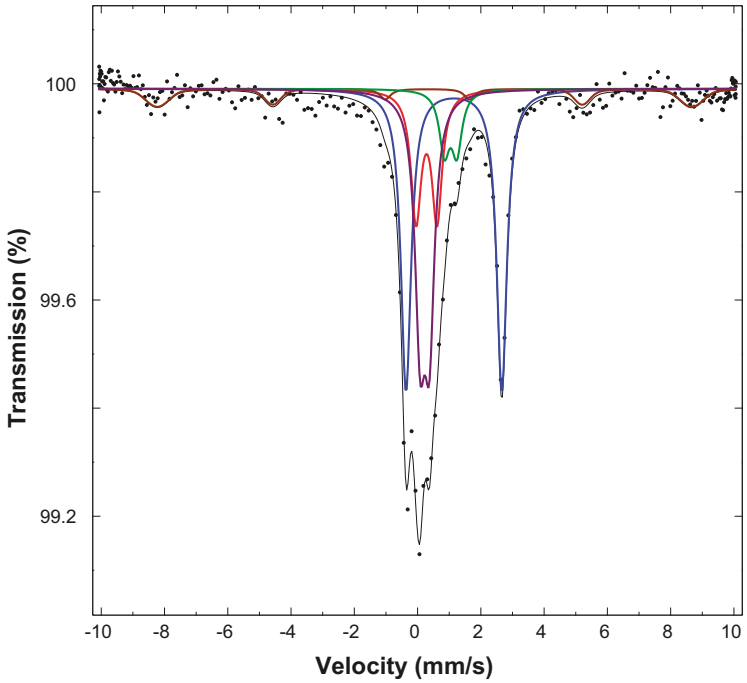

Figure A1-1. *Mössbauer spectrum recorded from sample TR03-ref at 77 K (1st sample). Components of the fit are displayed above the spectrum. They are: Component 1 in blue, Component 2 in red, Component 3 in violet, Component 4 in brown and Component 5 in green.*

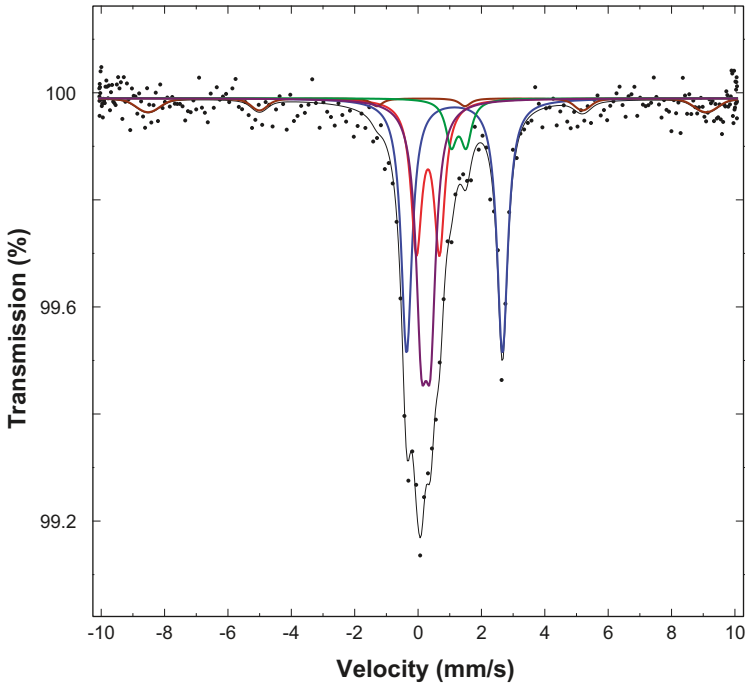

Figure A1-2. *Mössbauer spectrum recorded from sample TR03-ref at 77 K (2nd sample). Components of the fit are displayed above the spectrum.They are: Component 1 in blue, Component 2 in red, Component 3 in violet, Component 4 in brown, and Component 5 in green.*

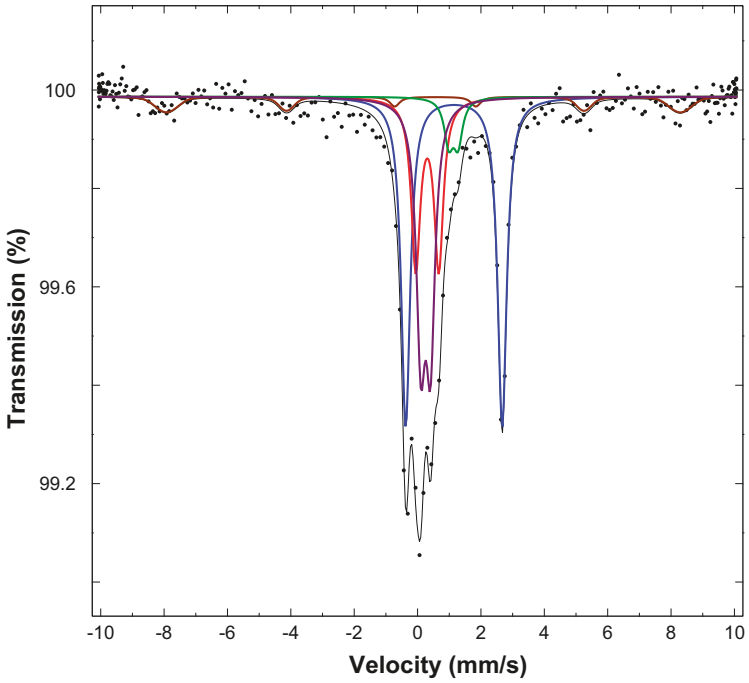

Figure A1-3. *Mössbauer spectrum recorded from sample TR03_250_C31 at 77 K. Components of the fit are displayed above the spectrum. They are: Component 1 in blue, Component 2in red, Component 3 in violet, Component 4 in brown and Component 5 in green.*

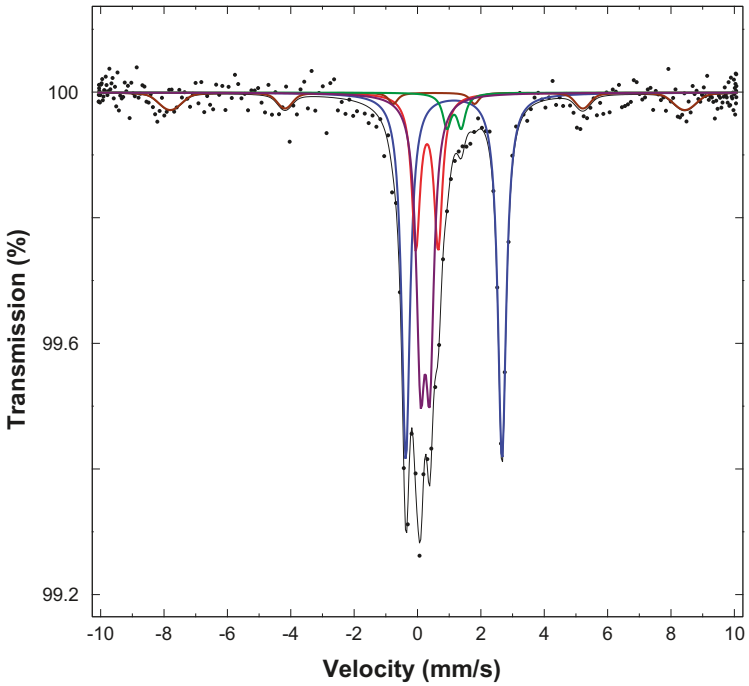

Figure A1-4. *Mössbauer spectrum recorded from sample TR03_250_C33 at 77 K. Components of the fit are displayed above the spectrum.They are: Component 1 in blue, Component 2 in red, Component 3 in violet, Component 4 in brown, and Component 5 in green.*

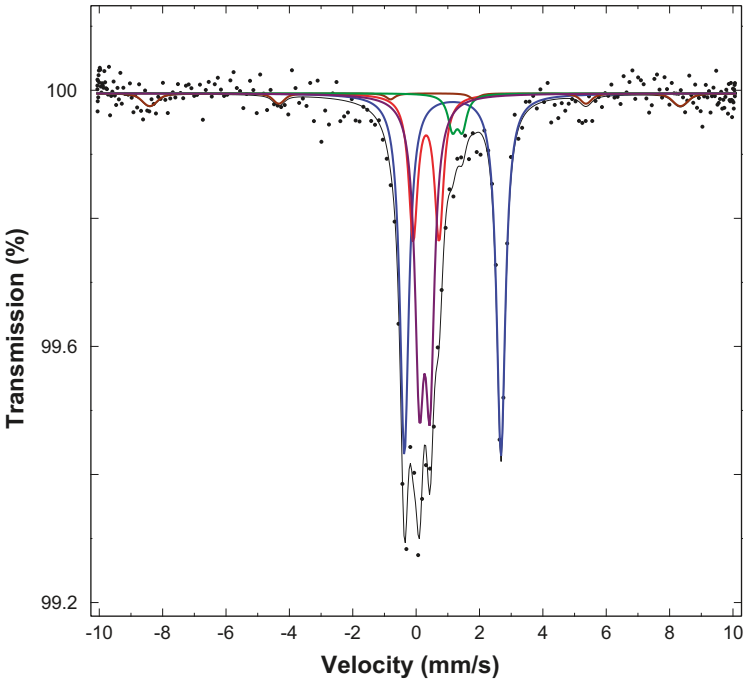

Figure A1-5. *Mössbauer spectrum recorded from sample TR03_250_C35 at 77 K. Components of the fit are displayed above the spectrum.They are: Component 1 in blue, Component 2 in red, Component 3 in violet, Component 4 in brown, and Component 5 in green.*

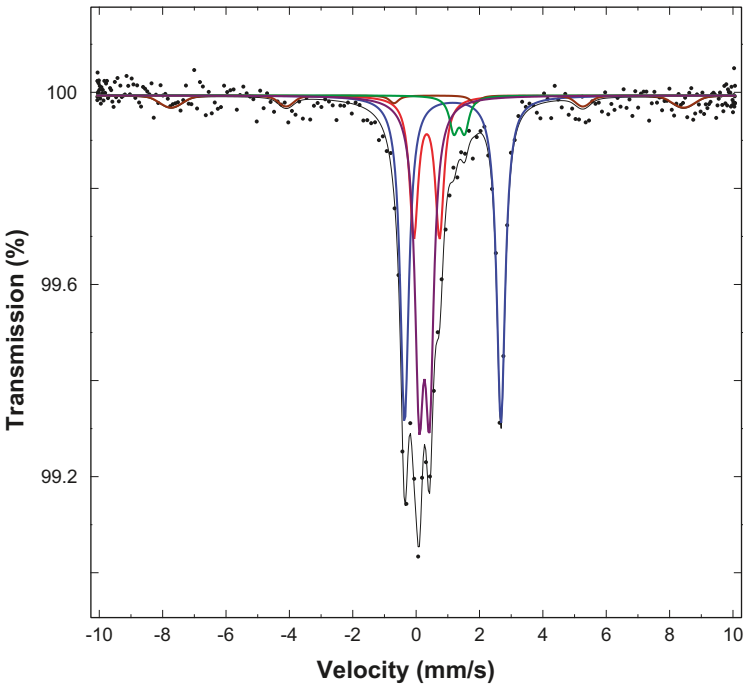

Figure A1-6. *Mössbauer spectrum recorded from sample TR03–250–C39 at 77 K. Components of the fit are displayed above the spectrum.They are: Component 1 in blue, Component 2 in red, Component 3 in violet, Component 4 in brown, and Component 5 in green.*

Table A1-1. Hyperfine parameters of the bentonite samples.

	I (%)	Δ (mm/s)	δ (mm/s)	B (T)	Γ (mm/s)
TR03 ref 1					
Component 1	38.9	3.028	1.261		0.386
Component 2	16.4	0.66	0.40		0.386
Component 3	28.8	0.29	0.34		0.386
Component 4	8(1)	–0.1(1)	0.38	52(1)	0.386
Component 5	7.7	0.29	1.16		0.386
TR03 ref 2					
Component 1	36.2	3.023	1.275		0.410
Component 2	20.9	0.73	0.42		0.410
Component 3	29.7	0.28	0.35		0.410
Component 4	7(1)	0.2(1)	0.30	55(1)	0.410
Component 5	6.3	0.28	1.39		0.410
C31					
Component 1	39.3	3.045	1.261		0.343
Component 2	20.1	0.73	0.42		0.343
Component 3	28.1	0.31	0.37		0.343
Component 4	7(1)	–0.4(1)	0.49	55(1)	0.343
Component 5	5.3	0.29	1.24		0.343
C33					
Component 1	41.8	3.035	1.258		0.318
Component 2	17.3	0.71	0.41		0.318
Component 3	29.0	0.29	0.35		0.318
Component 4	8(1)	–0.2(1)	0.53	50(1)	0.318
Component 5	3.8	0.29	1.26		0.318
C35					
Component 1	42.6	3.049	1.265		0.338
Component 2	16.9	0.82	0.43		0.338
Component 3	32.3	0.33	0.38		0.338
Component 4	4(1)	–0.5(1)	0.35	52(1)	0.338
Component 5	3.9	0.31	1.41		0.338
C39					
Component 1	39.4	3.041	1.265		0.327
Component 2	16.7	0.81	0.44		0.327
Component 3	33.9	0.32	0.37		0.327
Component 4	6(1)	–0.2(1)	0.58	50(1)	0.327
Component 5	4.0	0.34	1.47		0.327

Appendix 2

Report on the low-velocity re-measurements on samples TR03-ref and C33

J. Lindén, Department of Physics, Åbo Akademi, FIN-20500 Turku, Finland

(Dated: December 21, 2011)

A2-1 Experimental

Two samples were re-measured, each consisting of ~ 50 mg dry powder mixed with epoxy glue evenly spread on an area of ~ 3,0 cm^2.The samples had earlier been measured using a higher velocity (10 mm/s). However, it turned out that the original samples had oxidized, despite the protective epoxy-resin the powders were immersed in. The original sample containers were still stored under an protective N_2 atmosphere in a glove-box, inside the original containers. Therefore, new absorbers were manufactured. The samples measured were: TR03-ref and TR03_250_C33. Both spectra were collected at 77 K in transmission mode using a sinusoidal velocity scale with a maximum Doppler velocity of 4.59 mm/s. The velocity was chosen to allow better view of the paramagnetic main components. The geometry, i.e. source-to-detector distance, absorber area and collimation was the same for both samples, as well as the the settings for the gamma-ray window. Data were collected for a week for each sample.

Sample cooling was achieved using an Oxford ITC-4 continuous-flow cryostat operated with liquid nitrogen. The 14.4-keV Mössbauer quanta were produced by a Cyclotron Co. ^{57}Co:*Rh* (25 mCi Apr. 2009) source and detected using a LND 4546 porportional counter with a beryllium window. A Fast ComTec MA-250 velocity transducer was used for moving the source. It was equipped with a Halder MR-351 Drive unite. The data was gathered using a Fast ComTec MCA-3 multichannel-analyzer PCI card in an ordinary desktop PC. The measurement was done in the multiscaling mode.

The spectra were fitted using a home-made nonlinear least-squares fit program, utilizing spectral components corresponding to four paramagnetic doublets. The parameters used in the fit were: The quadrupole splitting Δ, in mm/s, the isomer shift δ with respect to α-Fe, in mm/s and the spectralintensities I in %. The magnetic component, seen in the earlier measurements was kept fixed at the parameter values observed earlier. However, it brought practically zero intensity to the relevant velocity intervall, as the most intensive lines are located at higher values for the absolute Doppler velocity.

A2-2 Results and discussion

The spectrum (not shown here) from the old absorber exhibited two major effects: loss of divalent Fe, seen as a decrease in the intensity of Component 1 and an overall decrease in absorbtion and increase in line width. The latter two effects can be ascribed to an overall deterioration of the crystallinity of the absorbers, due to the low-temperature oxidization.

The fitted spectra of the new absorbers are displayed in the Figures A2-1 to A2-2. The five components used for the analysis, all corresponding to various Fe species, are shown. An interesting question concerns the presence of Component 5, the isomer shift of which corresponds to divalent Fe. Its presence was noted in the high-velocity measurements and at least for the reference sample there seems to be a clear dip in the raw data indicating that it indeed exists. The high-velocity measurements gave higher line intensities for Component 5. There are not many datapoints for Component 5 in the high-velocity range, therefore the intensity estimates for Component 5 are more reliable.

Fit parameters are presented in the table.

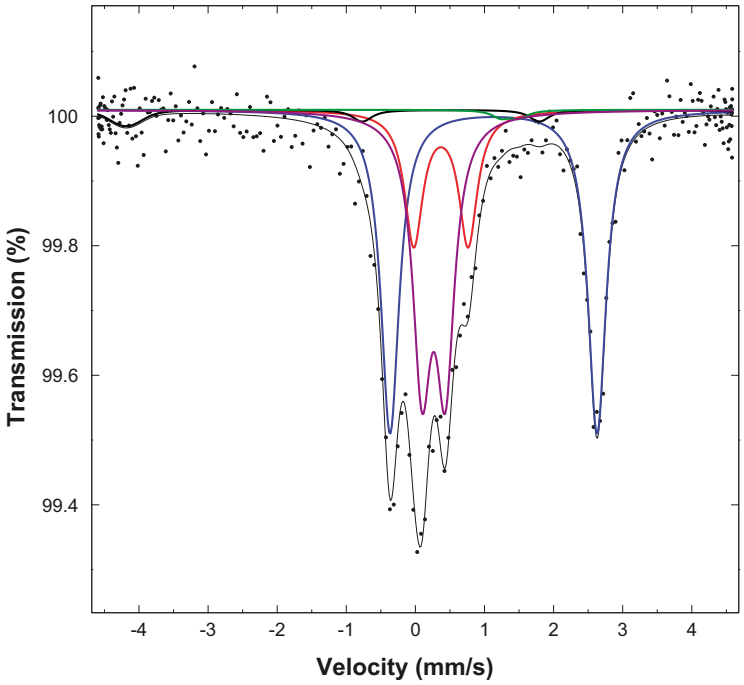

Figure A2-1. *Fitted Mössbauer spectrum recorded from sample TR03_250_C33 at 77 K. Components of the fit are displayed above the spectrum. They are: Component 1 in blue, Component 2 in red, Component 3 in violet, Component 4 in black and Component 5 in green.* $\chi^2 = 0.91372$.

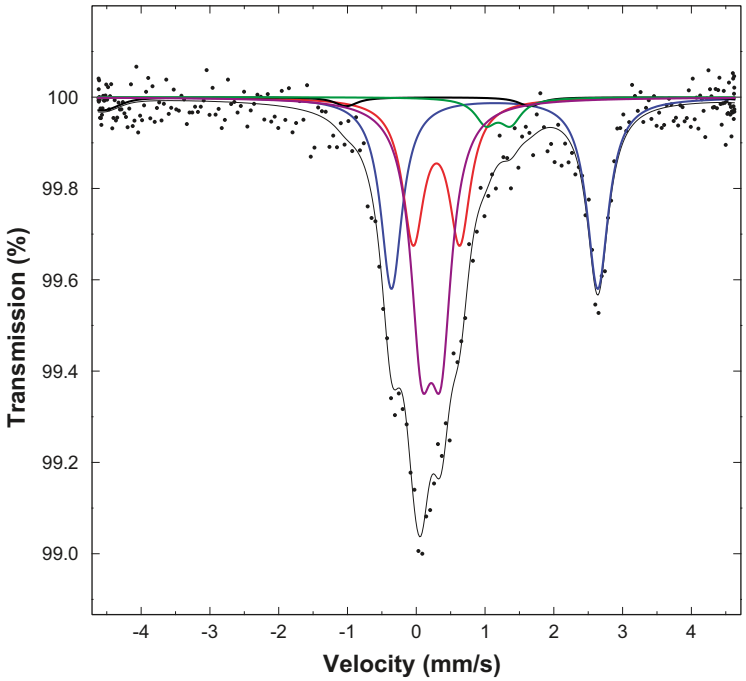

Figure A2-2. *Mössbauer spectrum recorded from sample TR03-ref at 77 K. Components of the fit are displayed above the spectrum.They are: Component 1 in blue, Component 2 in red, Component 3 in violet, Component 4 in black, and Component 5 in green.* $\chi^2 = 1.16387$.

Table A2-1. Hyperfine parameters of the remeasured bentonite samples.

	I (%)	Δ (mm/s)	δ (mm/s)	B (T)	Γ (mm/s)
TR03 ref 1					
Component 1	33.20	2.997	1.248		0.379
Component 2	24.08	0.677	0.403		0.379
Component 3	38.53	0.282	0.327		0.397
Component 4	–	–	–	–	0.379
Component 5	4.20	0.359	1.300		0.379
C33					
Component 1	44.90	2.995	1.246		0.319
Component 2	18.13	0.788	0.484		0.319
Component 3	35.64	0.338	0.378		0.319
Component 4	–	–	–	–	0.319
Component 5	1.30	0.26	1.48		0.319